UNIVERSITEIT VAN PRETORIA
UNIVERSITY OF PRETORIA
YUNIBESITHI YA PRETORIA

Experimental and Computational Investigation into Race Car Aerodynamics

Pieter Paulus Penning

Forti Corse SLR Formula One Team - 1995 Monaco Grand Prix

Submitted for partial fulfilment of the requirements for the degree
Master in Engineering (Mechanical Engineering)
in the
Faculty Engineering

University of Pretoria
Pretoria

May 1999

Synopsis[a]

Title:	Experimental and Computational Investigation into Race Car Aerodynamics
Author:	Pieter Paulus Penning
Study Leader:	Professor. K.J. Craig
Department:	Mechanical and Aeronautical Engineering
Degree:	Master in Engineering (Mechanical Engineering)

In this study, experimental tests and Computational Fluid Dynamics are used to investigate the aerodynamic performance of two types of track-based racing cars. After the literature study, where automotive aerodynamics is discussed in very general terms, the air flow beneath a Formula One Grand Prix Racing Car is investigated. This is achieved by fitting the under-tray of a 30% scale model of the Parmalat Forti Ford FG01-95 with surface-static pressure ports and testing the model in a rolling-road wind tunnel. By varying a number of model parameters, it is found that the wheels significantly alter the pressure distribution under the floor of the racing car at positions away from the centre-line. It is shown that the front or rear wheel sets are independently sufficient to induce the flow changes. The addition of the other set then only produces milder and more local changes.

The numerical part of the floor investigation is aimed at reproducing the centre-line flow pattern by solving the full Reynolds-Average Navier-Stokes equations over a two-dimensional curvilinear grid of the isolated floor. Two algorithms, Roe's flux-difference splitting method and the commercial package, STAR-CD which employs the SIMPLE algorithm and a two-equation turbulence model, are used to solve the governing equations. It is found that although the correct trends are observed when two different ride heights are simulated, absolute correlation is inadequate despite the use of experimentally-controlled boundary conditions. The simulations are however used to demonstrate the saturation in downforce with increasing vehicle speed.

In order to improve numerical accuracy, a second study was launched where the effect of including the centre-line profile of the complete vehicle is investigated. To reduce the amount of detail a $1/12^{th}$ scale model of a generic BMW Touring Car is used. Experimental data in the form of centre-line surface-static pressure coefficients are used for numerical correlation. The data is obtained by testing the three-dimensional model in a wind tunnel fitted with a stationary-road raised-platform floor. To establish continuity, the experimental data is used to show the similarities between the pressure distribution on the centre line of the open-wheel and the closed-wheel racing car. The effect of a rear-mounted aerodynamic device on the downforce is also discussed.

The numerical investigation using the SIMPLE algorithm of STAR-CD and three high Reynolds-Number turbulence models, is based on the centre-line profile of the experimental model. It is seen that although qualitative correlation exists in areas around the car, quantitative agreement is less positive. Discrepancies are found to be most significant under the floor. It is shown that the influence of the three dimensional flow field on the experimental results are unlikely to cause satisfactory correlation. It is suggested that, in order to improve correlation, a new investigation is launched aimed at refining the numerical model. An outline for the new study is presented and includes simulations indicating the dependence of the computational solution on the density of the grid and on the user-definable turbulence parameters.

---

[a] To fulfil the requirements as laid down by the University of Pretoria, the synopsis is repeated in Afrikaans on the next page.

Opsomming

Titel: Experimental and Computational Investigation into Race Car Aerodynamics
Outeur: Pieter Paulus Penning
Leier: Professor K.J. Craig
Departement: Meganiese en Lugvaartkundige Ingenieurswese
Graad: Magister in Ingenieurswese (Meganiese Ingenieurswese)

In hierdie studie word eksperimentele toetse en Berekeningvloeidinamika gebruik om die aërodinamiese werkverrigting van twee tipe baangebonde renmotors te ondersoek. Na die literatuurstudie, waar voertuig aerodinamika in breë terme bespreek word, word die lugvloei onder die vloer van 'n Formule Een Grand Prix renmotor ondersoek. Hier word die vloer van die 30% skaalmodel van die Parmalat Forti Ford FG01-95 met oppervlak statiese druktappunte ge-instrumenteer en dan in 'n rolvloer windtonnel getoets. Deur 'n aantal model-parameters te varieer is daar gevind dat die wiele die drukverdeling onder die vloer beduidend verander by posisies weg van die voertuig middellyn. Dit word getoon dat die voorste of agterste wiele die karakteristieke vloei veranderinge op hulle eie induseer. Die ander stel wiele veroorsaak dan slegs kleiner en meer lokale veranderinge.

Die doel van die numeriese gedeelte van die vloerondersoek is om die middellyn-vloeipatroon weer te gee deur die volle Reynolds-Getal Navier-Stokes vergelykings oor 'n twee dimensionele kromlynige rooster van die geïsoleerde vloer op te los. Twee algoritmes, Roe se "Flux difference splitting" metode en die komersiële pakket STAR-CD wat die SIMPLE algoritme en 'n twee vergelyking turbulensie model word toegepas, om die vloei op te los. Daar word vasgestel dat alhoewel die korrekte drukpatrone waargeneem word wanneer twee verskillende rithoogtes gesimuleer word, die absolute korrelasie onbevredigind is ten spyte van eksperimenteele beheerde grenstoestande. Die simulasies word egter wel gebruik om die versadiging in afwaartse krag met toenemende voertuigspoed te demonstreer.

Om die numeriese akuraatheid te verbeter is 'n tweede studie geloods waar die effek van die totale middellyn op die simulasies ondersoek word. 'n $1/12^{de}$ skaalmodel van 'n generiese BMW "Touring Car" word vir die doel aangewend. Die numeriese simulasies word gekorreleer deur middel van ekprimenteel bepaalde middellyn oppervlak-statiese-drukkoëffisiëntte. Die data word verkry deur die drie-dimensionele model in 'n windtonnel, toegerus met 'n verhewe-platform statiese vloer, te toets. Die eksperimentele data word eerstens gebruik om kontinuïteit met die eerste studie te bevestig deur korrelasie tussen die middellyn drukprofiele van die geslote-wiel en die oop-wiel renmotors aan te toon. Laastens word die effek van 'n agter-gemonteerde aerodinamiese installasie op die agter afwaartse krag bepreek.

Die numeriese ondersoek gebruik die SIMPLE algoritme van STAR-CD en drie hoë Reynolds-getal turbulensie modelle om die middellyn van die eksperimentele profiel te simuleer. Dit word getoon dat alhoewel kwalitatiewe korrelasie in sekere areas bestaan, die kwantitatiewe korrelasie nie so goed is nie. Die mees beduidende verskille word onder die vloer aangetref. Dit blyk onwaarskynlik dat die effek wat die drie-dimensionele vloeiveld op die ekpsrimentele reslutate het, die oorsaak hiervan is. Dit word voorgestel dat 'n nuwe studie geloods word met die doel om die numeriese model te verbeter. 'n Raamwerk vir die nuwe ondersoek word voorgelê, waar verdere simulasies die afhanklikheid van die oplossings aan die digtheid van die rooster asook die gebruikers-definieerbare turbulensie parameters aan toon.

Sleutelterme:
Aërodinamika, Voertuig, Renmotor, Padvoertuig, Formule Een, Touring Car, Windtonnel, Navier Stokes, STAR-CD, Berekeningsvloeidinamika,

UNIVERSITEIT VAN PRETORIA
UNIVERSITY OF PRETORIA
YUNIBESITHI YA PRETORIA

TABLE OF CONTENTS

1. INTRODUCTION

"At the heart of Formula One lies a very simple engineering concept: To send a racing car over a pre-determined course in the shortest possible time. That's it, nothing more and nothing less. Ironically, this is never really achieved. Technology aside, it astonishes me how fallible a human being is, people make mistakes all the time and to me, that is how races are won most of the time. You win, if the deficiencies in your team are less than the shortcomings of your competitor." - Hans Fouché, 1995, the best engineer I know and a very good friend.

Hans goes on: "F1 is not about magic, it is about understanding the principles at play, harnessing them and using them to your advantage .... It's about the basics, if you don't understand them, you'll get nowhere. You go into a wind tunnel with a bright idea and come out with more questions than answers. There is so much that we don't understand yet."

It is against this background that a study into the principles of the aerodynamic forces at play while racing, was launched. It is hoped that by examining the flow beneath a Formula One car, a small contribution can be made to this very fascinating and exciting engineering industry.

Since the discovery of the beneficial effects of under-floor flow in Formula One by Colin Chapman[1] in 1975, race car designers have continuously sought to improve traction by optimising the flow under the floor. After the dangers of ground effects became apparent, the governing body laid down strict rules to limit traction. Despite these constraints and the ones laid down in the years to follow, designers still managed to increase grip and decrease lap times on a regular basis. The 1995 season saw the introduction of a set of rules which dramatically altered the shape of the car floor. A stepped-bottom floor appeared for the first time. As the majority of the floor now had to be at least 50 mm above the ground, it was felt that the experience and knowledge gained on smooth-bottomed floors might no longer be relevant. The interaction between the floor and the rest of the car therefore had to be re-established. Consequently, a study into the flow beneath a Formula One car was initiated. This investigation, which was conducted using experimental and computational techniques, had the following objectives:

- To verify and determine the centre-line pressure profile by using experimental techniques.
- To use experimental methods to determine whether the characteristic flow patterns beneath the floor were functions of the floor profile alone, or whether other components also played a major role.
- To reproduce the flow patterns numerically by using the isolated centre-line geometry of the floor.

The study was based on the Parmalat Forti Ford FG01-95 Formula One racing car. This car was first raced during the 1995 Formula One season.

The main aim of this document is therefore to present the findings of this research project as outlined above. A secondary and perhaps a more subtle goal can be found in the structure and contents of the literature study. After this chapter, a person with very little or no knowledge of aerodynamics should be in a position to understand fundamental automotive aerodynamics and most of the findings presented in later chapters.

The history of gasoline-fuelled motor racing and the major aerodynamic advances that have been made since the inception of the sport at the beginning of the 20th century, are briefly presented at the beginning of the literature study. From this it can be seen that the application of wings in Formula One more than thirty years ago and the discovery of ground effects approximately a decade later, have lead to the very distinctive aerodynamic shape of the modern open-wheel racing car. The evolution of the modern racing car is used as a basis for the introduction of general automotive aerodynamic terms and concepts. The more traditional but still highly reliable experimental methods are discussed in Chapter 2 before the use of computational methods are examined.

The discussion on experimental techniques is introduced by examining the basic outlay of the different types of wind tunnels found in the industry today. As wind tunnels are used to measure aerodynamic quantities, the definition and use of these terms are presented in conjunction with a discussion on aerodynamic measuring equipment. This section is concluded by looking at wind-tunnel testing techniques. Here, issues such as the effect of scale, tunnel blockage and model-mounting techniques are outlined.

The literature study is concluded with a more technical look at the Computational Fluid Dynamics techniques which are currently used to solve fluid-flow problems. After presenting the governing Navier-Stokes equations in their integral and differential forms, the principles of turbulent flows are outlined. This is followed by a more detailed discussion of the turbulent models which are currently in use. The next topic under discussion, grid generation, outlines the various techniques which are used to construct the domain over which the flow field is to be solved. This includes the general transformation from the irregularly-spaced physical domain to a uniformly-spaced computational domain. The remaining two sections of Chapter 2 are aimed at discussing the numerical-solution methods which are employed to solve the governing equations and the boundary conditions which are required to define the numerical problem.

The investigation of the flow beneath the Formula One car, as presented in Chapter 3, was conducted in two parts. Firstly, a 30% scale model of the Parmalat Forti Ford FG01-95 was manufactured and tested in the low-speed rolling-road wind tunnel at the Council for Scientific and Industrial Research, South Africa. It was demonstrated that the centre-line pressure profile was representative of this type of vehicle. A number of changes were then made to the model in order to determine which factors, external to the floor, played a fundamental part in producing the pressure distribution beneath the car. Measurements were in the form of surface-static pressures. It was found that although parameters such as ride-height and front-flap position affected the intensity of the pressure map, the fundamental shape remained unaltered. The wheels were found to be instrumental in inducing significant changes to the pressure distribution. Interestingly, the front or rear wheel sets were independently sufficient to establish these flow changes. Adding the other set only produced milder and more local changes. Although the net effect of the wheels on the floor were negative, areas were found where the wheels had a beneficial influence.

As stated previously, the computational part of the investigation was aimed at determining the success of using isolated centre-line floor cases to predict experimental results. The computational domain was constructed using an efficient algebraic grid generator. Two numerical codes were used for the simulations. The first was an in house version of Roe's Flux Splitting Difference algorithm[2] and the second was the commercial code STAR-CD of

Computational Dynamics[3], England. The boundary conditions were controlled using experimental data. It was found, that despite the experimentally-fixed boundaries, the absence of external components such as the rear-wing assembly made predictions difficult. Changes to the centre-line grid, did however, produce the correct trends. The use of Computational Fluid Dynamics in Reynolds-Number sensitivity calculations is also demonstrated.

To address the problem of the poor numerical correlation under the floor of the Forti, a second study was launched. This is the subject matter of Chapter 4. Here, a $1/12^{th}$ scale generic model of a BMW Touring Car was used to investigate the accuracy with which the centre-line profile of the complete vehicle could be simulated. The F1 model was not chosen for this investigation as the smaller-scale closed-wheel racing car offered a more efficient, more economical and less sensitive method of obtaining the results.

The experimental results required for numerical correlation were obtained by manufacturing a scale model of the BMW, instrumenting it with surface-static pressure tubes, and testing it in a wind tunnel. The low-speed scale-model wind tunnel at the University of Pretoria in South Africa was used for the tests. The tunnel was equipped with a stationary-road raised-platform test-section floor. The objectives of the experimental investigation were:
- To establish similarities between the BMW and the Forti
- To obtain a base-line set of results for use in the numerical investigation
- To demonstrate the effect of a rear-mounted aerodynamic device

After repeatability and Reynolds-Number independence are demonstrated, it is shown that the pressure distribution beneath the BMW floor exhibits the same characteristics as those found under the F1 floor. Continuity is therefore established. By super-imposing the test results of a rear-mounted spoiler over the base-line data of the BMW, the effect of this device becomes clearly visible. The related discussion outlines the underlying phenomena responsible for rear downforce on sedan-based racing cars.

For the numerical investigation as presented in section 4.2, the centre-line profile of the experimental model was duplicated using the structured pre-processor of STAR-CD. The numerical investigation was centred around the accuracy of simulating turbulence by using the three high Reynolds Number turbulence models as supplied by STAR-CD.

The results showed that although the inclusion of the complete centre-line profile in the simulations increased the accuracy of the solution to a degree, the correlation of the predicted pressure distribution under the floor was still poor. It was also found that the three turbulence models out-performed one another in different areas around the vehicle. The poor numerical performance under the floor, the uncertainties regarding the choice of turbulence model and supporting experimental evidence lead to the conclusion that the numerical simulation was not accurate enough. It was therefore suggested that a further study should be launched but this new investigation went beyond the scope of this script. This new study should be aimed at improving the accuracy of the computational simulations of the BMW. A proposed direction for the new study is outlined in section 4.2.3. In this section it is shown by additional simulations that an increase in grid density is likely to improve the solution. The effect of varying the turbulence parameters is also shown to be a plausible method of improving correlation. Finally, it is concluded that if the standard STAR-CD turbulence models are unsuitable for the flow around the BMW, other turbulence models, which are designed to capture turbulence under adverse pressure gradients, should be used.

In Chapter 5 a conclusion is presented where the methodology and findings of this study are summarised.

Chapter 6 contains a list of all the references that were consulted during the course of this study.

Two appendices are also included. Appendix A presents the algorithm for the implementation of Menter's Shear Stress Transport turbulence model[4] and in Appendix B, Roe's Flux Difference Splitting procedure[2] for the full Reynolds-Averaged Navier-Stokes equations is outlined.

2. LITERATURE STUDY

A brief historical outline of automobile racing and the evolution of race car aerodynamics serves as a general introduction to this chapter. This is followed by an experimental literature study covering topics such as, wind tunnels and wind-tunnel models, test techniques and related equipment. Finally, numerical aerodynamics or Computational Fluid Dynamics (CFD), is presented and includes grid generation methods, flow solvers, boundary conditions and turbulence models.

2.1 Race Car Aerodynamics

2.1.1 The History of Automobile Racing and Race Car Aerodynamics

Automobile racing, using gasoline-fuelled internal combustion engines began in 1894, as a reliability race from Paris to Rouen, France. The race covered a distance of 80 km with the winner maintaining an average speed of just 16.4 kph[5]. Motor racing and manufacturers grew rapidly and within three years racing cars were looking distinctly different from road cars. The first regulation, which was introduced in 1898 after contestant fatalities, simply divided the cars into lightweight and heavyweight classes.

The first annual trophy, the James Gordon Bennet Cup, was launched in 1901 and national automobile clubs could each enter three cars. This cup transformed racing from a gentleman's sport to the more modern philosophy of "fastest wins"[1]. After spectator fatalities in 1901 and 1903, the French government banned street racing, unless events were held in sparsely populated areas and on roads with barriers.

The French manufacturers boycotted the Bennet trophy in 1906, as they were not content with only three cars per country. This lead to the first Grand Prix to be held at Le Mans in the same year. Racing events were now contested between rival manufacturers and not between national teams. The French ban on street racing lead to the first purpose built track at Brooklands, England in 1907.

From 1911, after the recession and until the beginning of the First World War, motor racing in Europe underwent significant changes. The evolution of racing circuits from basic triangular or oval shapes, to more twisting and winding circuits, led to the changes in design philosophy. Racing cars were becoming less dependent on engine power and more dependent on manoeuvrability, better brakes and more flexible engines.

The first limitation on the body-work was introduced in 1912, when the maximum width of the cars was limited to 175 cm's. For the 1913 season, the first rule had surfaced which limited the use of aerodynamic devices. Streamlined tails behind the fuel tank were not permitted[1]. By 1914, racing cars were moulded into a form which remained almost unchanged for the next 40 years.

The rapid progress in engineering during the First World War, served as a basis for a period of technological advancement in European motor sport. These advances led, amongst other things, to the 1923 Fiat 805.405, which was the first Grand Prix car to be developed in a wind tunnel.

The American designers were less eager to adopt the new found knowledge and persisted in emphasising engine power as the key to success.

In 1947, *the Fédération Internationale de l'Automobile* (F.I.A.)[i] divided Grand Prix racing into two formulae: the F.I.1 and the F.I.2. Formula One and its subsidiaries were born. During the same year the National Association for Stock Car Auto Racing (NASCAR) was founded in the U.S.A. In 1950, a Formula One world championship for drivers was started, followed by a championship for constructors in 1955. Hot Rod and particularly Drag Racing, which originated in California in the 1930's, was recognised by the F.I.A. in 1965. Racing with midget cars, which lead to cart racing, began in the 1940's in the USA and expanded to several international events from the 1960's onwards.

Until the 1950's, engine, chassis and tyre technologies were still changing rapidly, but aerodynamic improvements were largely aimed at drag reductions. By 1961 the transition from front mounted, to rear-mounted engines in Formula One was complete. Cars were now becoming smaller, lighter and more streamlined. The Coopers (father and son)[1], started the move towards rear-mounted engines, but it was the Lotus designer Colin Chapman who capitalised on it. He was, in 1959, in a quest for the smallest frontal area, the first to change the driver's seat from an upright to a more reclined position.

The smaller, more streamlined rear-mounted engine cars were less readily accepted in the USA. It took the second place of the comparatively small Lotus of Jim Clark at the Indianapolis in 1963 and the win in 1965, where he increased the average lap speed by 10 mph[6], to convert the Americans.

One of the American pioneers in the rear-engine racing car design arena was Jim Hall, joint owner of Chaparral. He joined Lotus so that he could study Grand Prix racing at first hand. He returned to the USA in 1963 and started designing rear-engine cars for the Canadian-American (CanAm) racing series. His designs carried two notable aerodynamic innovations; the front end spoiler beneath the nose and the first successful inverted wing above the rear axle. The wing was first seen on the 1966 Chaparral 2E. This idea was not copied effectively by Grand Prix constructors until almost two years later. This was partially due to the introduction of a new racing formula in 1966. The new formula retained, amongst other rules, the 1961 rule which banned body-work around the wheels. This rule was becoming more significant, as the ever increasing tyre widths were affecting the aerodynamic performance of the cars.

From 1968 the use of wings in F1 had spread almost uncontrollably. The wings had variable angles of attack, numerous shapes and sizes and were attached to all areas of the body-work and suspension. The poor construction and attachment methods frequently caused the wings to break off. This lead to serious accidents and subsequently, in 1969, the F.I.A. laid down strict rules governing the use of wings. The front wings were limited to nasal fins, while the rear wings were confined to a small area fixed to the sprung mass of the car.

---

[i] The *Alliance Internationale des Automobiles Clubs Reconnus,* which was formed in 1904, was renamed *the Fédération Internationale de l'Automobile* in 1946.

The next aerodynamic revolution came to motor racing in the form of the 1978 Lotus, designed by Colin Chapman. He designed the under-tray of the car in the shape of two half venturis, one on either side of the cockpit. The under-tray of the car formed the upper surface of the venturi, while the lower side was made up by the road surface. The venturis, which generated large amounts of negative pressure, especially when sealed using moveable side skirts, increased cornering speeds tremendously. The dangers involved in the high speeds lead to the banning of side skirts in 1981. Subsequent rule changes over the years, have lead to significant reductions in the size of the venturis in Formula One. Where the rules permit, large under-body diffusers are still used in other forms of motor racing.

There have been many other aerodynamic innovations, but none have been so radical and so important as the use of wings and ground effects.

The governing bodies are continuously revising the aerodynamic regulations, in an attempt to make motor sport safer.

2.1.2 Aerodynamics of Modern Racing Cars

Figure 2-1 presents a Formula One racing car, indicating the most important aerodynamic devices found on a racing car.
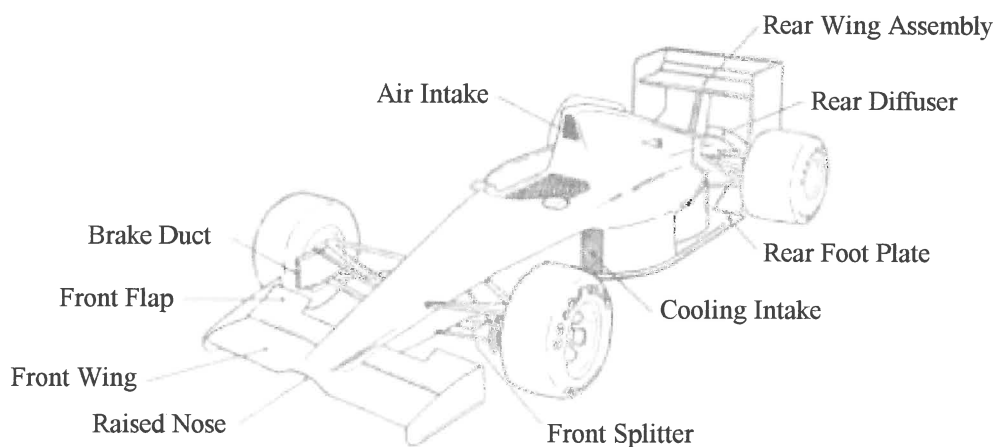

Figure 2-1 - Prominent Aerodynamic features of a 1992 Formula One Racing Car[7]

It can be seen from Figure 2-1, that race car aerodynamics can be divided into two classes. Internal aerodynamics, covering areas such as cooling ducts, heat exchangers, engine intakes and brake ducts and external areas such as wings, diffusers and body panels. To optimise these devices the aerodynamicist can use one of two techniques[8]:

- Experimental and
- Numerical or computational methods.

Traditionally, experimental methods were the only viable tool available to improve the aerodynamic performance of racing cars. With the advent of the high-speed digital computer, the aerodynamicist now has a relatively new tool on which he can rely. Potentially, CFD can be a very powerful and cost-effective tool to optimise the performance of cars. CFD has been used by some of the top Formula One teams in their development programmes[9,10]. Although the use of numerical flow solvers is becoming a more common practice, experimental aerodynamics is still regarded as the more reliable method for external flow problems.

2.2 Experimental Literature Study

Experimental aerodynamics can broadly be divided into two categories: road or track and wind-tunnel testing. Although both have advantages, wind tunnels are usually favoured when extensive development programmes are undertaken. This is largely due to the obtainable level of fluid control and the objective nature of tunnel tests. Furthermore, measuring equipment can be too bulky or too sensitive for track usage and can complicate experimental modifications. Track testing is normally used for verification, correlation and final "tuning", where driver preferences and track conditions become significant.

2.2.1 Wind Tunnels

Low-speed wind tunnels (LSWT) are commonly used for road and racing car development programmes. These tunnels are generally designed to operate at speeds below 300 mph (482 kph), where fluid compressibility is negligible[11]. This is the domain, in which most racing cars, except for certain types of drag racers and land-speed record vehicles, have to perform.

2.2.1.1 Low-Speed Wind tunnel Types

LSWT, where air is used as the test fluid, can be divided into two categories:
- Open-return tunnels and
- Closed-return tunnels

Open-return tunnels have their inlets and outlets venting to the atmosphere. These are usually cheaper to construct and are also preferable when engine development work or smoke generators are used frequently. They are more prone to noise pollution and testing can be dependent upon weather conditions if the tunnel is not enclosed in a larger building,.

In closed-return tunnels the air is circulated in a continuous loop. These are more expensive to build but are cheaper to operate. Although less dependent on weather fluctuations, they can be subject to rising air temperatures during prolonged tests. This problem can be overcome at additional costs, by installing air or heat exchangers.

The test sections of both types of tunnels are divided into either open-jet or closed-jet test sections. Open-jet test sections are usually enclosed in larger structures and do not, except for the road surface, have test section walls. Larger models can therefore be used, as the effect of tunnel blockage and pressure reflections are smaller. Although the stream-wise static pressure distribution is more constant in open-jet sections, they generally have to be shorter due to air dissipation to the surroundings. The reader is referred to section 2.2.3.2 for a definition of the terms used above.

2.2.1.2 Automotive Wind tunnel Testing

Unlike most studies in the aerospace industry where one medium, the test vehicle, is passing through another medium such as air, land vehicles are always in close proximity to a third medium. This third constraint, the road or running surface, also has to be duplicated or simulated in a wind tunnel. Several methods have been developed in an attempt to achieve this. As a first approximation, one of the tunnel walls could be used but an examination of the wall and road-boundary layers reveal significant differences. These are illustrated in Figure 2-2.

Boundary Layer
Profiles

Vehicle moving
on a Track

Vehicle mounted in a
Wind Tunnel with a
stationary floor
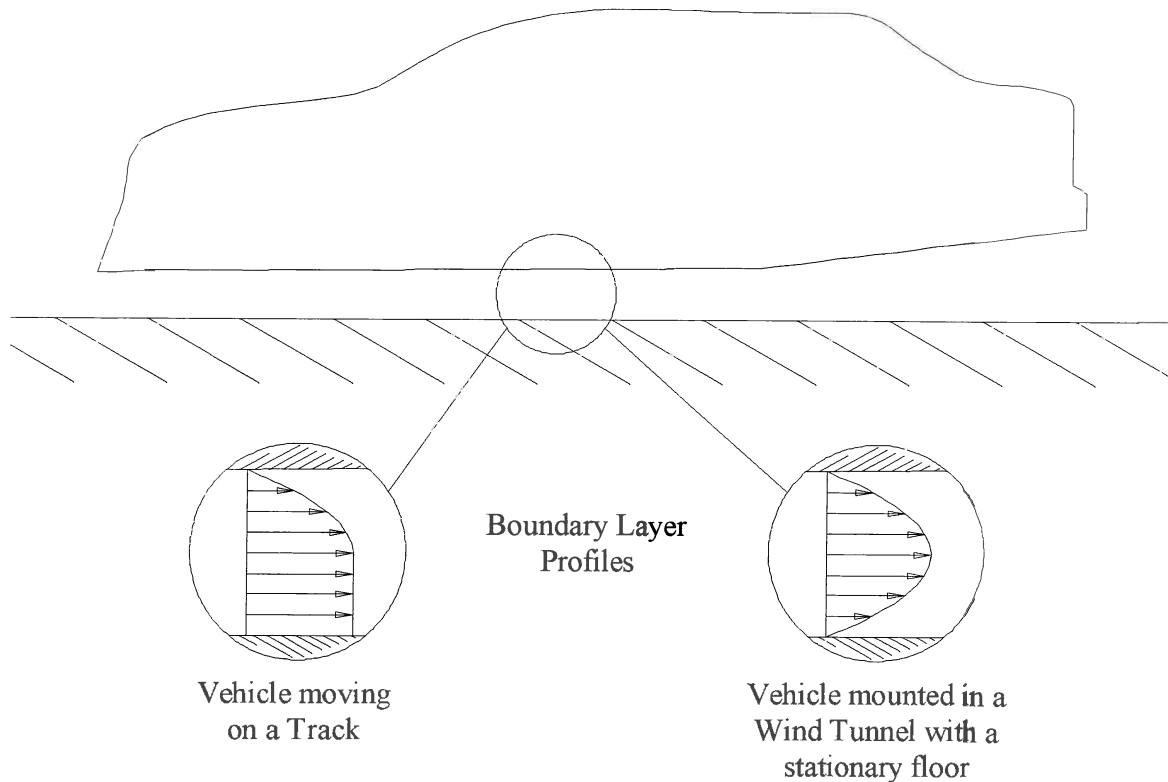
Figure 2-2: Boundary layer profiles of a vehicle moving on the road and mounted in a wind tunnel

In a real fluid, there is a viscous interaction between molecules of dissimilar velocities. This, combined with the condition of no-slip on the surface of an immersed solid[12], leads to a velocity gradient between the surface and the free stream fluid. This is known as the boundary layer and is discussed in more detail in section 2.2.3.1. On the track, under wind-still conditions, the road is stationary relative to the air. Here, boundary-layer development occurs only on the surface of the vehicle. In a wind tunnel however, where the vehicle is stationary relative to the fluid, there is boundary-layer growth on the vehicle surface, as well as on the tunnel floor.

An example of such a wall boundary layer was measured at the General Motors full-scale tunnel[8]. At the end of the test section, it was found to be approximately 130 mm thick at 95% of free stream velocity. Boundary-layer growth can become quite significant when developing racing cars, which often operate with ground clearances of the same order. Various methods aimed at addressing this problem have been developed. The most common solutions to this problem are shown in Figure 2-3.

The simplest and cheapest method of avoiding the boundary layer, is to mount the car on a raised platform situated in the free stream air as shown in Figure 2-3A. Although the tunnel boundary layer is avoided, the vehicle becomes subject to another one formed on the raised platform. This layer can be reduced by inclining the ground plane at a small negative angle[13]. Another method which can be employed, is to raise the model by an amount corresponding to the thickness of the layer. Care also has to be taken not to induce re-circulating flow at the end of the plate, due to an incorrect air split above and below the raised floor.

A - Raised ground plane

B - Suction in front of model

C - Suction Platen

D - Moving Belt
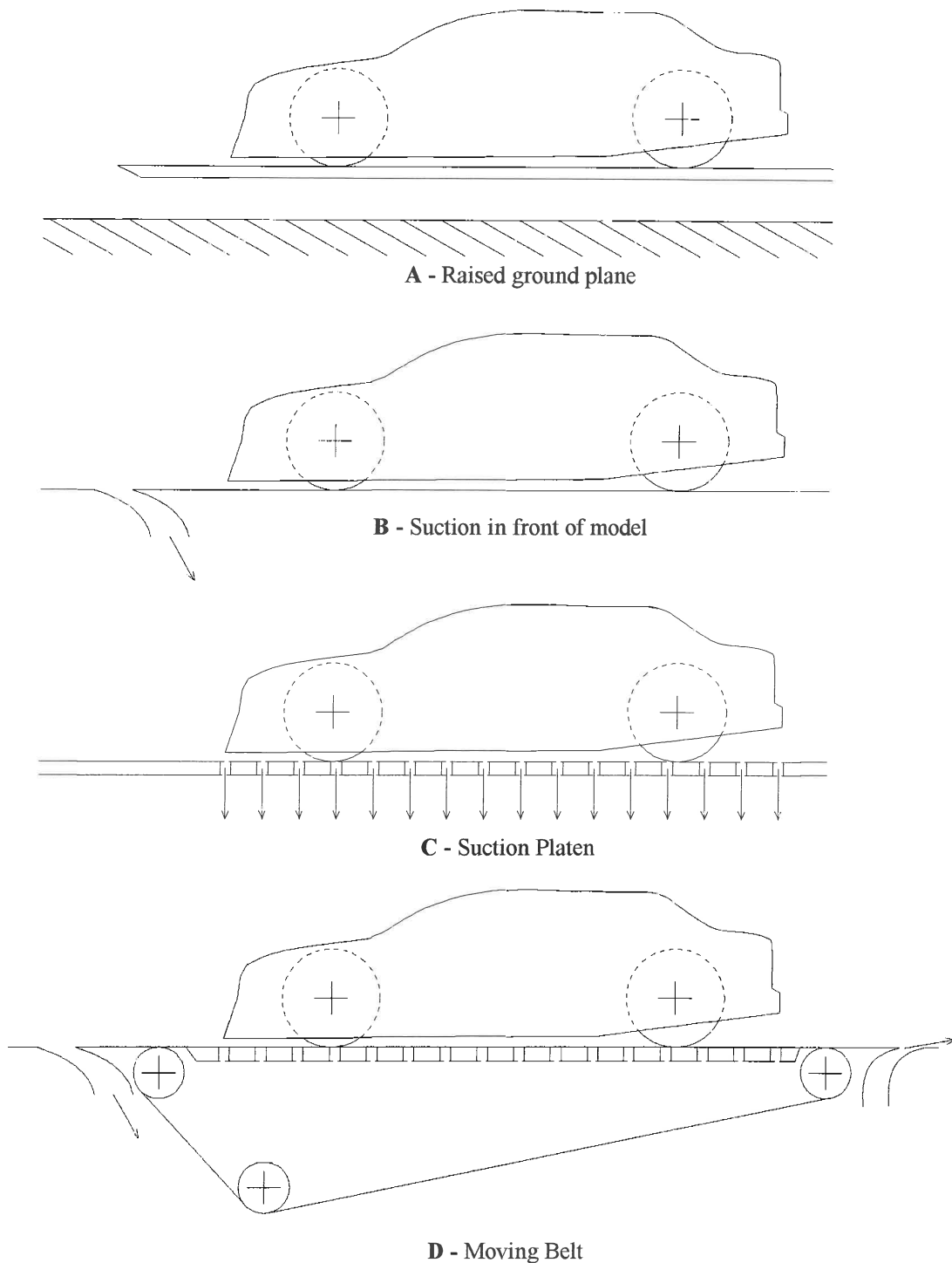
Figure 2-3 : Methods of simulating the moving ground

A slightly more complicated method is depicted in Figure 2-3 B. Here, a span-wise suction slot is placed in front of the model to remove the boundary layer. The amount of suction has to be controlled carefully. Too little will not remove the layer, while excess suction can cause flow reversal. Unfortunately, a new boundary layer will start forming immediately behind the slot, even if the wall layer is removed completely. To overcome this problem, a more

complicated, but more effective method is to introduce a suction platen under the entire test-section floor, as illustrated in Figure 2-3 C. Although this method has the potential to eliminate the boundary layer completely, discrepancies still remain over the amount and variation in length-wise suction which is required for different types of vehicles.

The last illustration in Figure 2-3 is that of a rolling road system with suction slot. Despite the high initial expense, this system is used almost universally by all open-wheel racing teams. This is because the road and car floor interaction is critical to them. The boundary layer is removed by the front suction slot and then prevented from re-forming by synchronising the air and belt speeds.

Mercker and Knape[14] investigated the use of tangential blowing instead of a rolling road for passenger cars. Their results showed discrepancies when measuring the front wheel lift.

The moving ground plane or belt, also makes the simulation of the rotating wheels possible. This is essential to open-wheel racing cars, as the flow field in which the car is immersed, is strongly influenced by the large rotating wheels.

The moving ground plane, does however, introduce several complications. The overhead and rear mounted struts or stings which are required to secure the model (section 2.2.3.3), cause additional flow-field interference. The negative pressure under the racing car necessitates the use of a suction platen to prevent the belt from lifting. The friction induced by the belt running over the platen generates heat, and so platen cooling is required. A belt-steering mechanism is also needed to keep the belt in position at high speeds. The suction platen, belt steering or centring mechanism and related cooling problems, usually limit the operating speed of the tunnel to around 25 to 60 m/s. This can be well below the operating speed of the racing car.

The air which was removed from in front of the belt in Figure 2-3 D, is re-introduced immediately behind the belt. This is to delay the formation of the boundary layer behind the rolling road.

The methods presented in Figure 2-3 are all aimed at eliminating or correcting the tunnel-wall boundary-layer phenomena. The relatively large wake produced by bluff bodies such as motor cars, are not addressed in any of these methods. To compensate for this, Garry et al.[15] found that the rear end of a road vehicle on a raised platform, should be at least four times the square-root of its base area or $x \geq 4A^{1/2}$, from the end of the test section. He observed drag errors of 10 to 20% when this distance was less than $x = 2A^{1/2}$.

2.2.2 Wind-Tunnel Measurement Techniques

The effective development of a racing car depends on the ability of the aerodynamicist to measure and analyse experimental data with high degrees of accuracy and repeatability. The data types can for clarity, be divided into three categories:
- Body forces and coefficients
- Aerodynamic pressures
- Flow visualisation techniques

2.2.2.1 Body Forces and Coefficients

When a body such as a racing car moves through a fluid such as air, the fluid exerts a pressure and a shearing action on the surface of the vehicle. If integrated, a single resultant force can be calculated around the aerodynamic centre, or centre of pressure (COP) of the vehicle. This force can be divided into three independent components, known as the drag, the lift and the side force. If these forces are translated to another point such as the centre of gravity or centre of the wheelbase of the vehicle, three corresponding moments, the rolling, the pitching and the yawing moment appears. It should be noted that the centre of pressure of the side force, is generally not in the same longitudinal position as that of lift force[16]. The sign convention and aerodynamic moments and forces, as defined by the Society of Automobile Engineers (SAE)[17], is shown in Figure 2-4.
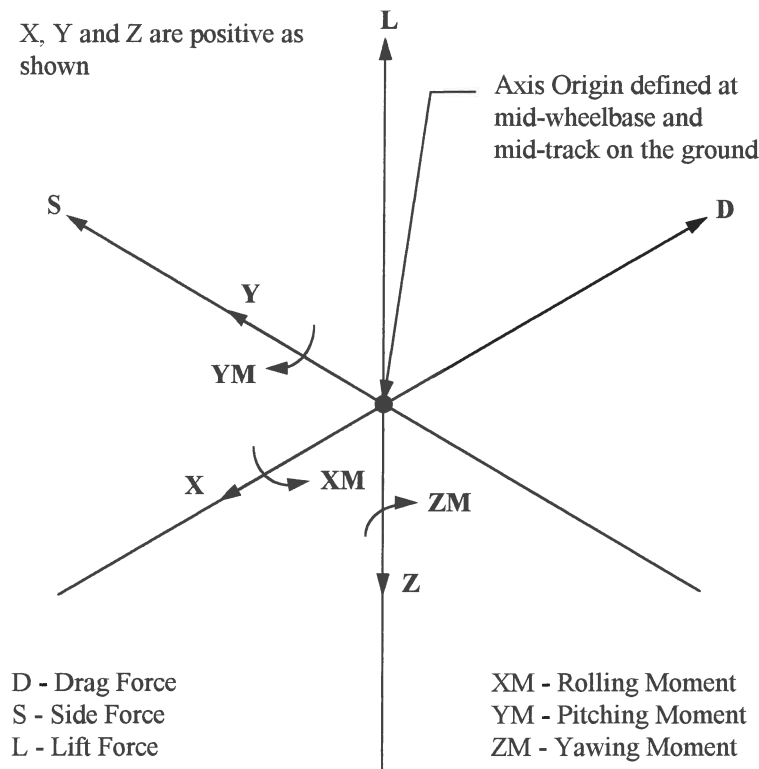
Figure 2-4 - SAE Aerodynamic Force and moment convention

The first of the forces to be discussed, is the drag force. This is a resistive force, which slows a body in motion and acts along the longitudinal axis of the vehicle. The drag force can be divided into two components[18], a pressure or form drag and a friction or surface drag. Pressure drag depends largely on the shape or form of the body and is caused by the pressures acting on the body. The surface drag arises due to shear forces acting on the body. The relative importance of the surface and pressure drag depends largely on the shape of the body. For very slim or streamlined shapes, the surface drag is the dominating factor. For blunt bodies, such as road vehicles and racing cars, the pressure drag is more important.

Lift is the force component acting either perpendicular to the direction of motion, or perpendicular to the free-stream velocity. The aerodynamic lift is primarily produced by the

pressure forces acting on the vehicle[19]. As most racing cars generate negative lift, the positive term "downforce", is almost universally used to describe negative lift.

The side force, is defined as a force acting perpendicular to both the lift and the drag.

The rolling moment acts around the longitudinal axis of the vehicle. This moment is created by asymmetrical lift and side forces between the starboard and port sides. The yawing moment is resolved along the vertical axis of the vehicle. It is the result of non-symmetrical drag and side force distributions along the longitudinal centre line. The pitching moment acts along the lateral axis and is produced by uneven lift and drag forces.

The body forces and moments are mainly measured using wind-tunnel balances[11]. Aerodynamic balances are very complicated, as the forces acting on the body, have to be de-coupled into independent components. Traditionally, this was achieved using intricate mechanically designed balances, but strain gauges have also been in use for a number of years. Balances can measure from one up to six components. Depending on their position in relation to the model, they are known as internal or external balances.

The forces and moments measured in a wind tunnel are seldom directly applicable to the track. This is because the wind-tunnel model scale and test speeds are often different to that experienced when racing. This dilemma is solved by non-dimensionalising the quantities and expressing them as aerodynamic coefficients. These non-dimensional aerodynamic coefficients are defined below.

The Force Coefficients:

$$C_i = \frac{F_i}{\frac{1}{2}\rho V_\infty^2 A} \text{ where } i = \begin{cases} D - \text{Drag} \\ Y - \text{ Side} \\ L - \text{Lift} \end{cases}$$

Equation 2-1

The Moment Coefficients:

$$CM_i = \frac{M_i}{\frac{1}{2}\rho V_\infty^2 Al} \text{ where } i = \begin{cases} X - \text{Roll} \\ Y - \text{Pitch} \\ Z - \text{Yaw} \end{cases}$$

Equation 2-2

F_i and M_i are the measured forces and moments respectively, V_∞ is the free-stream velocity, A is the vehicle frontal area and ρ is the density of air. The wheelbase, or total vehicle length can be used as the additional dimension (l) which is required when calculating the moment coefficients.

After Reynolds-Number independence (section 2.2.3.1) is demonstrated prior to a test series, the coefficients can then be converted back to forces and moments, at track or any other operating conditions. This is achieved by applying the same relations as Equation 2-2, but by substituting the tunnel conditions for those experienced on the track. The coefficients can also be used directly, to compare the aerodynamic performance of different vehicles with the same

frontal area. Another application is the calculation of performance related figures. For example, the power requirements can be calculated at any speed, given the drag coefficient, or conversely, the vehicle speed can be determined at any given engine power. The tractive resistance equation[20] as defined in Equation 2-3, is used to derive these quantities.

$$P_w = \left[\mu_r mg \cos\theta + \tfrac{1}{2}\rho C_D A v^2 + mg \sin\theta + m\ddot{\theta} \right] v$$

<div align="right">**Equation 2-3**</div>

or

$$\binom{\text{Power}}{\text{Required}} = \binom{\text{Rolling}}{\text{Resistance}} + \binom{\text{Drag}}{\text{Resistance}} + \binom{\text{Climbing}}{\text{Resistance}} + \binom{\text{Acceleration}}{\text{Resistance}}$$

where

$$\mu_r = \mu_s + \mu_d v\ ;$$
$$P_w = P_e \eta_d$$

and

C_D = drag coefficient

P_e = engine power $[W]$

η_d = drive train efficiency

v = top speed $[m/s]$

μ_s = static rolling resistance

μ_d = dynamic rolling resistance

μ_r = effective rolling resistance

m = vehicle mass $[kg]$

ρ = density $[kg/m^3]$

A = vehicle frontal area $[m^2]$

$\ddot{\theta}$ = inertial rotation

During analysis, the aerodynamic coefficients are sometimes expressed as ratios in order to obtain a better understanding of the aerodynamic performance of various vehicle configurations. The Lift to Drag ratio (C_L/C_D) is frequently used to compare the efficiency with which different body components generate lift. When the changes in efficiency become very small, this ratio can be modified even further. The ratio of the change in lift to the change in drag ($\Delta C_L/\Delta C_D$) can then be used.

The dynamic pressure ($\tfrac{1}{2}\rho V^2$), as used to define the coefficients shown previously, can be obtained in a wind tunnel using a pitot-static tube. The pitot static consists of two concentric tubes. An inner tube, open at both ends and an outer tube, sealed at the leading edge barring a series of holes perpendicular to the longitudinal axis. The pitot-static tube is installed by pointing the tip into and parallel to the flow and connecting the other end to a manometer or pressure transducer. The inner tube measures the total air pressure, while the outer tube only measures the static pressure.

The measured pressures are related to one another through the dynamic pressure, as expressed in Bernoulli's equation[8]:

$$P_{tot} = P_\infty + \tfrac{1}{2}\rho V^2$$

or

Total Pressure = Static Pressure + Dynamic Pressure

The track performance or lap times of racing cars do not only depend on the size of the aerodynamic forces but are also strongly influenced by the position of the centre of pressure and the sensitivity of that point to changes in driving conditions. To determine this, the distribution of the forces has to be known. This is achieved by using a multi-component balance, which measures the aerodynamic moments around a known point, or by using two one-component force balances for each distribution direction. The force distribution can then be resolved using the position of the balance and the geometry of the vehicle.

2.2.2.2 Surface Pressures

The forces and coefficients discussed in the previous section, supply the aerodynamicist with information regarding the performance of the complete vehicle. While this information is adequate when looking at design targets, or when comparing different vehicles, very little insight is gained into the characteristics responsible for these coefficients. Understanding the flow field surrounding the car is often the key to a successful development programme.

The pressures acting on blunt bodies, such as racing cars, are as described earlier, predominantly responsible for the aerodynamic behaviour of the vehicle. Knowledge of these pressures, can therefore lead to a better understanding of the aerodynamic characteristics of the vehicle. One method of achieving this, is to measure the surface-static component of the total pressure. This pressure can be measured by applying the same principle as employed with the pitot-static tube. By measuring pressure perpendicular to the surface, the dynamic component can be excluded. The surface-static pressures can be measured by either placing small tubes or pressure taps through the skin of the body, or by using flush-mounted pressure discs. Care has to be taken to ensure that these devices do not produce local flow disturbances. As with the pitot-static tube, the tubes or discs are connected to a pressure transducer. After measurement, the pressures can then be reduced to non-dimensional pressure coefficients (C_P) as defined below[8].

$$C_P = \frac{P - P_\infty}{\tfrac{1}{2}\rho V_\infty^2}$$

where the reference static (P_∞) and dynamic pressures can be obtained using a pitot-static tube.

The aerodynamic forces can also be calculated from the surface pressures by surface integration, as defined by the following relationship[18]:

$$Dp = \oint p \sin\varphi\, dS$$

Although surface-static pressures can supply information regarding the flow on the surface of the vehicle, it is sometimes necessary to know what the conditions are at distances from the surface. The easiest method of achieving this, is to measure the total pressure using a pitot tube. Unfortunately, their construction and principle of operation limit their use. As with pitot-static tubes, pitot tubes also have to be aligned with the flow. Depending on their design, measurement errors can be incurred at misalignment angles of as little as 3 degrees[11]. Pre-existing knowledge of the flow is therefore required to ensure reliable results. A Kiel tube[11] is more suitable if prior knowledge of the flow field is unavailable, as flow angles in excess of 30° can still be measured with high degrees of accuracy.

The last of the pressure components, the dynamic pressure or flow velocity, can also be measured if required. One method of achieving this is to use a pitot-static tube. Unfortunately, despite the simplistic and robust construction of the tube, it is limited to use under free-stream conditions only. This is partly due to flow-angle sensitivity as described above, but more importantly, it is due to the sensitivity to static variations in the tunnel. The static fluctuations produced by the test object, can significantly influence the results if the tube is placed too close to the body under investigation.

To overcome the deficiencies of the pitot-static tube, multiple-component hot-wire probes can be used[18]. These probes work on the principle that the change in resistance due to cooling of electrically heated wires, can be related to the change in the air velocity responsible for the heat loss. Another method of determining the flow velocity is to use three, five or seven-hole probes. These probes can be described as an assembly of up to seven miniature pitot tubes, each tube measuring a component of total pressure. After measurement, these pressures are fed into a calibration matrix, where the magnitude of the velocity is determined in three dimensions. The precision and size of the calibration matrix is instrumental in determining the accuracy and maximum attainable flow angle.

2.2.2.3 Flow Visualisation

Flow visualisation techniques are used to observe different flow fields around a body[8,18]. They are used to gain qualitative rather than quantitative information and can be very cost effective.

One of the quickest, cleanest and most common methods employed are tufts. These are short, thin strips of string which when attached to the surface of the vehicle at one end, will align themselves with the airflow, thereby indicating local flow patterns. Other popular methods are lasers, smoke generators and oil-based fluorescent paints. The last two methods tend to soil the model and tunnel and are therefore usually only used at the end of a test series.

2.2.3 Wind-Tunnel Testing

One of the first decisions which has to be made when planning a wind-tunnel test programme, is the scale of the test model. When choosing the scale various factors have to be balanced. The operational and possible tunnel construction costs have to be considered. The amount of model detail and precision that is required, the ease and speed with which modifications can be made and the cost of manufacturing model components have to be taken into account. Finally, the desired accuracy of the results plays a major role in selecting the scale.

The first and often most obvious choice when considering the scale, would be to use full-scale models. Full-scale wind-tunnel testing is ideal, when the preservation of detail is important, as the actual vehicle under investigation or an identical model can be used. Full-scale testing does

however have several disadvantages. Vehicle transportation and tunnel installation, when using a model or purpose built racing car, can be expensive and cumbersome. Due to the size of the vehicle, component modifications can use up valuable tunnel time. Full-scale parts are also expensive to manufacture and can have long lead times. During the early phases of a project, sufficient detail is usually not available to warrant a full-scale vehicle. Furthermore, construction costs of the tunnel shell and power requirements tend to vary with the square of the tunnel width[11]. This means that a sedan-based racing car, which would require a tunnel with a cross-sectional area of more than 30 m², would need substantial initial investment and also a large operating budget. Currently, there are few tunnels in the world large enough for such tests and even fewer with the ability to simulate road conditions accurately. Full-scale tunnels are therefore usually only used for short test or verification programmes, while smaller-scale models are used when prolonged or continuous development is required.

When the scale of a car is changed it is important not only to reproduce the details of the vehicle, but also to duplicate the flow patterns and forces. The accurate scaling of the body and flow is achieved by a technique known as dimensional analysis.

2.2.3.1 Dimensional Analysis

Fluid flow problems can be characterised by fluid to fluid interactions and by the interaction of the fluid with its boundaries. In order to understand and compare similar fluid-flow phenomena and resulting forces originating under different physical conditions, it becomes necessary to remove the details of a particular flow problem, by non-dimensionalising the parameters defining the flow.[21] For most racing and passenger cars, where the flow is assumed to be incompressible, four non-dimensional relations are important. They are:

$$\text{Finess Ratio} \quad = \frac{L}{D} \quad = \frac{\text{Length}}{\text{Width}} \; ;$$

$$\text{Aspect Ratio} \quad = \frac{S}{W} \quad = \frac{\text{Span}}{\text{Width}} \; ;$$

$$\text{Relative Roughness} \quad = \frac{\varepsilon}{D} \quad = \frac{\text{Roughness Height}}{\text{Width}}$$

$$\text{Reynolds Number(Re)} \quad = \frac{\rho V L}{\mu} = \frac{\text{Inertial Forces}}{\text{Viscous Forces}}$$

Equation 2-7

where ρ is the density, μ is the viscosity, V is the characteristic velocity and L is the length of the vehicle. The first three ratios relate to the physical dimensions of the vehicle, while the fourth, the Reynolds Number, describes the interaction between the body and the fluid. If, when scaling, the full scale values of these ratios are applied to every component of the vehicle and flow, the case under investigation will be duplicated exactly, regardless of the scale employed. Unfortunately, this is rarely achieved. Fine detail and intricate body parts can disappear or not be viable to reproduce when reducing the scale. The surface roughness becomes in most cases impossible to scale as the full-scale surfaces are usually already at their practical minimum limits of smoothness. Although these problems diminish when the amount of detail on the full-scale vehicle is small, the Reynolds Number remains critically important.

External race car aerodynamics can as stated previously, be seen as fluid-flow problems where the flow is essentially incompressible. If the same working fluid is used for both the scale

model and the full-scale car, the Reynolds Number simply becomes proportional to the product of the size and speed of the vehicle. There are however, limits to where this simple product rule can be applied. When the Mach Number[11], defined as the ratio of the air speed to the speed of sound, rises above 0.3, the assumption of incompressibility becomes invalid and so additional corrections have to be made. Furthermore, physical limitations such as the attainable tunnel and rolling-road speeds also influence the maximum Reynolds Number. Scale-model tests are therefore usually performed at lowest possible Reynolds Numbers.

The Reynolds Number, not only defines, but also describes the type of interaction present at the solid-fluid boundary. As stated in section 2.2.1.2, a boundary layer is formed due to the viscous properties of the fluid. Initially, during the interaction, the fluid streamlines remain parallel and momentum exchange between layers is only on a molecular scale. This is known as laminar flow. Unless the free-stream fluid velocity or Reynolds Number is sufficiently low, this type of flow cannot be maintained and soon becomes turbulent. Here, considerable random motion and therefore, significant amounts of momentum exchange, exists between the different layers.

The transition from laminar to turbulent flow occurs at a finite distance from the leading edge of the surface. Therefore, as in the case of smaller scale models, if the length of the surface is reduced but the fluid properties are not adjusted, transition will still occur at the same absolute distance from the leading edge. This distance will however not be at the same relative position as on the full-scale case. This error is compounded even further if flow separation is present. The energetic nature of turbulent flow, will cause the point of separation to be postponed, resulting in a smaller wake than would be present in the laminar case. The body form therefore plays a major role in determining the sensitivity of the tests to the Reynolds Number.

Streamlined bodies such as tear-drop shapes are less sensitive to variations in the Reynolds Number, as the flow remains largely attached. Bluff bodies such as vertical plates are also insensitive as the separation point is fixed by the sharp edges. Unfortunately, cars which can be described as semi-streamlined or semi-bluff bodies, are very dependent on the Reynolds Number as there are few hard edges were the flow is forced to separate.

Tests performed by Barnard[16], showed that for a typical road car the critical Reynolds Number of $5x10^5$ corresponded to a 1/12th scale model at 25 m/s. He also found that for a Group C racing car, little variation in the drag was found above a Reynolds Number of around $9.6x10^5$. He found a 25% scale model tested at a velocity of about 40 m/s to be a popular choice. Tests performed in the Swift tunnel in the U.S.A. on a 40% scale model of a open-wheel racing car, suggested that speeds in excess of 60 m/s were needed to obtain reliable downforce figures.[22]

For the purposes of external aerodynamics, most of the internal components such as the engine and gearbox can also be scaled using dimensional analysis. The cooling pack can however not be scaled directly using this approach. A cooling core, disregarding the thermodynamic effects, influences the flow in two major ways. The first is a pressure drop due to the obstruction caused by the core and the second is the flow straightening effect created by the core fins. The simulation of these phenomena, at a smaller scale, are usually achieved by constructing a wire mesh and honeycomb sandwich. The wire mesh is chosen to represent the pressure drop while the honeycomb is used to straighten the flow. The density of the mesh can be calculated using the approach outlined by Masaru[23]. He used the core pressure drop, the porosity coefficient and Reynolds Number to determine the mesh density.

In summary, dimensional analysis can be used to reproduce fluid-flow problems at any scale. The size of the vehicle can therefore be changed, within limits, to fit the requirements of the test facilities. For any given wind tunnel, restrictions are placed on the maximum model size. The reasons for, and effects of these limitations, are presented below.

2.2.3.2 Wind-Tunnel Blockage Effects

When a model is placed into a closed-jet test-section wind tunnel, the walls form an unnatural boundary around the body. This forces the fluid stream lines in the test section closer together, producing higher test-section speeds which results in an over-estimation of the aerodynamic forces. This is known as solid or tunnel blockage. The proximity of the walls can also cause pressure reflections which affect the results even further.

The amount of blockage (B) is defined as the ratio of the cross-sectional area of the model to that of the empty test section[11]. To minimise the blockage errors, the walls of the tunnel have to be placed as far as possible from the model. Construction and operational costs limit the practical extent to which this can be applied. Hucho[18] suggests a blockage ratio of not more than 5%. In addition, tunnel-blockage correction factors, which vary from direct data manipulation such as continuity corrections, to more complicated computations involving pressure measurements along the test-section walls, are also employed. One such correction, which is based on continuity, is that as proposed by Sykes[24]. He performed a series of tests relating to cars and found, that for tests with a blockage of up to 20% and a yaw angle of up to 20°, the correction factor f, to be

$$f = \frac{C_{f,c}}{C_f} \text{ where } f = 1 - 1.9B$$

Equation 2-8

$C_{f,c}$ is the blockage corrected coefficient, C_f is the measured coefficient and B is the blockage ratio. The pressure coefficients can be corrected in a similar way by using the following formula:

$$f = \frac{1 - C_{p,c}}{1 - C_p}$$

Equation 2-9

where $C_{p,c}$ is the corrected pressure coefficient and C_p is the measured pressure coefficient.

Furthermore, the boundary-layer growth along the test section walls also influences the results. The boundary layer effectively reduces the test-section area towards the outlet. This decreases the static pressure along the test section which tends to draw the model downstream, changing the apparent drag. This effect, which is known as longitudinal or horizontal buoyancy[11], can be corrected by having slightly expanding test sections, using slotted walls or open-jet test sections. Empirical corrections to the drag, based on the pressure gradient along the test section, can also be employed.

All the factors discussed so far have to be taken into consideration when determining the size of the model, but usually, it is the availability of wind tunnels and operational funds which are

the overriding factors. Formula One teams, which are at the pinnacle of motor sport, use wind tunnels which can accommodate models ranging from 30 to 50% of full scale.

2.2.3.3 Model Mounting

The methods used to secure models in wind tunnels depend on the tunnel, balance and model types, as well as on the model size. For stationary-road tunnels, the wheels can be fixed directly onto the balance platform itself. For full-scale cars, the wheels and suspension are simply locked, as the weight of the car is usually enough to prevent movement.

The methods employed when rolling-road tunnels are used are more complicated, as the floor cannot be used to fix the models. Struts or wires, which protrude from the model, then have to be used. This arrangement, if pitch automation is not required, usually consists of a single main strut. The strut, which either extends from the top or rear of the model, connects the model to the external balance, or the internal balance to the tunnel frame. It also provides a concealed path for the cabling of control, data acquisition and measurement equipment.

If pitch or ride-height adjustments are required during a test run, additional tail struts or wires are needed for roof-mounted systems. Similar to the main strut, these also extend from the top or rear of the vehicle. Additional fixtures are however not required when a tail-mounted main strut is used, as the boom can be designed to accommodate height adjustments. The mounting struts do unfortunately create additional disturbances to the airflow. These can be summarised as follows:

- The direct contribution of the strut to the drag; called tare. This only applies to external balances.
- The additional blockage caused by the strut.
- The disturbance caused by the strut on the flow field of the model.
- The disturbance caused by the model on the flow field of the strut.

The last two categories are usually grouped together and are called interference. All these effects have to be removed by calibration.

The tare contribution can be reduced by shielding the strut from the airflow, but it cannot be eliminated entirely. The remaining contribution is determined by measuring the drag under operating conditions, with only the strut in the tunnel. The value measured during the tare run, is then subtracted from the model-drag values.

The interference, which is more difficult to determine, can be obtained using an additional balance[11]. In this approach, the model, while left in position, is disconnected from the main system and secured to the second balance. Two sets of data are recorded. The first is taken with the primary strut in position and the second is made without it. The difference between the two readings is taken as the total system interference and includes the tare contribution.

When a rolling-road system is used, the running wheels produce an additional contribution to the tare. This is caused by the stiction in the bearings and the friction between the belt and the wheels. This is determined by running the belt without the wind.

2.2.3.4 Wheels

The aerodynamic performance of racing cars and in particular open-wheeled types, are strongly influenced by the flow patterns created by their rotating wheels. This extends to all regions of

the body-work and includes areas such as engine and brake cooling systems[25]. It is therefore very important to reproduce these effects accurately.

The scarceness of full-scale rolling-road wind tunnels necessitates the use of stationary floors when scale models are not used. Under these conditions, the wake produced by open wheels under dynamic conditions, can be simulated by forcing separation before the apex of the tyre[18]. This arrangement attempts to reproduce the wake of the rotating wheel. The success and accuracy of this method still remains unclear. Various other methods[18] have also been investigated to improve the accuracy of wheel simulation using stationary or rotating wheels. Cogotti[26] found it essential to ensure zero gap between the wheel and the road, as the gap produced a venturi effect which changed the sign of the lift coefficient. Mercker et al.[25] could not find a fixed relationship between stationary and rotating wheel tests. Quantitative as well as qualitative errors could therefore be introduced by incorrect simulation.

During scale-model test programmes, the rolling-road system is still preferred. Besides the problems discussed in section 2.2.1.2 relating to rolling roads, several additional problems arise when wheel rotation is considered. The correct surface roughness of the tyre and road is very difficult to reproduce or to scale. The tyre profile is not symmetrical under dynamic loading on the track. The contact patch area is flat, while at the apex of the tyre, camber is present. As the contact patch is usually considered critical for simulation, the tyre camber has to be omitted. A flat running surface is also required to reduce belt wear.

The weight of the model wheels are also important. Heavy wheels can cause excessive belt wear, while light wheels can induce bounce or vibration which can influence the results. These can be overcome by mounting the wheels off the model, using a side-mounted strut system for each wheel. Unfortunately, this system requires additional balances to measure the drag of each wheel. The side struts also introduce aerodynamic interference which has to be removed. Ride-height adjustments become more difficult, as additional equipment is required to move suspension and brake-duct components. Wheel-steering studies do however become easier when the wheels are mounted off the model.

On a rolling road, wheel lift becomes very difficult to measure due to the interaction with the running surface. Mercker[25] devised a method whereby the lift of full-scale production vehicles could be measured.

2.2.3.5 Full-Scale Correlation

Ultimately all wind-tunnel tests have to be related to the racing car on the track. In the top open-wheel racing formulae, this becomes crucial as the aerodynamic coefficients form an integral part of the set-up of the car. Accurate correlation between the track and the tunnel is therefore required.

A Formula One racing car operates with ride heights typically ranging between 5 and 50 mm. When this gap is scaled for smaller model tests, track correlation becomes essential, as the air gap does not scale linearly. Additional ride-height adjustments therefore have to be made. When these corrections are made accurately, the top speed of the racing car can be predicted to within 1 mph and the downforce to within 1 lb.[27]

The success of any wind-tunnel programme, using the test methods and procedures as described in this chapter, can still be undermined by repeatability problems. Conclusions can

never be drawn from data, which have discrepancies smaller than the repeatability of the experiment. It is therefore essential, to construct precision models and test them in quality wind tunnels with highly repeatable systems.

2.3 Computational Literature Study

Computational Fluid Dynamics is the study of aerodynamic and fluid-mechanic problems using numerical solutions[28].

The governing fluid-flow equations and underlying assumptions are solved by discretising the equations and then implementing a numerical scheme over a predetermined solution domain. The governing equations are therefore discussed first. This is followed by the construction of the solution domain and finally, two different numerical-solution schemes are presented.

2.3.1 The Governing Equations

Fluids[ii] consist of molecules which are continuously in a state of random motion[29]. The large scale motion of fluids add a uniform velocity vector to the motion of each molecule. If the sample of molecules under investigation is large enough, the individual molecular motions are not detectable and so only the large scale motion needs to be investigated.

The governing equations of fluid dynamics are based on three universal laws of conservation[30]:
- Conservation of Mass (Continuity equation)
- Conservation of Momentum (Newton's Second Law)
- Conservation of Energy (First Law of Thermodynamics)

Although Navier and Stokes were only responsible for the equations relating to the conservation of momentum, all the governing equations are currently, collectively known as the Navier-Stokes equations. These equations can be expressed either in integral or differential form.

In integral form the conservation of mass over an arbitrary fixed control volume Ω can be expressed as:

$$\frac{\partial}{\partial t}\iiint_\Omega \rho d\Omega + \iint_S n \bullet \rho V dS = 0$$

Equation 2-10

or

$$\begin{pmatrix} \text{Net outflow of mass leaving the control} \\ \text{volume} \end{pmatrix} = \begin{pmatrix} \text{Time rate of mass change in the control} \\ \text{volume} \end{pmatrix}$$

where t is the time co-ordinate, ρ is the fluid density, V is the velocity vector, S is the boundary surface surrounding Ω and n is the unit normal vector to S. This equation is valid for any continuous perfect or real fluid.

[ii] A fluid can be defined as any substance which cannot sustain a shear force when at rest.

The conservation of momentum in integral form can be expressed over the fixed control volume Ω as:

$$\frac{\partial}{\partial t}\iiint_\Omega \rho V\, d\Omega + \iint_S \rho V\,(n\bullet V)\, dS = \iiint_\Omega \rho f\, d\Omega + \iint_S n\bullet T_{ij}\, dS$$

or

$$\begin{pmatrix} \text{Time rate of change in} \\ \text{linear momentum within} \\ \text{the volume} \end{pmatrix} + \begin{pmatrix} \text{The net flow of} \\ \text{momentum across} \\ \text{the volumes surface} \end{pmatrix} = \begin{pmatrix} \text{Body forces} \\ \text{e.g. gravity} \end{pmatrix} + (\text{Surface forces})$$

where f is the body force acting on the fluid per unit mass and T_{ij} is the total or Newtonian flow stress tensor. The Newtonian stress tensor is given by

$$T_{ij} = -\delta_{ij} p + \sigma_{ij}$$

where δ_{ij} is the Kronecker Delta defined as

$$\delta_{ij} = \begin{cases} 1, & i = j \\ 0, & i \neq j \end{cases}$$

and p is the fluid pressure characterised as a normal stress and σ_{ij} is the viscous stress tensor.

The momentum equation is valid for steady and unsteady flows of continuous liquids or **gases** which obey the assumptions of Stokesian and Newtonian fluids. Stokesian fluids obey four conditions:

- The fluid must behave as a continuum in which the stress tensor is only a function of the rate of the strain tensor and of the thermodynamic state of the fluid.
- The fluid must be homogeneous.
- The fluid must be isentropic.
- When the fluid is at rest the viscous stress tensor and the rate of the strain tensor must both vanish.

A Newtonian fluid is a fluid where the stress tensor is linearly proportional to the rate of the strain tensor.

Using the Stokesian-Newtonian fluid assumption as well as Stokes' hypothesis[31], as defined in Equation 2-14, the viscous stress tensor can be written as

$$\sigma_{ij} = \mu\left[\left(\frac{\partial u_i}{\partial x_j} + \frac{\partial u_j}{\partial x_i}\right) - \frac{2}{3}\delta_{ij}\frac{\partial u_k}{\partial x_k}\right]$$

or

$$\begin{pmatrix} \text{Viscous stress} \\ \text{tensor} \end{pmatrix} = \begin{pmatrix} \text{Normal and shear stress} \\ \text{due to fluid friction} \end{pmatrix} - \begin{pmatrix} \text{Normal stress contribution} \\ \text{to the fluids volume change} \end{pmatrix}$$

where μ is the first coefficient of viscosity, u and x are the Cartesian velocity and position co-ordinates respectively. i, j and k are in standard tensor notation, each cycled over 1, 2 and 3.

Stokes' hypothesis which states that the bulk viscosity which must vanish, is defined as

$$\mu' = \lambda + \frac{2}{3}\mu$$

The conservation of energy can be expressed in integral form as:

$$\frac{\partial}{\partial t}\iiint_\Omega E d\Omega + \iint_S n \bullet EV dS = \frac{\partial}{\partial t}\iiint_\Omega q_{ext} d\Omega - \iint_S n \bullet q dS$$
$$+ \iiint_\Omega \rho f \bullet V d\Omega + \iint_S n \bullet \left(T_{ij} \bullet V\right) dS$$

or

$$\begin{pmatrix} \text{Time rate of increase in} \\ \text{total energy per unit} \\ \text{volume in} \end{pmatrix} + \begin{pmatrix} \text{Net increase in total} \\ \text{energy per unit volume} \\ \text{by convection across S} \end{pmatrix} = \begin{pmatrix} \text{Time rate of increase in heat} \\ \text{added to } \Omega \text{ from sources} \\ \text{e.g. radiaton} \end{pmatrix}$$

$$- \begin{pmatrix} \text{Heat loss due to} \\ \text{conduction across S} \end{pmatrix} + \begin{pmatrix} \text{increase in energy due to the} \\ \text{work done on } \Omega \text{ by the body} \\ \text{forces} \end{pmatrix} + \begin{pmatrix} \text{Work done by the} \\ \text{stress tensor on S} \end{pmatrix}$$

The total Energy per unit volume (E) is defined as:

$$E = \rho\left(e + \frac{u^2 + v^2 + w^2}{2}\right)$$

e is the internal energy per unit mass, q_{ext} is the heat added from external sources and q is the heat flux due to conduction.

The heat conduction in a fluid is usually assumed to be governed by Fourier's heat conduction law which is defined as:

$$q = -k\nabla T$$

where k is the coefficient of thermal conductivity and T is the fluid temperature in an absolute temperature scale such as Kelvin.

If the body-force terms and the external-heat source terms are omitted, the conservation laws described above can be expressed in a special vector format:

$$\frac{\partial}{\partial t}\iiint_{\Omega} U d\Omega + \iint_{S}\left(F+G+H\right)\bullet n dS = \iint_{S}\left(F_{v}+G_{v}+H_{v}\right)\bullet n dS$$

where

$$U = \begin{bmatrix} \rho \\ \rho u \\ \rho v \\ \rho w \\ E \end{bmatrix};\ F = \begin{bmatrix} \rho u \\ \rho u^{2}+p \\ \rho uv \\ \rho uw \\ \left(E+p\right)u \end{bmatrix}i;\quad G = \begin{bmatrix} \rho v \\ \rho uv \\ \rho v^{2}+p \\ \rho vw \\ \left(E+p\right)v \end{bmatrix}j;\quad H = \begin{bmatrix} \rho w \\ \rho uw \\ \rho vw \\ \rho w^{2}+p \\ \left(E+p\right)w \end{bmatrix}k;$$

$$F_{v} = \begin{bmatrix} 0 \\ \sigma_{xx} \\ \sigma_{yx} \\ \sigma_{zx} \\ \beta_{x} \end{bmatrix}i;\quad G_{v} = \begin{bmatrix} 0 \\ \sigma_{xy} \\ \sigma_{yy} \\ \sigma_{zy} \\ \beta_{y} \end{bmatrix}j;\quad H_{v} = \begin{bmatrix} 0 \\ \sigma_{xz} \\ \sigma_{yz} \\ \sigma_{zz} \\ \beta_{z} \end{bmatrix}k$$

and

$$\beta_{x} = u\sigma_{xx}+v\sigma_{xy}+w\sigma_{xz}+k\frac{\partial T}{\partial x};\quad \beta_{y} = u\sigma_{yx}+v\sigma_{yy}+w\sigma_{yz}+k\frac{\partial T}{\partial y};$$

$$\beta_{x} = u\sigma_{zx}+v\sigma_{zy}+w\sigma_{zz}+k\frac{\partial T}{\partial z}$$

Equation 2-18

Q is the dependent or conserved variable vector. F, G and H are the inviscid flux vectors and F_v, G_v and H_v are the viscous flux vectors.

The first row of the vectors corresponds to the continuity equation. The second, third and fourth rows describe the momentum equations, while the last row represents the energy equation.

By transforming all the surface integrals to volume integrals using Gauss' Divergence theorem[31], the integral equations which were defined above can be transformed to a set of differential equations. When this is done the following flux-vector form of the differential equation results:

$$\frac{\partial U}{\partial t}+\frac{\partial F}{\partial x}+\frac{\partial G}{\partial y}+\frac{\partial H}{\partial z}=\frac{\partial F_{v}}{\partial x}+\frac{\partial G_{v}}{\partial y}+\frac{\partial H_{v}}{\partial z}$$

Equation 2-19

By inspection, it can be seen that the five equations presented in the integral or differential vector format above, contain seven unknowns (p, ρ, T, e, u, v, w). Two additional relations are therefore required to close the system of equations. This is achieved from the equation of state, by establishing a relationship between the thermodynamic variables (p, ρ, T, e), as well as to relate the transport properties (μ and k) to the thermodynamic properties. According to the state principle of thermodynamics, the local thermodynamic state is fixed by any two

independent thermodynamic variables, provided that the chemical composition is not changed due to diffusion or to finite rate reactions[30]. For example, if e and ρ are chosen as the two independent variables, equations of state of the following forms are required:

$$p = p(e,\rho); \qquad T = T(e,\rho)$$

2.3.2 Reynolds Equations for Turbulent Flows

The unsteady Navier-Stokes equations can be regarded as the governing equations for turbulent flow, but due to the space scales involved, computers are not yet capable of solving these equations directly for practical problems. A common estimate is that 10^5 grid points are required to resolve 1 cm^2 of a typical turbulent flow field[29].

An alternative approach to solving these equations directly is to break the dependent variables in the conserved equations, into time-mean and fluctuating components and then to take time averages of the governing equations. Currently the majority of turbulent research is directed towards the solution of these time-averaged or Reynolds-Averaged equations.

There are two time-averaging procedures currently in use. They are the standard or conventional and the mass or Favré averaging approaches. The mass-averaging approach is often preferred for compressible and external flows due to its compact form. For flows where the density fluctuations can be neglected, the two approaches become identical.

In the conventional averaging approach, the dependent variables are split into mean and fluctuating parts:

$$f = \overline{f} + f'$$

where

$$\overline{f} = \frac{1}{\Delta t} \int_{t_o}^{t_o + \Delta t} f\, dt$$

f is any dependent variable such a u or v. $\overline{f}$ represents the time-averaged or mean part and f' is the fluctuating component. Δt should be large compared to the period of random fluctuations in the turbulent flow-field, but small compared to the slower flow-field variations of ordinary unsteady flows.

In the mass-weighted averaging approach only the velocity and thermal variables are defined as:

$$\widetilde{f} = \frac{\overline{\rho f}}{\overline{\rho}}$$

The remaining variables are averaged as in the standard approach.

To simplify the Reynolds-Averaged Navier-Stokes Equations, it is assumed that triple correlations are smaller than double correlations and are therefore neglected. The fluctuating

components of viscosity, thermal conductivity and specific heat are usually small and are also neglected. The Favré-averaged Navier-Stokes equations can then be written as:

$$\frac{\partial U}{\partial t} + \frac{\partial F}{\partial x} + \frac{\partial G}{\partial y} + \frac{\partial H}{\partial z} = \frac{\partial F_v}{\partial x} + \frac{\partial G_v}{\partial y} + \frac{\partial H_v}{\partial z} + \frac{\partial F'}{\partial x} + \frac{\partial G'}{\partial y} + \frac{\partial H'}{\partial z}$$

Equation 2-23

where

$$U = \begin{bmatrix} \overline{\rho} \\ \overline{\rho\tilde{u}} \\ \overline{\rho\tilde{v}} \\ \overline{\rho\tilde{w}} \\ \overline{E} \end{bmatrix} ; F = \begin{bmatrix} \overline{\rho u} \\ \overline{\rho\tilde{u}^2} + \overline{p} \\ \overline{\rho\tilde{u}\tilde{v}} \\ \overline{\rho\tilde{u}\tilde{w}} \\ (\overline{E} + \overline{p})\tilde{u} \end{bmatrix} ; F_v = \begin{bmatrix} 0 \\ \tilde{\sigma}_{xx} \\ \tilde{\sigma}_{yx} \\ \tilde{\sigma}_{zx} \\ \tilde{\beta}_x \end{bmatrix} ; F' = \begin{bmatrix} 0 \\ -\overline{\rho u''u''} \\ -\overline{\rho u''v''} \\ -\overline{\rho u''w''} \\ -\overline{(E+p)u''} + \overline{\sigma_{xx}u''} + \overline{\sigma_{xy}v''} + \overline{\sigma_{xz}w''} \end{bmatrix}$$

The other fluxes are expanded in a similar way. The viscous stress tensor in is given by

$$\tilde{\sigma}_{ij} = \mu \left[\frac{\partial \tilde{u}_i}{\partial x_j} + \frac{\partial \tilde{u}_j}{\partial x_i} - \frac{2}{3} \delta_{ij} \left(\frac{\partial \tilde{u}_k}{\partial x_k} \right) \right]$$

Equation 2-24

The $-\overline{\rho u_i'' u_j''}$ and $-\overline{(E+p)v''}$ terms are new apparent turbulent stresses and heat-flux quantities. These are collectively known as Reynolds stresses. To close this system of equations, either additional equations involving the new unknowns have to be found, or assumptions have to be made which relate the new quantities to the time-mean flow variables. This is most often done with the use of turbulence models.

2.3.3 Turbulence Models

The turbulent-boundary layer is often sub-divided according to the dominance of the shearing action that is present[33]. In one definition, the laminar sub-layer is classified as the very small area next to the surface where viscous shear is important. The outer region, known as the fully turbulent zone, is defined as the layer where turbulent shearing is the overriding consideration. The region connecting the two zones is called the buffer zone. In another definition, the boundary layer is divided into two regions. Here, the inner region consists of the laminar sub-layer, the buffer zone and part of the fully turbulent zone. The remaining part of the turbulent boundary layer is then known as the outer region. In order to identify the upper limit of the inner zone a non-dimensional space co-ordinate, y^+ is used. This term is defined as:

$$y^+ = y \frac{u^*}{v}$$

Equation 2-25

where u^* is the friction velocity.

$u*$ is defined as:

$$u* = \left(\frac{\tau_\omega}{\rho} \right)^{\frac{1}{2}}$$

and τ_ω is the wall-shear stress

A popular estimate for the start of the outer region is a y^+ value of about 400[32].

Generally, turbulence models relate the fluctuating correlations to the mean-flow properties by empirical constants. As implied by the name, these schemes do not solve but only model the turbulent flow. Turbulence models can broadly be classified into two categories:
- Eddy-viscosity models
- Reynolds-stress models

Eddy-viscosity models use the Boussinesq approximation, while the Reynolds-stress models do not assume that the turbulent shearing stress is proportional to the rate of mean strain. Reynolds-stress models are more expensive computationally, as they solve a partial differential equation (PDE) for each of the turbulence terms and are therefore, currently not yet viable as engineering tools. As a result, eddy-viscosity models are the most widely used turbulence models for practical flows today.

The turbulent shear-stress is defined as the stress resulting from momentum exchange in the fluid. It is assumed that the fluid travels a finite distance before exchange takes place. This distance is named after its founder and is known as the Prandtl mixing length[32]. The Prandtl's mixing length concept is defined as[28]:

$$\mu_{turb} = \rho \ell^2 \left| \frac{\partial u}{\partial y} \right|$$

where ℓ, the mixing length is the distance away from the wall where particles maintain their original momentum and μ_{turb} is turbulent viscosity.

2.3.3.1 Eddy-Viscosity Models
The Boussinesq assumption relates the Reynolds stresses[28] to the mean flow quantities by

$$- \overline{\rho u_i'' u''}_{j} = \mu_T \left(\frac{\partial \tilde{u}_i}{\partial x_j} + \frac{\partial \tilde{u}_j}{\partial x_i} - \frac{2}{3} \delta_{ij} \frac{\partial \tilde{u}_k}{\partial x_k} \right) - \frac{2}{3} \delta_{ij} \rho k_T$$

and

$$-c_p \overline{\rho T'' u_i''} = k_{Tc} \frac{\partial \tilde{T}}{\partial x_i}$$

k_{Tc} is the turbulent conductivity which is related to the eddy viscosity by $k_{Tc} = c_p \mu_T / Pr_T$, where Pr_T is the turbulent Prandtl number, μ_T is the turbulent viscosity and k_T is the turbulent kinetic energy.

Substituting the Eddy-viscosity model equations into the Reynolds-averaged equations

$$\frac{\partial U}{\partial t} + \frac{\partial F}{\partial x} + \frac{\partial G}{\partial y} + \frac{\partial H}{\partial z} = \frac{\partial F_v}{\partial x} + \frac{\partial G_v}{\partial y} + \frac{\partial H_v}{\partial z}$$

yields the following:

$$U = \begin{bmatrix} \overline{\rho} \\ \overline{\rho \tilde{u}} \\ \overline{\rho \tilde{v}} \\ \overline{\rho \tilde{w}} \\ \overline{E} \end{bmatrix}; \quad F = \begin{bmatrix} \overline{\rho u} \\ \overline{\rho \tilde{u}^2} + \overline{p} \\ \overline{\rho \tilde{u} \tilde{v}} \\ \overline{\rho \tilde{u} \tilde{w}} \\ (\overline{E} + \overline{p}) \tilde{u} \end{bmatrix}; \quad F_v = \begin{bmatrix} 0 \\ \tilde{\tau}_{xx} \\ \tilde{\tau}_{yx} \\ \tilde{\tau}_{zx} \\ \tilde{\beta}_x \end{bmatrix} \quad \text{etc.}$$

Equation 2-30

and

$$\tilde{\tau}_{ij} = (\mu + \mu_T)\left[\frac{\partial \tilde{u}_i}{\partial x_j} + \frac{\partial \tilde{u}_j}{\partial x_i} - \frac{2}{3}\delta_{ij}\left(\frac{\partial \tilde{u}_k}{\partial x_k} \right) \right] - \frac{2}{3}\delta_{ij}\overline{\rho}k_T$$

$$\tilde{\beta}_x = \tilde{u}\tilde{\tau}_{xx} + \tilde{v}\tilde{\tau}_{xy} + \tilde{w}\tilde{\tau}_{xz} + (k + k_T)\frac{\partial \tilde{T}}{\partial x};$$

The same form as that of the laminar Navier-Stokes equations as defined in Equation 2-19 can therefore be retained.

It has been shown experimentally that for attached flows up to Mach numbers of five[32], the turbulent structure remains unchanged and is similar to that of incompressible flows. Under these conditions, density fluctuations can be neglected.

Eddy-viscosity models are generally classified according to the number of supplementary PDE's utilised. The most common models are zero and two-equation models.

In addition to the underlying Boussinesq assumption, zero-equation or algebraic models further assume that the local rate of turbulence production is equal to the rate of turbulence dissipation. These models also omit the convection of turbulence. A study performed by Marvin[33] suggests that algebraic models in their standard forms fail to capture the flow adequately when subjected to moderate-to-adverse pressure gradients. In certain cases, modifications to the standard model using a relaxation equation improved the situation somewhat, but the results were dependent on the choice of the relaxation length. The accuracy of solutions generated by algebraic models are strongly dependent on the type of flow field, the type of model and subsequent model modifications.

Unlike zero-equation models, two-equation models include the past history of the flow. This is achieved by deriving transport equations, which are based on the Navier-Stokes equations.

Unfortunately, the accuracy of these models are dependent on the assumptions made when evaluating the terms in the transport equations. This is a problem which is shared by all higher-order closure schemes. Research has therefore, been directed at improving the accuracy of the underlying assumptions and constants. These models are the most widely used eddy-viscosity models today.

The most popular two-equation model in current use, is the k-ε turbulence model or derivatives of it. These models solve differential transport equations for the turbulence energy (k) and dissipation rate (ε). The differences between most of these models lie in the form of the equations or the treatment of the near-wall region. In the standard version of the STAR-CD[3] model, high Reynolds-Number forms of the k and ε equations are used in conjunction with an algebraic "law of the wall" function.

Two variations of the standard k-ε model which are supplied by STAR-CD, are the Renormalisation Group (RNG) model and Chen's k-ε model. The RNG model is claimed[3] to be more accurate and general due to the fundamental nature of the approach. This model includes an additional term in the dissipation equation. Chen's variation of the k-ε model includes the production time scale and the dissipation time scale in closing the dissipation equation. This allows the energy transfer mechanism of turbulence to respond to the mean strain rate more effectively.

The STAR-CD version of the standard k-ε model is suitable for fully turbulent, incompressible or compressible flows. Buoyancy is also taken into account to a certain degree.

Wall functions are required as the k-ε models are not valid near the wall where molecular and turbulence effects are of the same order of magnitude. The following assumptions are made when wall functions are employed:
- One dimensional behaviour of the flow. Variations in velocity and other flow parameters are assumed to be normal to the wall.
- Uniform shear stress in the boundary layer. The effects of pressure gradient and body forces are assumed to be small.
- Shear stress and velocity vectors are unidirectional.
- The rate of the production of turbulence energy equals the rate of dissipation.
- Linear variation of the turbulence length scale.

The accuracy of the wall functions depends on the degree to which the assumptions and approximations as presented above, correlate to the physical problem.

Wall functions effectively provide turbulent-boundary conditions at the outer edge of the layer for the turbulent-transport equations. These are based on known distribution of velocity, temperature and turbulence parameters in a one dimensional contexts.

The alternative approach proposed by STAR-CD to using wall functions is to use low Reynolds-Number mixing-length models. The models calculate the turbulent viscosity by extending Prandtl's mixing-length hypothesis to three dimensions. Transport equations are therefore not required. A switch is made from the mixing-length model to the high Reynolds-Number turbulence model at a user defined distance from the wall. This distance should be in the range of $y^+ \approx 30$ to 150 to ensure that the normal k-ε transport equations

apply[3]. The switching criteria is based on the equality, within a specified tolerance, of the turbulent viscosity as calculated by the near wall and far-wall models.

Despite the extensive usage of the various k-ε models, Cambers and Wilcox[34] demonstrated two flaws for wall-bounded flows. They found the model to be ill-behaved when approaching a solid wall and inaccurate for flows with adverse pressure gradients. Attempts to correct this problem by introducing damping functions, have resulted in other deficiencies as stated by Yang and Shih[35]. They attempted to correct the problem of near-wall singularities, by developing a near-wall k-ε model. This model failed to capture the adverse pressure gradients properly.

To overcome the deficiencies of the various k-ε models, a significant number of alternative models have been developed. One of the more successful models to be developed was the k-ω model of Wilcox[36]. However, Menter[37] found this model to be strongly dependent on the value of the free-stream dissipation rate (ω_f), when applied to free-shear layers. He changed the eddy viscosity by as much as 100% by simply reducing ω_f. Despite this deficiency, the k-ω model is superior to the various k-ε models in other areas, as:

- No damping functions are required.
- Adverse pressure gradients are captured with higher accuracy.
- Simple Diriclet boundary conditions can be imposed.
- It is numerically more efficient and more stable. Wilcox[38] claims that the k-ω model is about 30% more efficient.
- Surface roughness and mass injection can be employed without changing the governing equations.

To eliminate the free-stream deficiency of the k-ω model, Menter[4] devised a model which he called the Baseline or BSL model. This model, although based on the k-ω, is a combination of the standard k-ω and k-ε models. The BSL model however, still suffered the same deficiency as all eddy-viscosity models, as the transport of the principle turbulent shear stress $-\overline{\rho u_i'' u_j''}$ was not accounted for. To include this within the framework of the eddy-viscosity models, Menter modified his BSL model to include the transport of turbulent shear stress. He called it the "Shear-Stress Transport" or SST model. Menter showed that the SST model correlated better to experimental data than the k-ε, k-ω and BSL models for a variety of flow situations. This method is discussed in more detail in Appendix A.

2.3.4 Grid Generation

The governing equations, whether in differential or integral form, are solved by discretising the equations over the flow field of interest. To achieve this, the computational domain has to be divided up into discrete points. A grid is therefore required.

Numerical algorithms and discretising procedures are best suited to be solved over uniformly-spaced orthogonal grids. These are difficult to achieve, as most physical flow problems have irregular boundaries. Interpolating procedures are therefore required at the perimeter. This generally means a loss in grid precision, but more importantly, a loss in computational accuracy becomes unavoidable. This problem can be overcome by transforming the irregular non-orthogonal physical domain to an equally-spaced orthogonal computational domain[32]. This also facilitates grid clustering in regions were high flow gradients are expected.

The general transformation that is used is an independent variable transformation from the physical domain (x, y, z), to the computational domain (ξ, η, ζ) involving non-orthogonal co-ordinates[39]. This transformation can be written as:

$$\tau = t$$
$$\xi = \xi(t, x, y, z)$$
$$\eta = \eta(t, x, y, z)$$
$$\zeta = \zeta(t, x, y, z)$$

<div align="right">**Equation 2-31**</div>

A unique single-valued relationship between the generalised and physical co-ordinates is assumed.

Using the chain rule of partial differentiation, the metrics of the transformation $(\xi_x, \eta_x, \zeta_x, \dots)$ can be expressed, after mathematical manipulation, in terms of primitive metrics $(x_\xi, x_\eta, x_\zeta, \dots)$ as follows[iii]:

$$\xi_x = J(y_\eta z_\zeta - y_\zeta z_\eta)$$
$$\xi_y = J(x_\zeta z_\eta - x_\eta z_\zeta)$$
$$\xi_z = J(x_\eta y_\zeta - x_\zeta y_\eta)$$
$$\eta_x = J(y_\zeta z_\xi - y_\xi z_\zeta)$$
$$\eta_y = J(x_\xi z_\zeta - x_\zeta z_\xi)$$
$$\eta_z = J(x_\zeta y_\xi - x_\xi y_\zeta)$$
$$\zeta_x = J(y_\xi z_\eta - y_\eta z_\xi)$$
$$\zeta_y = J(x_\eta z_\xi - x_\xi z_\eta)$$
$$\zeta_z = J(x_\xi y_\eta - x_\eta y_\xi)$$
$$\xi_t = -(x_\tau \xi_x + y_\tau \xi_y + z_\tau \xi_z)$$
$$\eta_t = -(x_\tau \eta_x + y_\tau \eta_y + z_\tau \eta_z)$$
$$\zeta_t = -(x_\tau \zeta_x + y_\tau \zeta_y + z_\tau \zeta_z)$$

<div align="right">**Equation 2-32**</div>

The last three equations can be rewritten using the first nine metric expressions

$$\xi_t = -J\left(x_\tau(y_\eta z_\zeta - y_\zeta z_\eta) + y_\tau(x_\zeta z_\eta - x_\eta z_\zeta) + z_\tau(x_\eta y_\zeta - x_\zeta y_\eta)\right)$$
$$\eta_t = -J\left(x_\tau(y_\zeta z_\xi - y_\xi z_\zeta) + y_\tau(x_\xi z_\zeta - x_\zeta z_\xi) + z_\tau(x_\zeta y_\xi - x_\xi y_\zeta)\right)$$
$$\zeta_t = -J\left(x_\tau(y_\xi z_\eta - y_\eta z_\xi) + y_\tau(x_\eta z_\xi - x_\xi z_\eta) + z_\tau(x_\xi y_\eta - x_\eta y_\xi)\right)$$

<div align="right">**Equation 2-33**</div>

[iii] Duplicated from: Craig, K.J., "Numerical Thermo Fluids - MSM780", Grid Generation Lecture Notes, University of Pretoria, 1994. Courtesy of Professor K.J. Craig

The Jacobian of the transformation, J, is defined as:

$$J = \frac{\partial(\xi,\eta,\zeta)}{\partial(x,y,z)} = \begin{vmatrix} \xi_x & \xi_y & \xi_z \\ \eta_x & \eta_y & \eta_z \\ \zeta_x & \zeta_y & \zeta_z \end{vmatrix} = \frac{1}{J^{-1}} = 1 \Big/ \frac{\partial(x,y,z)}{\partial(\xi,\eta,\zeta)} = 1 \Big/ \begin{vmatrix} x_\xi & x_\eta & x_\zeta \\ y_\xi & y_\eta & y_\zeta \\ z_\xi & z_\eta & z_\zeta \end{vmatrix}$$

$$= 1 \Big/ \left[x_\xi \left(y_\eta z_\zeta - y_\zeta z_\eta \right) - x_\eta \left(y_\xi z_\zeta - y_\zeta z_\xi \right) - x_\zeta \left(y_\xi z_\eta - y_\eta z_\xi \right) \right]$$

Equation 2-34

When these mapping procedures are employed the physical domain can be of an irregular nature without affecting the computational accuracy.

The success of the transformations do however place a number of constraints on the grid in the physical domain. These are summarised below:

- The mapping must be one to one. This will ensure, that grid lines of the same family do not cross.
- The grid lines should be smooth. This will ensure the continuous transformation of derivatives.
- The grid should have clustered points in the physical domain where large flow gradients are expected.
- Excessive grid skewness should be avoided.

These requirements have lead to the evolution of a number of grid topologies. In two dimensions these are known as the "C"-, "H"- and "O" grids. A number of techniques have been developed to construct these grids. The nature of the generation methods, make it possible to place them in different groups. These are:

- Algebraic methods
- Partial Differential methods
- Unstructured methods
- Adaptive methods

2.3.4.1 Algebraic Grid Generators

Algebraic grid generation methods are the least complicated techniques that can be employed. Although computationally fast, they are difficult to implement for complicated geometry. These meshes cannot always control interior skewness or smoothness. Discontinuities at the boundaries can also propagate into the interior, leading to errors caused by sudden changes in the metrics.

Algebraic methods employ interpolating schemes in order to obtain the boundary and interior cell points. If stretching algorithms are used for construction, grid clustering can easily be achieved. Stretching procedures can also be applied to ensure grid smoothness, when the grid is initially generated in multiple blocks. Multiple-block construction techniques become necessary when a combination of grid topologies are utilised, or when multiple obstacles are present in the domain.

Stretching functions range from simple geometric methods, where there is only control over the spacing of the first cell, to more sophisticated algorithms such as that of Vinokur[39]. He

employed hyperbolic relations to develop a two-sided procedure, giving control over the first and last spacing, the number of grid points as well as the total line distance.

To improve the orthogonal nature of algebraic grids close to solid boundaries, blending functions[40] can be used. Blending can be achieved in two steps. Firstly, by projecting an existing arc length onto a surface normal, and then by blending the existing grid and the surface normals. This procedure is outlined below.

$$x(\ell) = x_1(\ell)f_1 + x_2(\ell)f_2$$

<div align="right">**Equation 2-35**</div>

where

$$f_1 = \frac{2}{\pi}\tan^{-1}\left[\left(\frac{\ell}{L_t}\right)^p\right]$$

$$f_2 = \frac{2}{\pi}\tan^{-1}\left[\left(\frac{L_t}{\ell}\right)^p\right]$$

<div align="right">**Equation 2-36**</div>

L_t is the transition index, p is the power of the blending function, x_1 and x_2 are the generic co-ordinates of the original and projected points respectively and ℓ is the index. The number of intervals to blend, the transition index and the power of the blending function has to be specified.

2.3.4.2 Partial Differential Grid Generators

Partial Differential Equation grid generators, are the most commonly used among grid-generation methods because of their control capabilities. In these methods, the grid points in the physical space are solved based on a uniformly spaced grid in the computational domain. These methods[39] are categorised as elliptic, parabolic and hyperbolic systems of PDE's[iv].

Eliptic grid generators are currently widely used. These are suited to cases where all the boundaries of the domain are known. The boundaries can either be specified as grid-line slopes or as discrete grid points. The Thompson, Thames and Mastin (TTM)[41] method is one of the more popular schemes.

[iv] A second order PDE can be expressed in the following general format:

$$A\phi_{xx} + B\phi_{xy} + C\phi_{xy} + D\phi_x + E\phi_y + F\phi + G = 0$$

This general equation can be classified according to the to the sign of the expression $B^2 - 4AC$:

Elliptic if $\quad B^2 - 4AC < 0$

Parabolic if $\quad B^2 - 4AC = 0$

Hyperbolic if $\quad B^2 - 4AC > 0$

For the TTM method, the Poisson equations are used to transform the mesh from the physical to the computational domain. In 3D the equations can be written as:

$$\xi_{xx} + \xi_{yy} + \xi_{zz} = P(\xi,\eta,\zeta)$$

$$\eta_{xx} + \eta_{yy} + \eta_{zz} = Q(\xi,\eta,\zeta)$$

$$\zeta_{xx} + \zeta_{yy} + \zeta_{zz} = R(\xi,\eta,\zeta)$$

Equation 2-37

where P, Q and R are control functions

2.3.4.3 Unstructured Grid Generators

Algebraic and PDE grid generators create meshes where the cells in the physical domain remain adjacent to the same cells after transformation. This structured nature can make it difficult to generate very complex grids, or to create adaptive meshes. To overcome these deficiencies, a variety of techniques which are collectively known as unstructured grid-generation methods, have been developed. When these are employed, the grid points can be placed anywhere in the domain. The vertices are then connected to one another by a process known as tessilisation, resulting in tetrahedral-shaped cells when working in three dimensions.

2.3.4.4 Adaptive Grid Generators

The accuracy of any computational solution can be undermined by the ability of the grid to capture the flow field sufficiently. When the engineer generates a grid, he/she has to anticipate regions of high flow gradient and cluster the grid cells accordingly. As prior knowledge of the flow field is not always known, the concentration of cells might not be in the correct position to capture adverse gradients. Adaptive grids have the ability to ensure this by relocating the cells during the solution process. These mesh generators look at intermediate results and place cells where gradients are present. The grid does not stabilise until the steady state solution has been reached.

2.3.5 Numerical Solution Methods

The numerical solution of the governing fluid-flow equations can be divided into either space-marching, or time-marching schemes. Space-marching methods are designed to solve the governing equations where the flow is inherently stable. Time-marching methods on the other hand, can be used to obtain solutions for both steady state and time-dependent problems. Time-marching routines approach their steady-state solutions asymptotically with increasing time.

Marching schemes are solved by using either explicit or implicit algorithms. Explicit procedures are easy to implement and require the minimum number of operations per cycle. Although the implicit approach is more complicated, it is inherently more stable, meaning that larger time steps can be taken. These methods are therefore computationally more efficient.

Numerical methods which discretesize the differential form of the Navier-Stokes equations, are generally called finite-difference (FD) methods. Finite-volume (FV) methods are based on the integral form of these equations. The major differences between these two approaches are listed in Table 2-1.

Finite Difference	Finite Volume
$$\frac{df(x)}{dx} \approx \frac{f(x+\Delta x)-f(x)}{\Delta x}$$	$$\iint_S f dS \approx \sum_s f \Delta S$$
- Taylor series expansion is used. Δx is finite leading to a truncation error. - The power of Δx determines the order and therefore the accuracy of the method. - Variables are evaluated at the cell corners. - Special one-sided boundary treatment is required, as a row of grid points lie on the boundary. Once convergence is obtained the solution is known at the surface. - Free stream capture only through difference approximations.	S is the surface surrounding the volume V. - For non-uniform, non-orthogonal meshes care has to be taken when calculating cell face areas and cell volumes. - Variables are evaluated at the cell faces. - Slave cells are needed at all boundaries. These facilitate tangency and no slip implementation, but the solution at the surface has to be obtained through averaging. - Automatic free-stream capture capability.

Table 2-1 Differences between Finite-Difference and Finite-Volume Methods

From Table 2-1 it can be seen that finite differences can be grouped according to the order of the method that is used. Examples are shown in Figure 2-5 by graphically depicting a backward and a forward first-order case as well as a second order central-difference method.
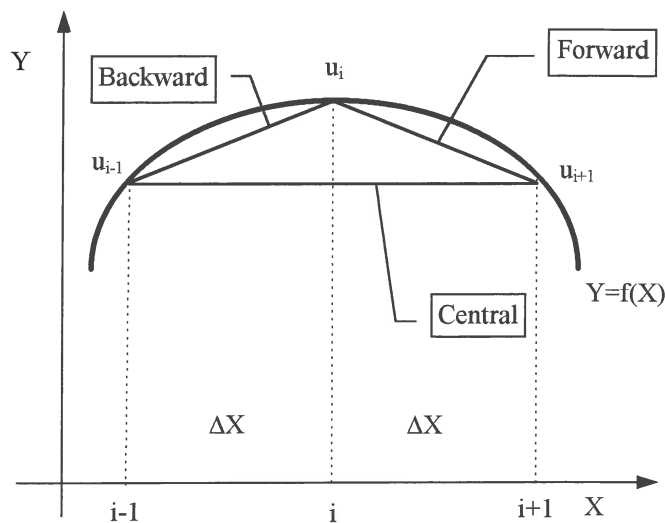
Figure 2-5 Difference schemes[28]

The numerical implementation of PDE's result in two classes of round-off errors. The first is a property of the numerical processor, while the second is caused by the discretising process. As the second inaccuracy is a function of the numerical scheme, the algorithm should be designed to ensure bounded and consistent errors. This means that the discrepancy should not only stay constant during the solution process, but also as the time and spatial increments tend towards zero, the difference equations should approach the differential equations. If these conditions are not met, numerical instability can result.

A few of the most likely causes of instability are listed below:
- Inconsistent spatial or temporal discretising schemes.
- Physically ill-posed boundary conditions.
- Inconsistent implementation of boundary conditions.
- Time or space-step size violations.
- Mismatch between the numerical and physical domains of dependence.
- The attempt to capture strong gradients with too little dissipation.

Numerical schemes have therefore not only been developed to increase numerical efficiency, but also to limit potential instabilities.

Two numerical schemes are used in this study. The first is Roe's Flux difference splitting method for the Full Reynolds Averaged Navier-Stokes Equations (RANS) and the second is the Semi-Implicit Method for Pressure Linked Equations (SIMPLE) by Patankar and Spalding[30].

2.3.5.1 Roe's Flux difference vector splitting for the Euler Equations

The 2D Euler equations, which are an inviscid case of the RANS equations, will be used to explain the concept of Roe's flux-vector splitting method as the physical interpretation of his method is not entirely clear[2]. These equations are used as they are less complicated but still representative of the full 3D RANS equations. The discussion of the Euler equations is conceptual in nature and the reader is referred to Appendix B for a detailed presentation of Roe's algorithm for the full RANS.

The 2D Euler equations, after transformation to the rectangular computational domain, can be written as[v]

$$\tilde{U}_t + \tilde{F}_\xi + \tilde{G}_\eta = 0$$
$$\tilde{U} = UV = UJ^{-1}$$

<div align="right">**Equation 2-38**</div>

where V is the volume of the finite volume element and corresponds to the inverse of the Jacobian of the transformation. This system of equations possesses the following properties[32]:
- The flux vectors are homogeneous
- The eigenvalues are real and can be positive and negative
- The sign of the eigenvlaues indicates the direction of data propagation
- The flux Jacobian matrices can be diagonalised

The algorithm used to explain Roe's procedure is given by

$$U_{i,j}^{n+1} = U_{i,j}^n + \Delta U_{i,j}^n$$

where

$$\Delta U_{i,j}^n = -\frac{\Delta t}{V_{i,j}}\left(\frac{D_+}{\Delta \xi}\tilde{F}_- + \frac{D_-}{\Delta \xi}\tilde{F}_+ + \frac{D_+}{\Delta \eta}\tilde{G}_- + \frac{D_-}{\Delta \eta}\tilde{G}_+\right)^n_{i,j}$$

<div align="right">**Equation 2-39**</div>

---

[v] Duplicated from: Craig, K., "Computational Fluid Dynamics - MBV780", Lecture Notes, University of Pretoria, 1994. Courtesy of Professor K.J. Craig.

The plus and minus fluxes in the ξ and η directions are determined using a suitable flux-splitting method. The two methods that are presented below are explained with the aid of Figure 2-6.
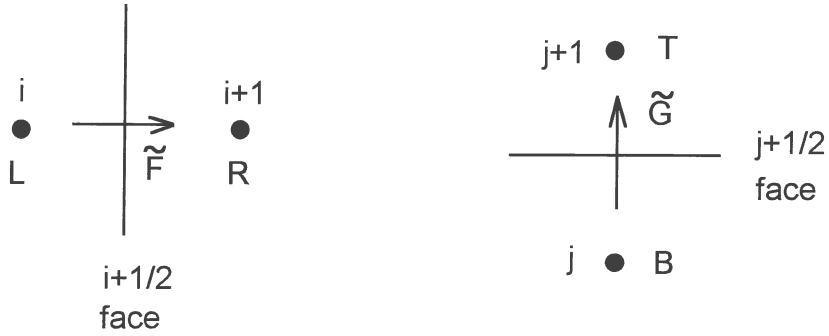

Figure 2-6 Fluxes through the cell face in two directions

Steger and Warming[28] formulated the characteristics theory[vi] into conservation law form by splitting the flux vector according to the sign of the characteristic speeds of the flow. By considering the schematic illustration in Figure 2-6 their methods of flux splitting in two directions can be written as[42]:

$$\widetilde{F}_{i+\frac{1}{2}} = \frac{\widetilde{F}_R + \widetilde{F}_L}{2} - \tfrac{1}{2}\left[\left(A_+ - A_-\right)U_R - \left(A_+ - A_-\right)U_L\right]$$

$$\widetilde{G}_{i+\frac{1}{2}} = \frac{\widetilde{G}_T + \widetilde{G}_B}{2} - \tfrac{1}{2}\left[\left(B_+ - B_-\right)U_T - \left(B_+ - B_-\right)U_B\right]$$

Equation 2-40

where A and B are the Jacobians of the transformation.

Roe[2] found that by using the geometric averages to split the fluxes, the characteristics could be captured in the right direction. Referring back to Figure 2-6, Roe's approach can be written as[42]

$$\widetilde{F}_{i+\frac{1}{2}} = \frac{\widetilde{F}_R + \widetilde{F}_L}{2} - \tfrac{1}{2}\left(\hat{A}_+ - \hat{A}_-\right)\left(U_R - U_L\right)$$

$$\widetilde{G}_{j+\frac{1}{2}} = \frac{\widetilde{G}_T + \widetilde{G}_B}{2} - \tfrac{1}{2}\left(\hat{B}_+ - \hat{B}_-\right)\left(U_T - U_B\right)$$

Equation 2-41

where $\hat{A}$ and $\hat{B}$ are the *geometric-averaged* Jacobians. Sudden changes, such as shock waves could be apprehended with higher accuracy by using Roe's method.

Using Roe's method the algorithm of Equation 2-39 can now be re-written as

$$\Delta U_{i,j}^n = -\frac{\Delta t}{V_{i,j}}\left(\frac{\widetilde{F}_{i+\frac{1}{2}} - \widetilde{F}_{i-\frac{1}{2}}}{\Delta \xi} + \frac{\widetilde{G}_{j+\frac{1}{2}} - \widetilde{G}_{j-\frac{1}{2}}}{\Delta \eta}\right)^n_{i,j}$$

Equation 2-42

[vi] The precise treatment of the flow physics in the classic method of characteristics was lost during the early development of finite difference procedures.

Splitting of the Jacobians $\hat{A} = \hat{A}_+ + \hat{A}_-$ and $\hat{B} = \hat{B}_+ + \hat{B}_-$ of Equation 2-39 is through polarity of the rotated eigenvalues. As the eigenvalues and associated eigenvectors are real, the Jacobian can de diagonalised. A similarity transformation therefore exists such that[32]

$$\widetilde{A}_{\pm} = X^{-1}\Lambda_{A_{\pm}}X$$
$$\widetilde{B}_{\pm} = X^{-1}\Lambda_{B_{\pm}}X$$

where Λ is a diagonal matrix of eigenvalues of $\widetilde{A}$ and X is the eigenvector matrix. Λ_+ and Λ_- are then determined by

$$\Lambda_+ = \frac{\Lambda + |\Lambda|}{2}$$
$$\Lambda_- = \frac{\Lambda - |\Lambda|}{2}$$

Equation 2-43

As stated previously, a thorough presentation of Roe's algorithm for the full 3D RANS equations is given in Appendix B. In the appendix it is seen that the algorithm is expanded from a thin-layer procedure. This was necessary as the underlying assumptions of the thin-layer approach does not necessarily hold for bluff bodies such as racing cars where large areas of separation is expected. The thin-layer equations are designed for flow cases where the normal-stress gradients are much larger than the streamwise and circumferential gradients[32].

2.3.5.2 The SIMPLE Algorithm of Patankar and Spalding

The incompressible SIMPLE algorithm for the Navier-Stokes equations is used as implemented by STAR-CD[3]. This procedure is based on a cyclic series of guess-and-correct operations. The velocity components are first calculated from the momentum equations using a guessed pressure field. The pressures and velocities are then corrected so as to satisfy continuity. This process continues until the solution converges. The outline of the SIMPLE algorithm is presented below:

- Guess the pressure at each grid point.
- Solve the momentum equations to find the intermediate velocity components.
- Solve the pressure-correction equation at each grid point to find the pressure corrections.
- Correct the pressures and velocities.
- Replace the intermediate values of pressure and velocity with the new corrected values.
- Repeat the process until the solution converges.

2.3.6 Boundary Conditions

In order to obtain a unique solution for the PDE's, two supplementary sets of conditions are required. These are initial and boundary conditions.

Initial conditions are required as the dependent variables have to be specified at some initial state. Fortunately, the dependency on these vanish as the solution evolves through time.

The relations which the dependent variables or their derivatives have to satisfy on the edge of the solution domain, are known as boundary conditions. As the outcome of the solution depends on these, it is vital to specify them correctly.

Boundary conditions can be specified in two basic ways:
- Dirichlet boundary conditions, where the dependent variables are specified along the boundary.
- Neumann boundary conditions, where the normal gradients of the dependent variables are specified.

Irrespective of the way in which boundary conditions are specified, they still have to relate to the physical-flow problem. They can therefore, depending on the prevailing flow conditions, be classed as follows:
- Impermeable boundaries
- Axis of symmetry or reflection boundaries
- Entrance and Exit boundaries

2.3.6.1 Impermeable Boundaries

Impermeable boundaries are constraints such as solid walls, where the flow has to be parallel to the surface. For viscous flow fields, velocity, pressure and wall temperature relations can be as specified in Table 2-2.

Independent Variable	Boundary Condition	Boundary Type	Description
Pressure	$\dfrac{\partial p}{\partial n} = 0$	Neumann	One-dimensional boundary layer equation
Velocity	$u_n = 0$ $u = 0$	Dirichlet	Tangential flow No-slip condition
Temperature	$k\dfrac{\partial T}{\partial n} = 0$ $T = T_{wall}$	Dirichlet Neumann	Adiabatic wall Isothermal wall

Table 2-2 Impermeable Boundary Conditions

where n is the unit normal vector.

A study by Mazeheri and Roe[43] suggested that the assumptions of one-dimensional analysis and waves travelling normal to the boundaries, were not always valid. They also showed that the path to convergence followed a simple, well-defined repetitive pattern, characterised by the passage of acoustic waves travelling between the inner and outer boundaries. Based on this, they proposed a new "soft wall" boundary condition. In the steady limit this coincided with the conventional rigid boundary. They found that by replacing

$$u_n = 0$$

with

$$\frac{\partial u_n}{\partial t} + \frac{u_n}{\tau} = \frac{\mu}{\rho a}\frac{\partial p}{\partial t}$$

Equation 2-44

the computational time could be reduced by more than 40% for two-dimensional lifting flows. μ and τ are parameters chosen to minimise reflected disturbances. They found that μ could roughly be set equal to 0.5 as the precise value was not very critical. The parameter τ is loosely bounded by two considerations. The value should not be much less than the time step and secondly, it should not be greater than the time for a round trip of a wave crossing the domain.

2.3.6.2 Reflection Boundaries

Reflection boundaries can be employed when the flow is symmetrical around a line or plane. By definition this means that the flow cannot cross, or have any gradient normal to the boundary. These conditions are expressed in mathematical form in Table 2-3.

Independent Variable	Boundary Condition	Boundary Type
Pressure	$\dfrac{\partial p}{\partial n} = 0$	Neumann
Velocity	$\dfrac{\partial u}{\partial n} = 0;$ $u_n = 0$	Neumann Dirichlet
Temperature	$\dfrac{\partial T}{\partial n} = 0$	Neumann

Table 2-3 - Reflection Boundary Conditions

2.3.6.3 Entrance and Exit Boundaries

To implement the inflow and outflow boundary conditions for the RANS equations, it is easiest to look at the hyperbolic Euler equations. For this type of PDE, there has to be as many boundary conditions as there are characteristics. The two-dimensional characteristics for the Euler equations are plotted Figure 2-7[v] for a subsonic flow field.
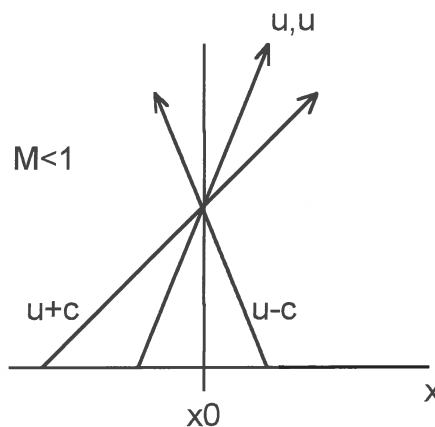

Figure 2-7 - Characteristics for the subsonic Euler equations

Characteristics originating from inside the domain do not have to be specified, as they can be resolved internally. From Figure 2-7, it can be seen that three external boundary conditions have to be specified at the inlet, while only one is required at the outlet. These values are normally determined through measurement. For external-flow problems, the computational

domain can be constructed so that the inlet and outlet boundaries are far from the body under investigation. Free-stream conditions can then be specified.

Wei Shyy[44] developed an alternative approach to specifying the unknown outlet condition. He calculated the remaining characteristic using a line-iterative method based on the internal flow. He proposed four different methods:

Explicit step space extrapolation - $\Phi_{NI,j}^{n+1} = \Phi_{NI-1,j}^{n}$ **Equation 2-45**

Implicit step space extrapolation - $\Phi_{NI,j}^{n+1} = \Phi_{NI-1,j}^{n+1}$ **Equation 2-46**

Explicit linear space extrapolation - $\Phi_{NI,j}^{n+1} = 2\Phi_{NI-1,j}^{n} - \Phi_{NI-2,j}^{n}$ **Equation 2-47**

Implicit linear space extrapolation - $\Phi_{NI,j}^{n+1} = 2\Phi_{NI-1,j}^{n+1} - \Phi_{NI-2,j}^{n+1}$ **Equation 2-48**

where NI refers to the right-boundary index, n is the iteration number, and Φ is any of the flow variables.

He found the implicit linear space extrapolation method to be computationally expensive, and that a unique solution was not always guaranteed. The explicit zero-order space extrapolation method appeared to be the most robust.

2.4 Conclusion

The aim of this chapter was to introduce the reader to experimental and numerical road-car aerodynamics and to present him/her with a summary of the existing techniques and methods, as found in the literature.

As an introduction, the history of racing cars, with the accent on aerodynamics, was briefly presented. This was followed by a more detailed discussion on the aerodynamics of modern racing cars. General Aerodynamic relationships and experimental techniques followed. Finally, the computational techniques were outlined.

Some of the techniques and methods included in this chapter were presented in "lay-man" terms. Certain elements had no direct bearing on the case studies presented in later chapters. The author felt that at the time of his introduction to race-car aerodynamics a few years ago, there was a large gap between "beginner" literature and highly technical reports. The author also found the information segregated and very few books, such as the one by Katz[8], were dedicated exclusively to race-car aerodynamics. It was therefore the intention to present a more complete picture in moderately technical terms, than was required for this study.

3. THE FLOW BENEATH A FORMULA ONE RACING CAR

The floor of a Formula One racing car is potentially an area where notable aerodynamic gains can be made. The floor can roughly contribute a third of the total downforce[27]. In addition, the pressure distribution under the floor also influences the centre of pressure and related pitch sensitivity of the car. An understanding of these flow patterns and resulting forces can therefore be very useful in optimising aerodynamic performance. The flow beneath an F1 car was therefore investigated.

For this research project, a 30 % scale model of the Parmalat Forti Ford FG01-95 F1 racing car was used. The full-scale car was raced in the 1995 F.I.A. governed[45] F1 world championship.

Both experimental and numerical techniques were used. The experimental part of this study was aimed at capturing the 3D flow field, while the numerical side was directed at reproducing the floor centre-line pressure distribution.

To curb the high levels of traction obtained using *ground effects*, the F.I.A. have laid down strict rules governing the shape of the car floor. Although these rules[45] have not been repeated here, the "rule box" is presented in Figure 3-1. This is the envelope into which all sprung parts of the car have to fit. It has been inverted to show the floor area.
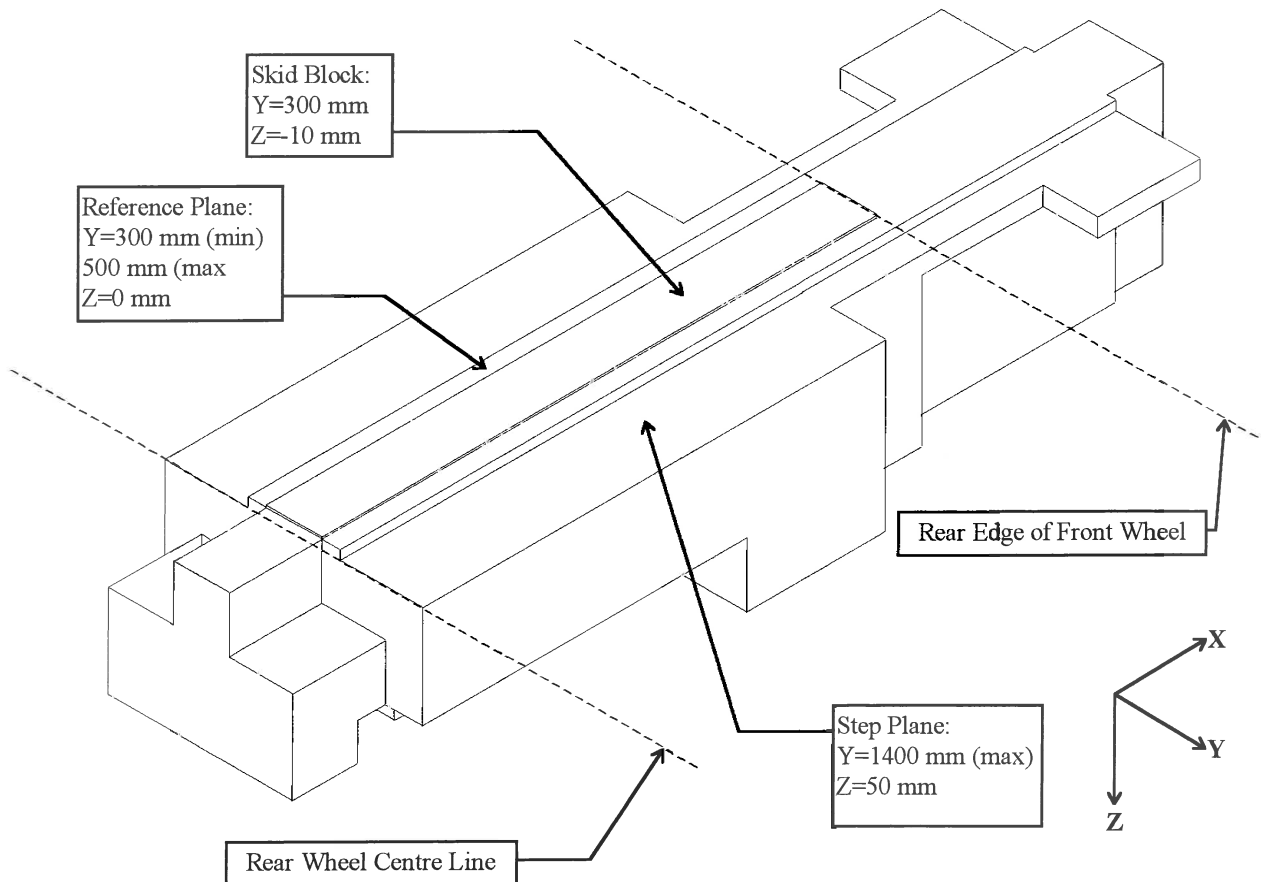

Figure 3-1 Representation of the 1995 FIA Formula One Rule Box

The resulting car floor, designed using the constraints of Figure 3-1, is shown in Figure 3-2.
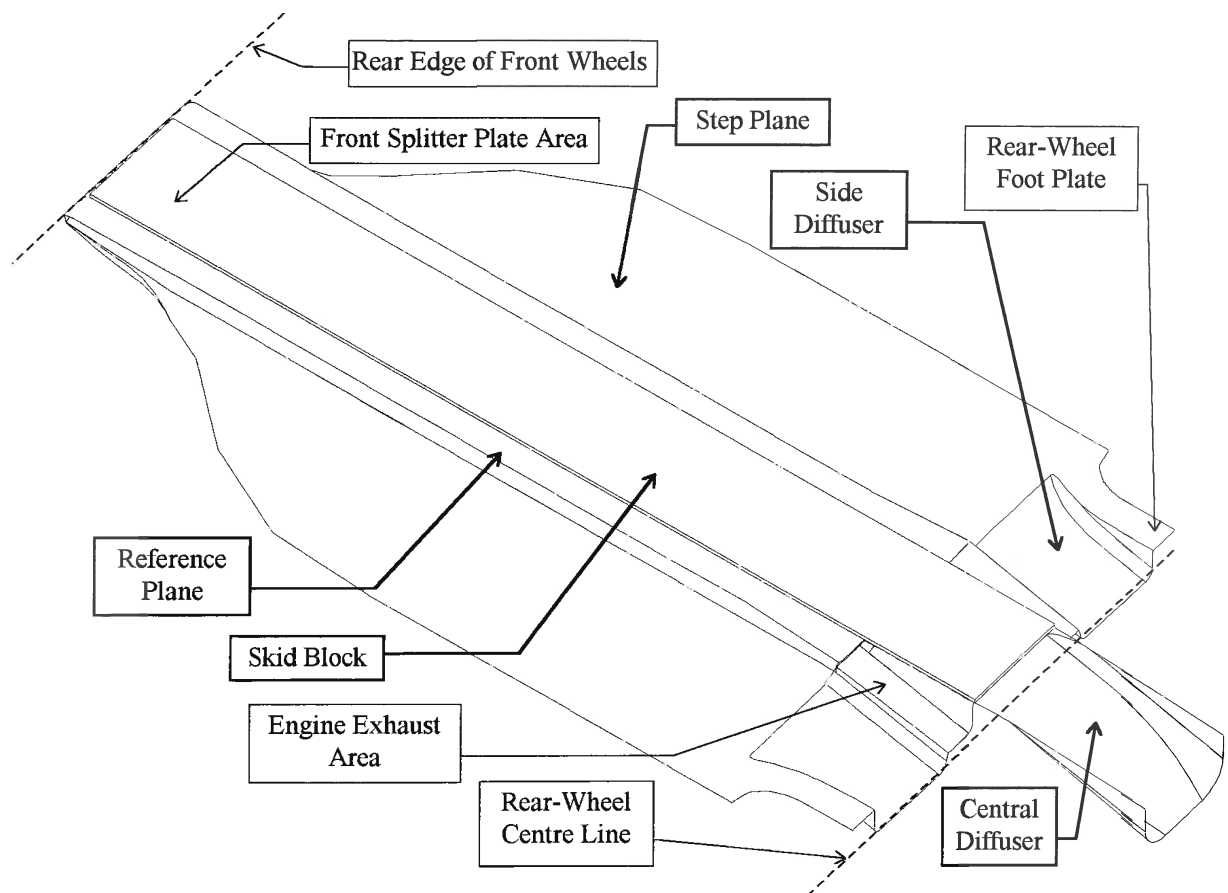

Figure 3-2 Inverted view of the floor

3.1 Experimental Investigation

The experimental investigation was aimed at characterising the centre-line flow pattern and then determining which factors, external to the floor, were predominantly responsible for the 3D pressure distribution under the floor of the car. This was achieved by using a baseline model as a reference and then varying certain parameters. As the fundamental flow pattern was the sole concern of this study, the model changes were selected to induce large shifts in the pitch and downforce of the car. Three sets of experiments were chosen to satisfy this criteria. These were:

- Model ride height and angle of attack variations
- Front-flap angle adjustments
- Front and rear wheel assessments

The experimental tests were also used to obtain data for the numerical investigation as presented in section 3.2.

3.1.1 Experimental Set-up

The closed-return LSWT at the Council for Scientific and Industrial Research (CSIR) in South Africa was used for the tests. The wind tunnel had a 1.5x2.1x3.7m closed test section and was equipped with a rolling road. The maximum obtainable belt speed was 30 m/s. The wind tunnel was also equipped with an overhead six-component virtual-centre balance.

The blockage ratio, as defined in section 2.2.3.2 was calculated to be 4.1%. All tests were performed at 24 m/s. Using the length of the model as the characteristic length, the Reynolds Number was in the range of 5×10^6. This satisfied the criteria of Barnard[16] for Reynolds-Number independence as discussed in section 2.2.3.1. A picture of the model, mounted in the tunne, is shown in Figure 3-3.
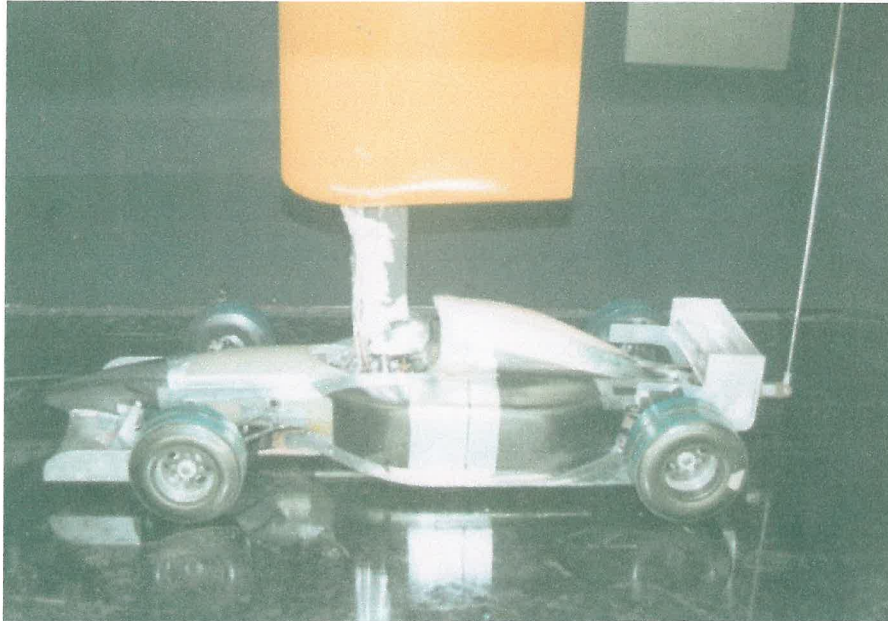
Figure 3-3 Set-up of the car in the wind tunnel

For ease of comparison with numerical data, all tunnel correction factors were removed.

The body parts of the model were made of glass and carbon fibre reinforced plastic (CFRP) using CNC machined moulds. The front and rear wings and flaps, spine, and wishbones were made of aluminium. The carbon fibre wheels were covered with a smooth, non-stick surface. The wheels were dynamically balanced before the start of the investigation. Internally, the model had a representative engine, gearbox, air intake and exhaust as well as scaled radiators. Ride height, front flap and rear wing adjustments were automated using internal stepper motors.

The CFRP floor was fitted with 92 pressure taps at locations shown in Figure 3-4. The longitudinal centre line was assumed to be the line of flow reflection.

The surface pressure tappings were constructed by drilling small holes perpendicular to the relevant surfaces and inserting metal tubes which were fixed flush to the surface to ensure no flow interference. The metal tubes were connected to two Scanivalve[vii] pressure transducers via plastic tubes. Due to the large number of plastic tubes, the Scanivalves were mounted inside the model so that only the six control cables (3 per Scanivalve) had to be taken from the model.

[vii] The Scanivalves that were used each contained a single pressure transducer with a manifold-type head which accommodated up to 48 pressure taps. All pressures were measured relative to a datum pressure. Each pressure port was measured sequentially by aligning the 48 ports with the transducer. The measured voltage signals were sent to a central processing unit where they were converted and non-dimensionalised to pressure coefficients (C_P).
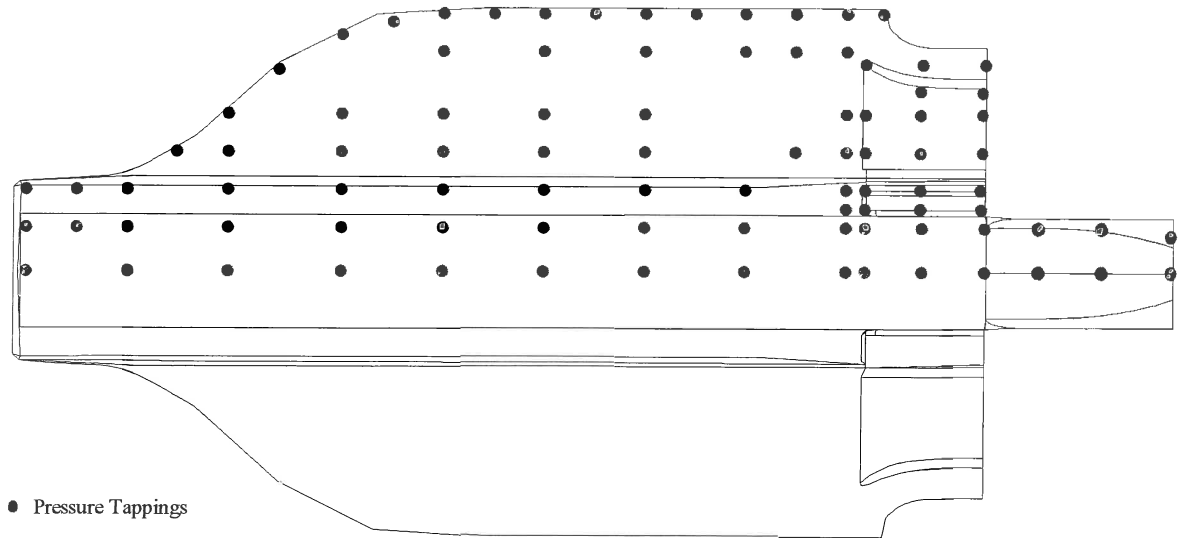
● Pressure Tappings

Figure 3-4 Location of pressure taps under the car floor

The wheels were mounted onto the model. Figure 3-5 shows detail of the model, the spine, the wheels, the two Scanivalves and the concealed pressure tappings.
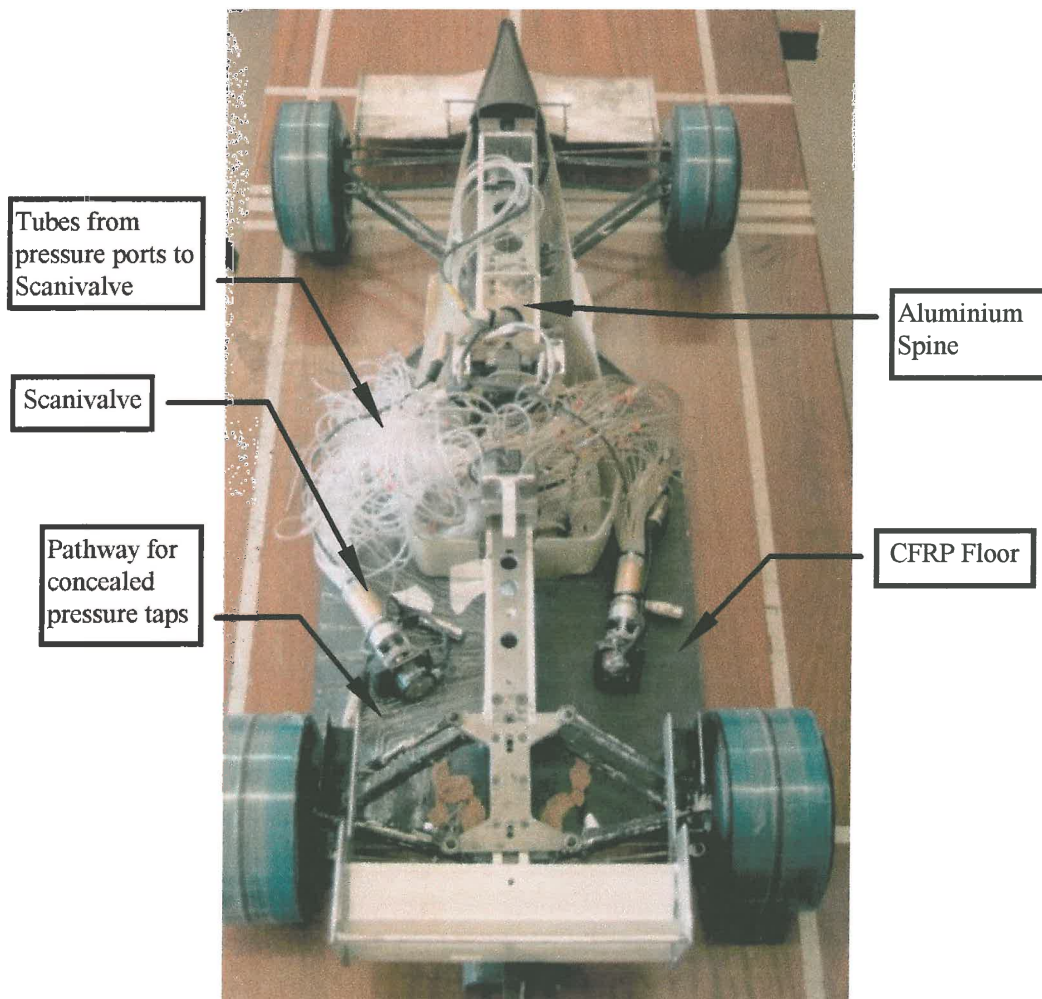

Tubes from pressure ports to Scanivalve

Scanivalve

Pathway for concealed pressure taps

Aluminium Spine

CFRP Floor

Figure 3-5 Model Construction

The adjustable components of the base-line model were fixed as summarised in Table 3-1. These remained unchanged throughout the study unless specified.

Model Parameter	Abbreviation	Value
Basic Model Configuration	-	Standard model
Front Ride Height (Full Scale - FS[viii])	FRH[ix]	20 mm
Rear Ride Height (Full Scale - FS)	RRH	40 mm
Front Flap Angle	FFA	9.3°
Rear Wing Angle	RWA	31°

Table 3-1 Model set-up

As an indication of the aerodynamic sensitivity to changes in the parameters listed in Table 3-1, the overhead balance was used to obtain coefficients for the complete vehicle. A 20 mm FS change in RRH would affect the COP by 5% when compared to the baseline case. Changing the FFA by 3 degrees shifted the COP by approximately 5 %. A 15 degree change in RWA changed the downforce by about 100 kg's.

3.1.2 Experimental Results

The experimental results below, are all based on pressure coefficients obtained from the scale model floor.

3.1.2.1 Repeatability

To illustrate the repeatability of the wind tunnel and model set-up, two sets of data were used. These were obtained on separate test days. The model had been modified between the two runs and was brought back to the specification as described in Table 3-1, before the second run was made. The repeatability, as summarised in Table 3-2 was only calculated for the pressure tapping. The overhead balance was not used during the tests.

Variable calculated	Result
Mean Pressure coefficient of Run 1 (C_P over 92 taps)	-1.6556
Mean Pressure coefficient of Run 2 (C_P over 92 taps)	-1.6628
Mean difference between Runs	0.0072
Mean difference expressed as a percentage (%)	0.4330

Table 3-2 Results of repeatability calculations

From the table it is evident that high levels of repeatability were achieved. Differences of less than 0.43% would have to be interpreted as repeatability errors and not as aerodynamic changes.

[viii] FS   - Full Scale dimensions
    MS - Model Scale dimensions
[ix] The terms front (FRH) and rear (RRH) ride height are defined as the air gap between the front and rear wheel centre lines respectively.

3.1.2.2 The Centre-Line Flow Pattern

As an introduction to the flow pattern beneath the vehicle, the centre-line pressure distribution of the baseline car is presented first.

The basic shape of a centre-line pressure distribution curve is found to be common to many smooth-bottomed, open and closed-wheel racing cars fitted with front splitters and rear diffusers[8,13]. The centre-line pressure plot of the stepped Forti floor, as presented in Figure 3-6, also exhibits these characteristics.

By inspection, the profile in Figure 3-6 can be divided into three separate curves connected by two inflection points. These can be linked directly to three physical zones on the car as shown in the figure. Zone I represents the front splitter. As found by Dominy[7], the stagnation point induced by the splitter and the proximity of the body, causes the flow to accelerate and then to diffuse downstream of the stagnation point. This is clearly indicated by the slope of the curve in Zone I.
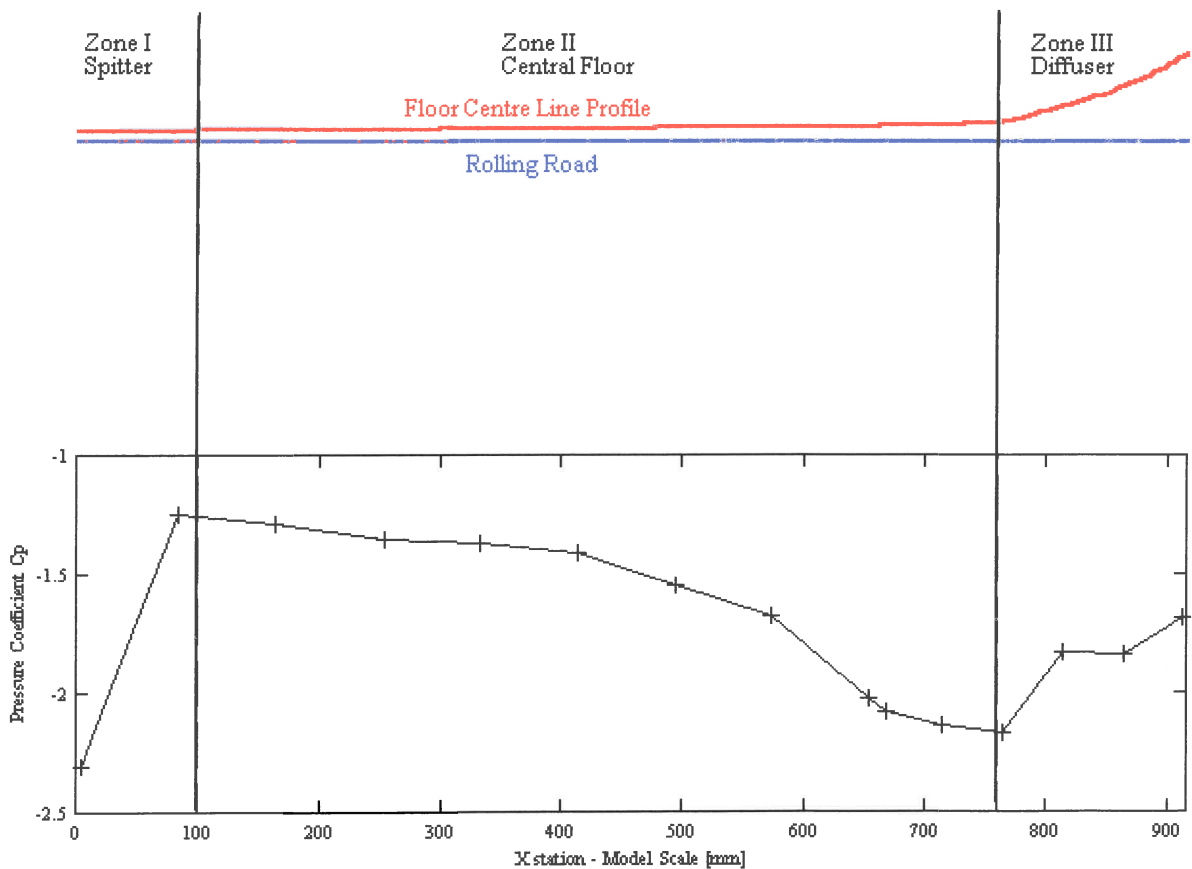
Figure 3-6 Centre-line pressure coefficient plot of the baseline set-up

Flow acceleration and diffusion are also responsible for the characteristic diffuser curve as seen in zone III. The transition from the central floor to the angled diffuser causes an area of local flow acceleration, inducing a sharp static-pressure drop. The maximum diffuser angle and corresponding negative pressures in this area are limited by the momentum of the air. Too steep an angle will cause separation, corresponding to a loss in downforce. The momentum of the air can be increased by matching the diffuser with the rear-wing assembly. When this is done correctly, the rear wing acts as a pump, energising the air and prolonging separation.

Higher diffuser angles can then be attained. As can be seen from the position of the inflection point in zone II, the effect of the rear-wing assembly and diffuser is more pronounced than the front-splitter.

Extending the conclusions regarding the shape of the pressure profile to positions away from the centre line is not obvious, as a racing car and especially a Formula One car is a highly three dimensional body. This is illustrated by the 3D pressure map in Figure 3-7[x] and the contour plot in Figure 3-8.

As anticipated, examination of the two figures reveals significant differences at stations away from the centre line. Most notable is the diffuser area which consists of a central diffuser, two side diffusers and two smaller exhaust diffusers. The transition from the reference plane to the step plane also has an influence on the contours. Other areas which are notably different, are the floor-edge area below the cooling intakes and the area immediately in front of the rear diffuser. Higher than average pressure peaks are clearly visible.
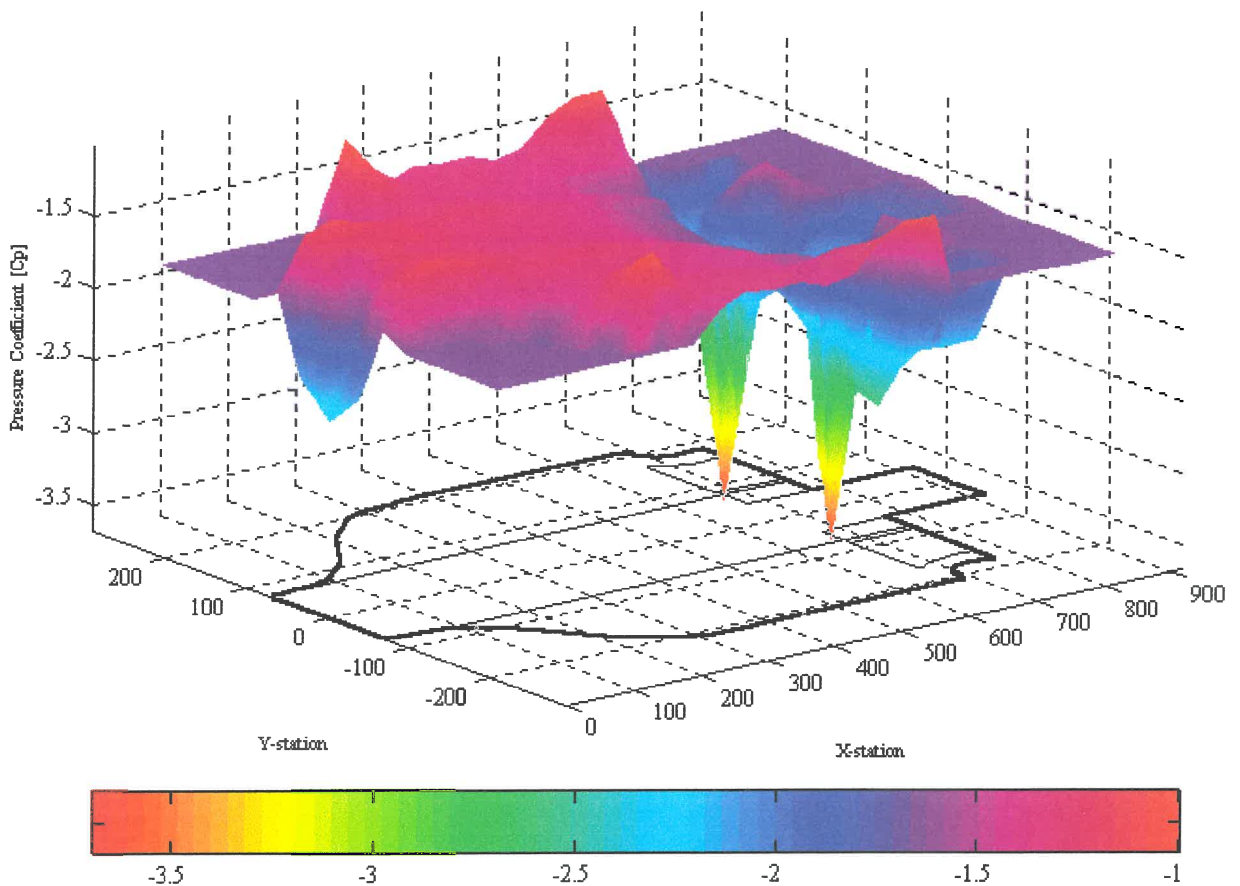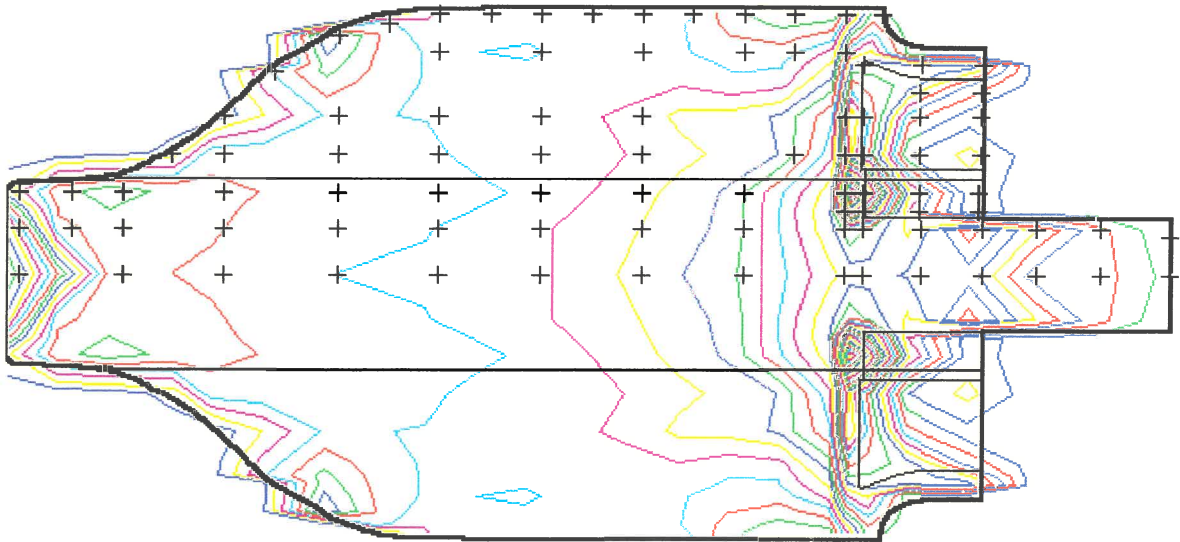

Figure 3-7 Pressure map of the floor - Baseline Model

---

[x] The planar area (blue/purple) of the pressure map lying outside the boundaries of the floor represent the correct position of the average pressure coefficient.

Figure 3-8 Pressure contour plot of the floor - Baseline Model

3.1.2.3 The Effect of Ride-Height Adjustments

As a first step in determining the parameters influencing the shape of the pressure map, the effect of different ride heights were investigated. Three sets of ride heights were applied to the baseline model. The ride heights, as listed in Table 3-3, were chosen to represent the dynamic operating range of the car. Diffuser stall was not induced.

| Front Ride Height	Rear Ride Height	Reason
10 mm	20 mm	Minimum Ride Height
24 mm	40 mm	Static Ride Height (control)
30 mm	60 mm	Maximum Ride Height

Table 3-3 Ride Height configuration

Note that the pitch of the model and the ground clearance was varied. The C_P contour plots of the three configurations are shown in Figure 3-9[xi].

From Figure 3-9 it can be seen that the underlying flow phenomena is relatively insensitive to variations in ride height. The basic contour and position of most isobars remain relatively constant throughout the ride-height range. As expected, the ground effect reduces as the air gap is increased. It is concluded that the basic flow pattern is not fundamentally altered by variations in ride height or pitch.

It should be stressed that although the changes that are observed in the figures are significant with respect to the aerodynamic performance of the car, this investigation was aimed at finding dramatic flow-pattern changes. In this context, smaller changes are not seen as significant.

[xi] Each colour represents the same pressure value in all the plots. The practice of colour co-ordinated pressure contours will be used throughout the remainder of the text.

FRH=10; RRH=20   FRH=20; RRH=40   FRH=30; RRH=60
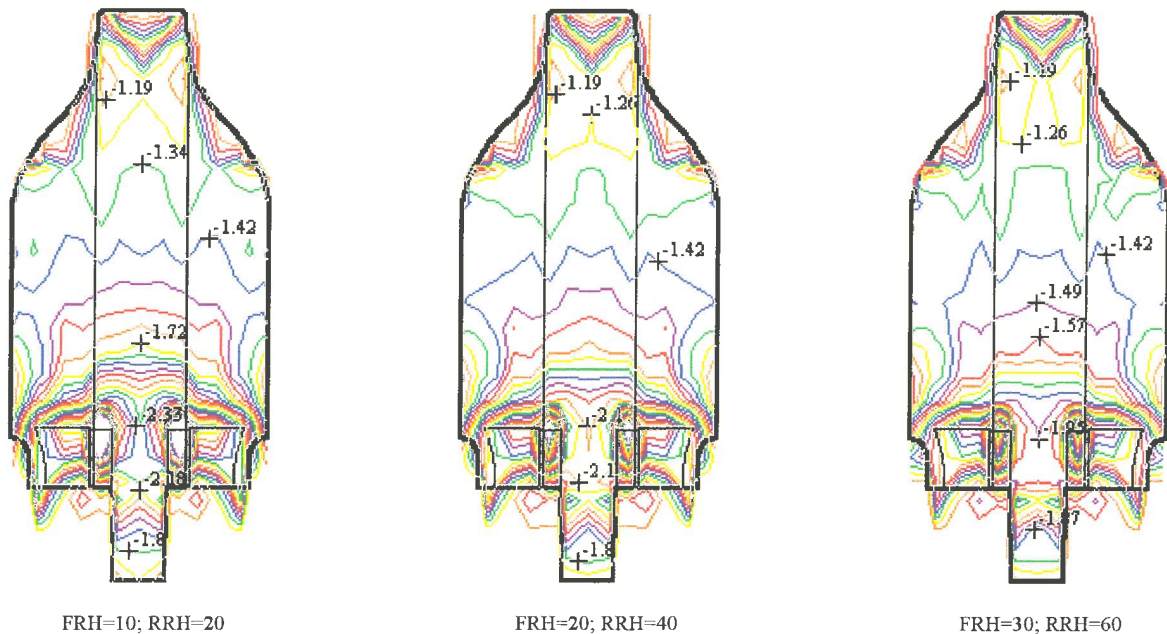
Figure 3-9 Pressure Coefficient contour maps of three Ride Heights

3.1.2.4 The Effect of Front-Flap Angle Adjustments

The front wing flaps, although fixed while driving, are the main mechanism used to balance the car aerodynamically. The flap angle of attack is therefore varied on a regular basis. As these devices deflect the air ahead of the floor, their influence was considered potentially significant and were therefore investigated next.

Two angles, one at 0° and the other at 26° were used for these tests. The two angles were the limits of the operating range of the flaps.

From Figure 3-10 it can be seen, that although changes in the contour lines are evident between the two cases, no dramatic variations are present. This suggests, that despite the influence on the shape of the pressure map, the level of downforce and the centre of pressure, that they were not the major contributors to the shape of the contours.

| 0° Front Flap Angle | 26° Front Flap Angle |
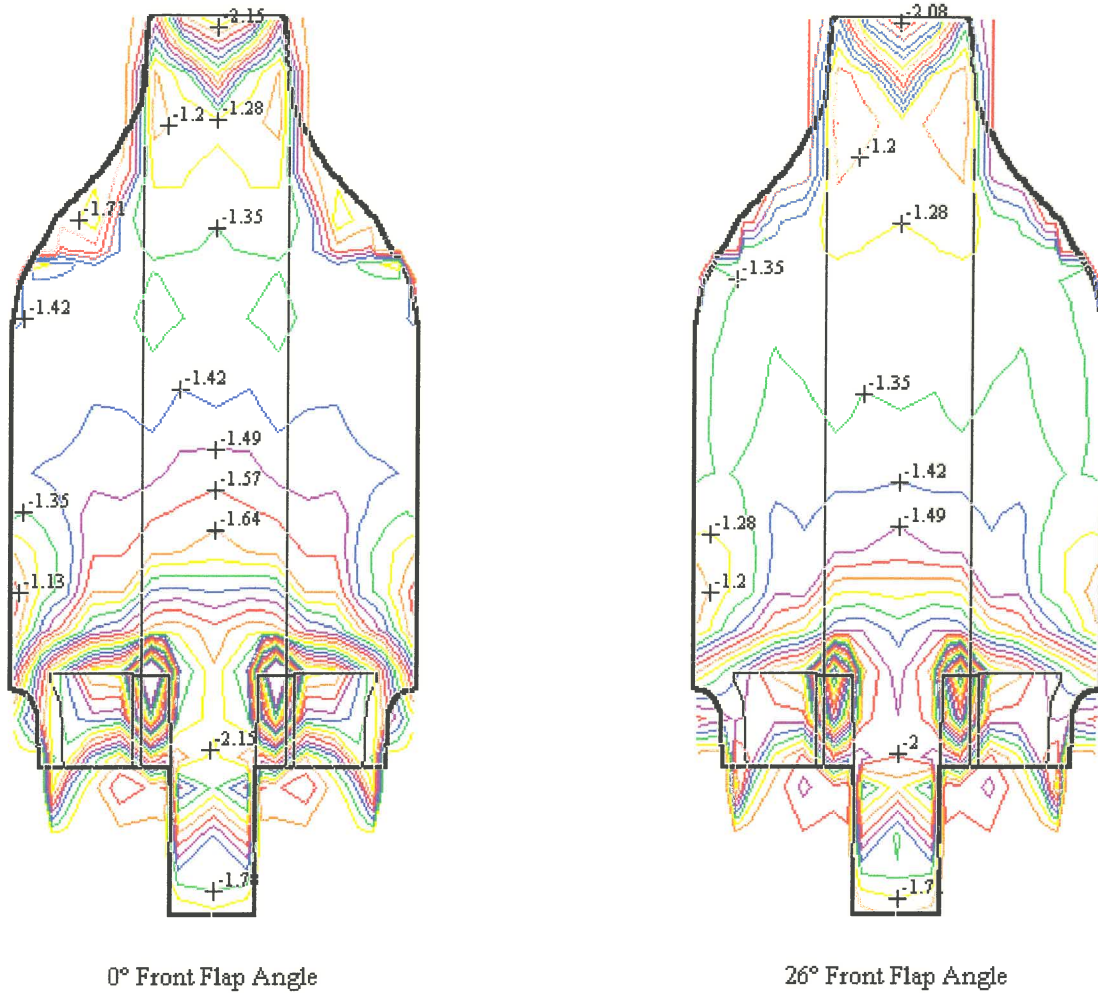
Figure 3-10 Flap Angle Comparisons

As the wheels are very prominent on Formula One cars, their effect was investigated next.

3.1.2.5 The Effect of the Wheels

The influence of the wheels were determined by removing them from the model. Figure 3-11 shows the pressure map of the floor in the absence of the wheels.
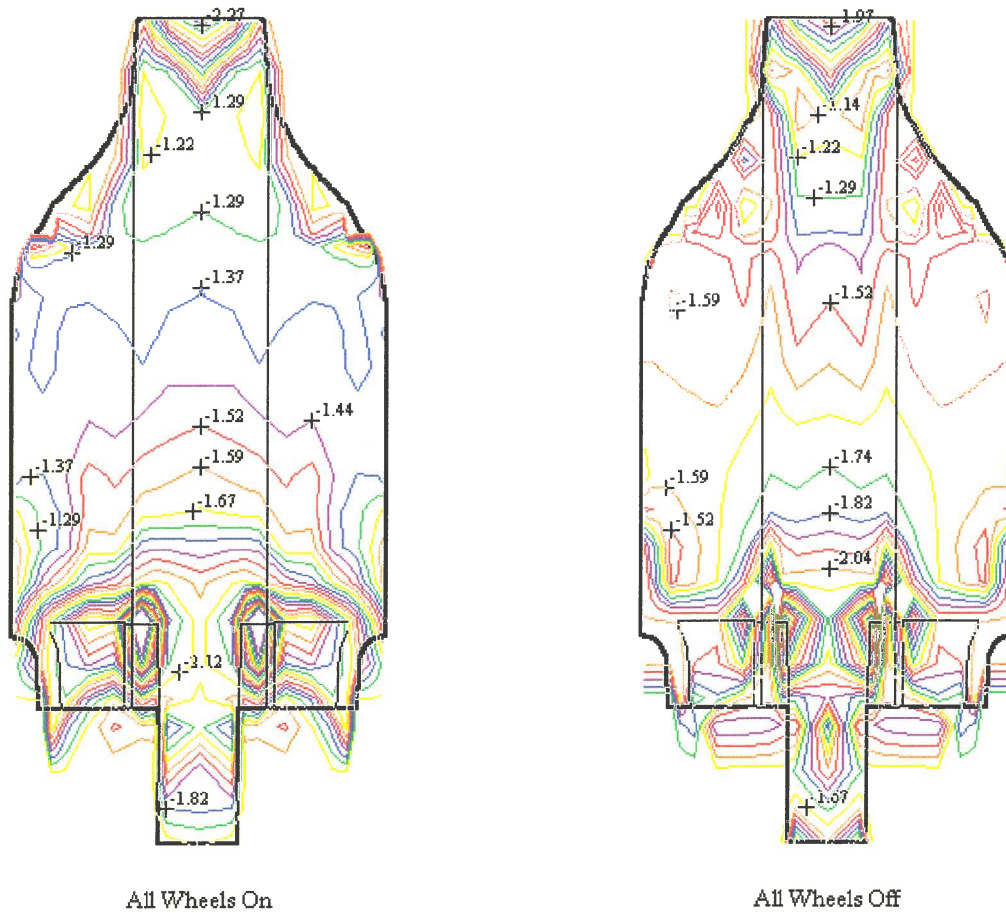
Comparing Figure 3-11 to the "wheels-on" case of Figure 3-7, it is clear that there are significant differences in the shape of the two maps. This is highlighted when the contour plots are compared as shown in Figure 3-12. The differences are visibly quantified by subtracting the wheels-off from the wheels-on case. This is plotted in Figure 3-13[xii].

[xii] The scale is adjusted so that the average of the difference lies on the ΔCp=0 plane. Surfaces above this plane therefore indicate the positive contributions of the wheels.
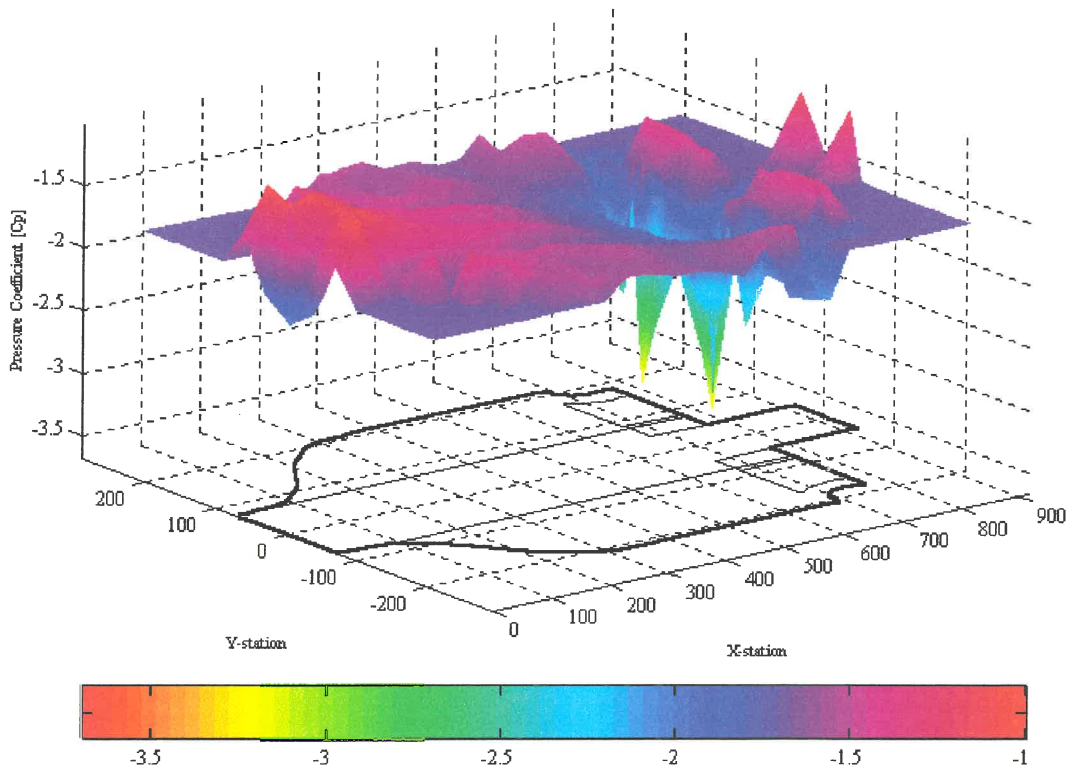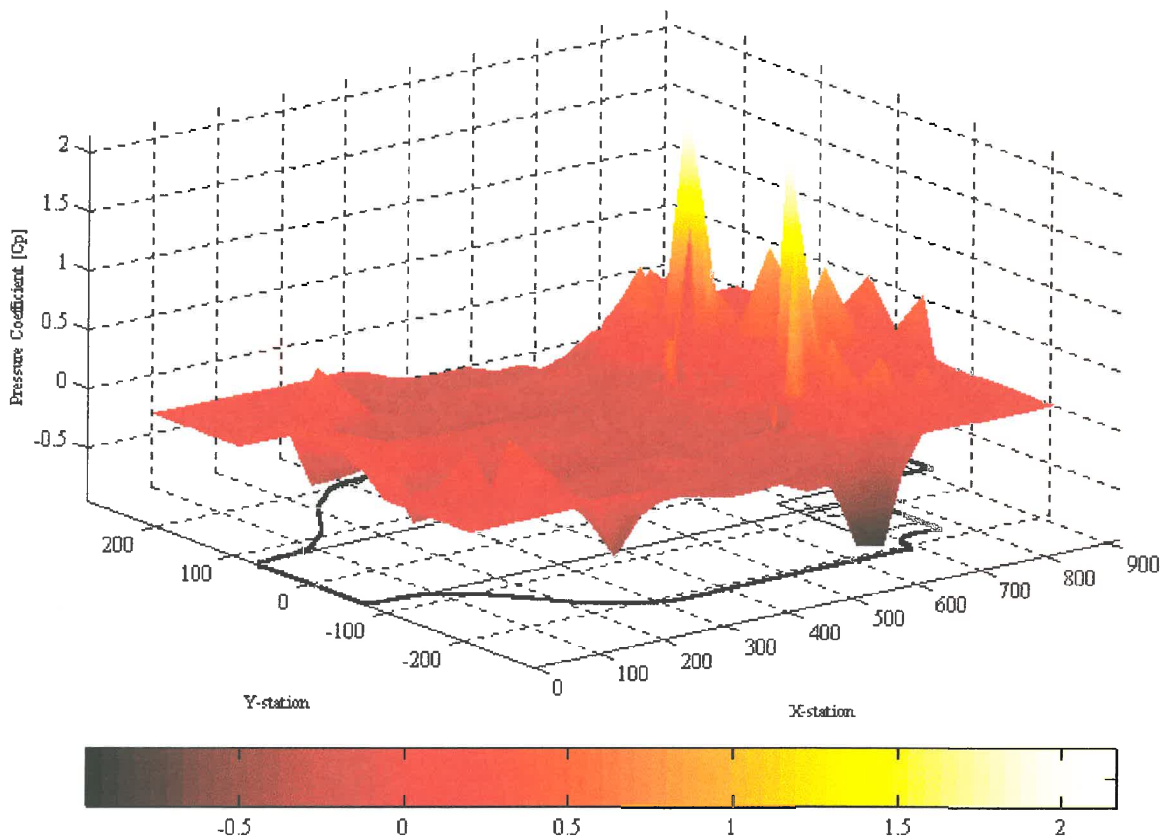
Figure 3-11 Pressure map of model floor with all 4 wheels removed

All Wheels On   All Wheels Off

Figure 3-12 Contour plot comparison of "wheel on" and "wheels off"

Figure 3-13 Differences between the "wheels on" and "wheels off" cases

By examining Figure 3-13 the changes in pressure distribution can be summarised as follows:

- Gains in downforce at the front splitter
- Losses in downforce around the circumference of the floor with two notable negative spikes. One immediately ahead of the rear wheels and the other by the air cooling intakes at the leading edge of the side-pods. A small positive spike is also visible just ahead of the cooling intakes.
- Distinct gains in the diffuser area
- A mild but extensive depression over the central floor area.

To understand the origin of these phenomena, two further tests were conducted. For the first test, the model was run without the front wheels, while the second test ran without the rear set. The results, as shown in Figure 3-14 and Figure 3-15 are plotted relative to the wheels-on case. The colour scale is identical to that of Figure 3-13.
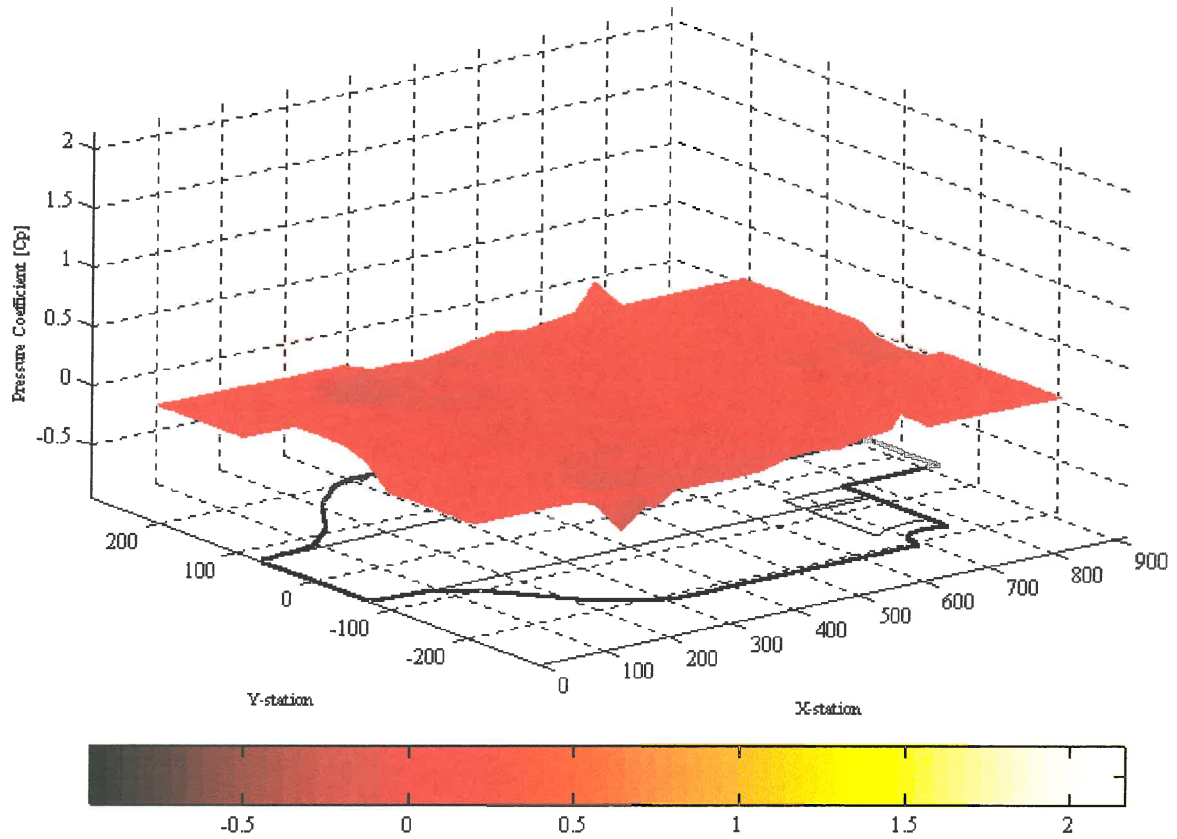
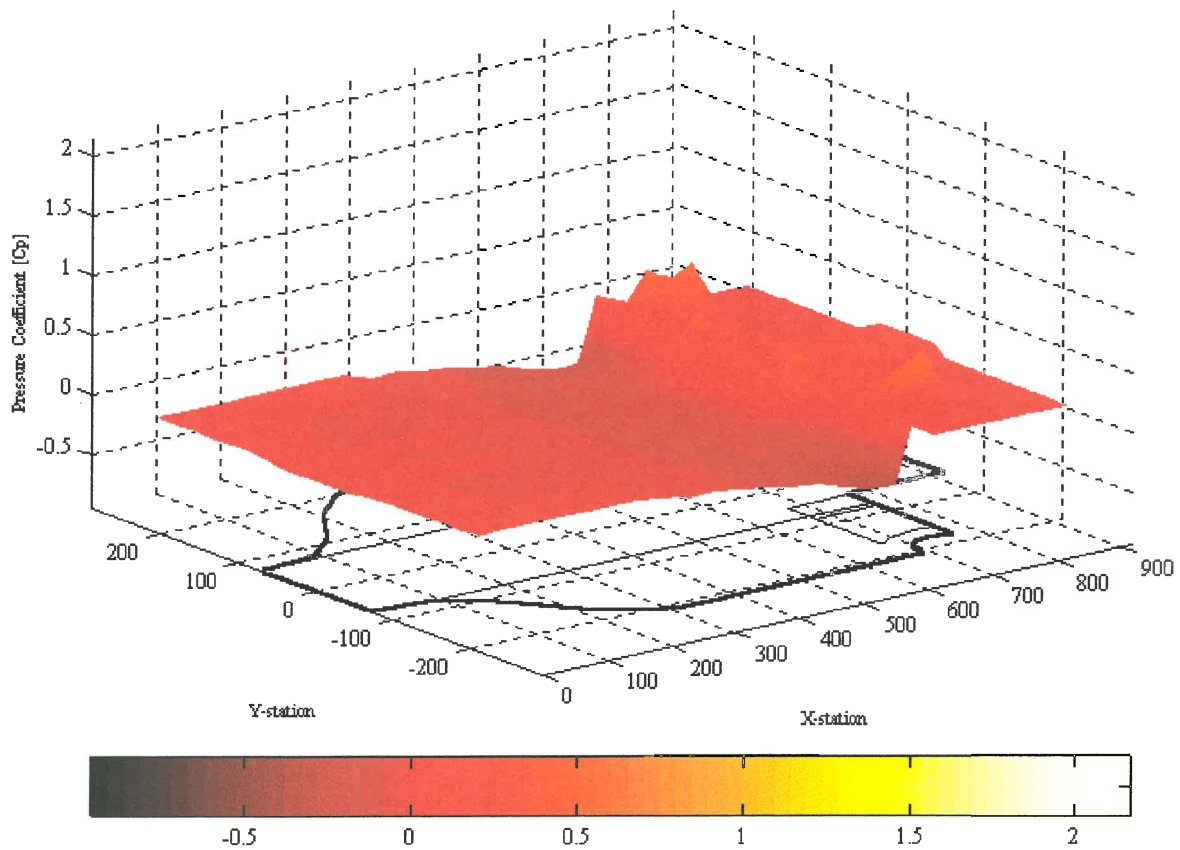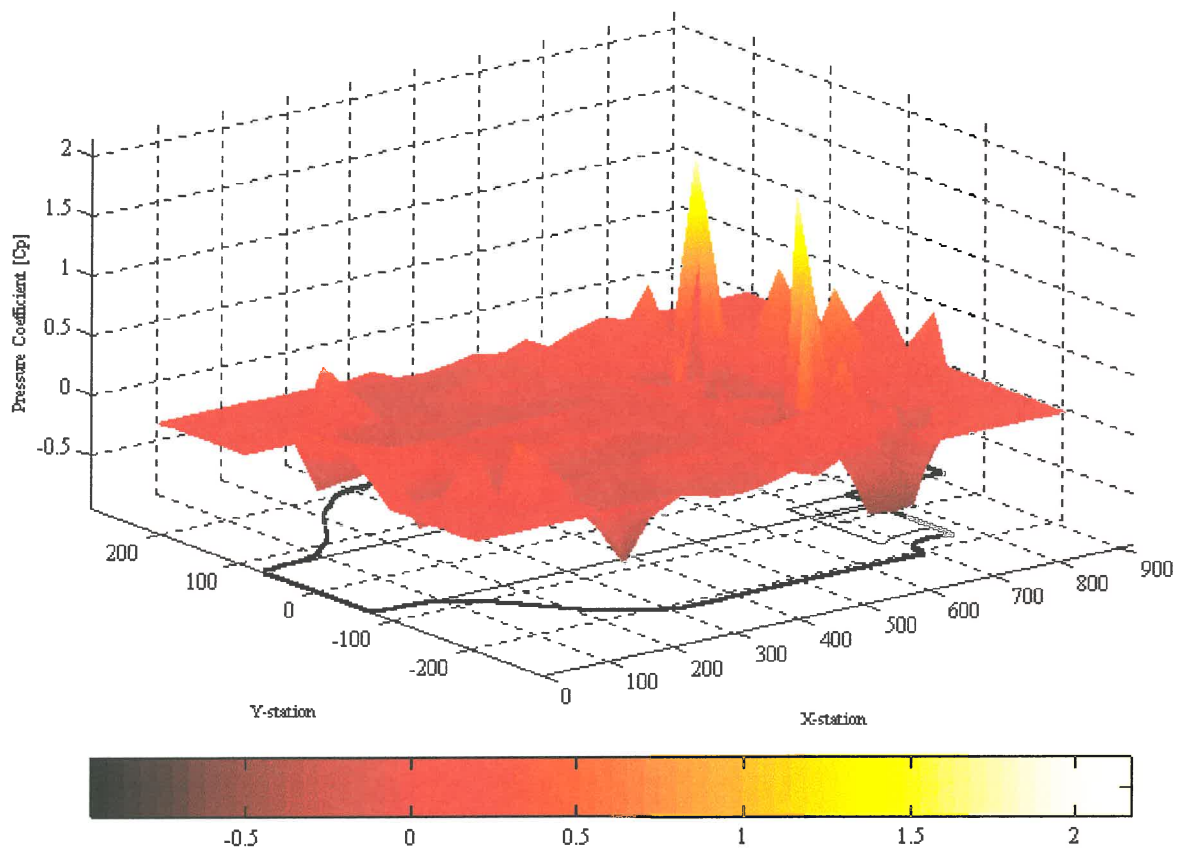**Figure 3-14 The relative effect of removing only the front wheel set**

Figure 3-15 The relative effect of removing only the rear wheel set

Comparing Figure 3-14 and Figure 3-15 to Figure 3-13, it is evident that neither show changes as pronounced as when the model had no wheels. This seems to suggest that no set is uniquely responsible for the flow-field changes. This is confirmed when the wheel-set runs are compared to the wheel-off case, as shown in Figure 3-16 and Figure 3-17. From these figures, it seems that neither of the wheel sets dominate the flow field and only one of the sets is required to induce changes of the same magnitude as indicated in Figure 3-13. Therefore, when the flow field has been established by either set, the other only causes more subtle and generally more local changes in the pressure field.

Figure 3-16 The relative effect of adding only the front wheel set

By examining the four figures presented above, it becomes possible to expand on the set of conclusions made earlier.

- The front wheels

The front wheels notably decrease the pressure at the front-splitter area. One way of explaining this, is to examine the vortices shed by the wheels[8]. The first set is shed at the contact patch of the tyres. The other is created by the interaction of the front wheels with the trailing edge of the front flap and the front-wing end-plates. These vortices were clearly visible when smoke flow visualisation was used. The symmetry of these vortices form a virtual nozzle around the centre line of the car. This creates an area for the oncoming air to accelerate through. The clockwise direction of these vortices also removes air from this channel, inducing a region of even lower pressure. The net effect is higher quality and higher velocity air under the floor. This effect can be seen to extend all the way to the rear diffuser.
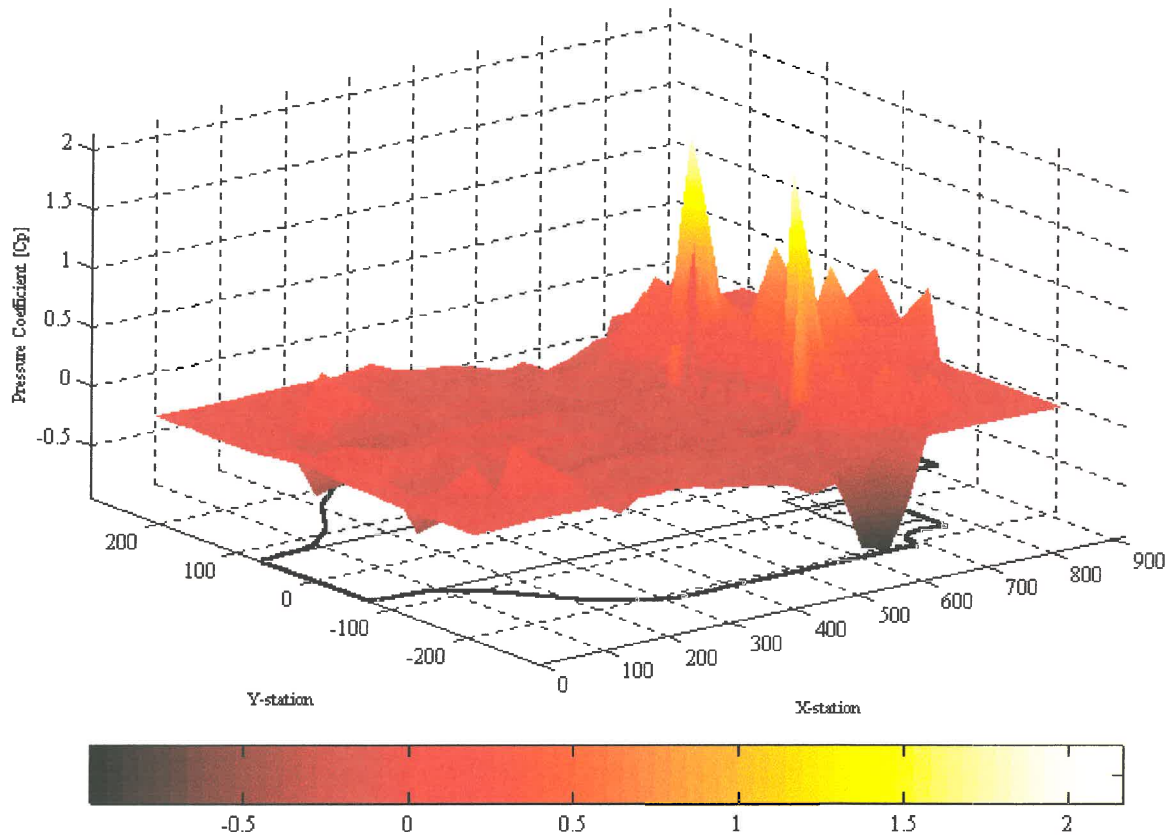
Figure 3-17 The relative effect of adding only the rear wheel set

The wake produced by the front wheels increases the amount of inflow at the edges of the floor. This effect is highlighted when the rear wheels are removed. Most notable are two spiky sets. One set at the outboard leading edge of the side-pods and the other set, at the floor-plate area of the rear diffuser. Here, the lower pressure induced by the front-wheel vortices under the floor, causes an influx of higher pressure air.

- The rear wheels

The stagnation point in front of the rear wheels induces a high pressure "bow wave". This area of higher pressure is quite extensive and in the absence of the front wheels, covers almost the entire floor area ahead of the wheels.

The vortices shed by the rear tyres on the in-board side, assist the diffuser by increasing the momentum of the flow in this area. The net effect is a decrease in the local static pressure.

To quantify these tests, the lift coefficients and the centre of pressures of the isolated floor was calculated for all four cases by surface integration as described by Equation 2-6 in section 2.2.2.2. The results are presented in Table 3-4. The COP is expressed as a percentage of the downforce available at the front wheels. For example:

If the COP was 0.7 x length of the wheelbase (WB) behind the front wheel centre line (20% behind the centre of the WB) 70% of the total downforce would be available at the rear wheels and therefore only 30% of the downforce would act on the front wheels (30%F).

From Table 3-4 it can be seen that the wheels have a negative effect on the downforce of the floor. The rear-wheel case produces the lowest level of downforce and moves the centre of pressure furthest to the rear.

Test Case	COP (%F)	Lift Coefficient (-C_L)
All wheels on	31.95	1.528
All wheels off	33.30	1.603
Only front wheels on	32.85	1.569
Only rear wheels on	31.85	1.502

Table 3-4 Lift Coefficients and balance of the wheel tests

Table 3-4 indicates that the wheels have a net negative effect on the downforce produced by the floor. It is possible to minimise their effect by using aerodynamic devices such as turning vanes or barge boards. It is potentially even feasible to use these devices to isolate the positive effects of the wheels and to improve the overall aerodynamic performance of the car.

The discussion in this section has been mainly centred around the effect of the wheels at off-centre line positions. To conclude this section, the effect of the wheels on the centre-line pressure distribution is examined by comparing the wheels-off case to the wheels-on case. The result of this comparison is shown in Figure 3-18.
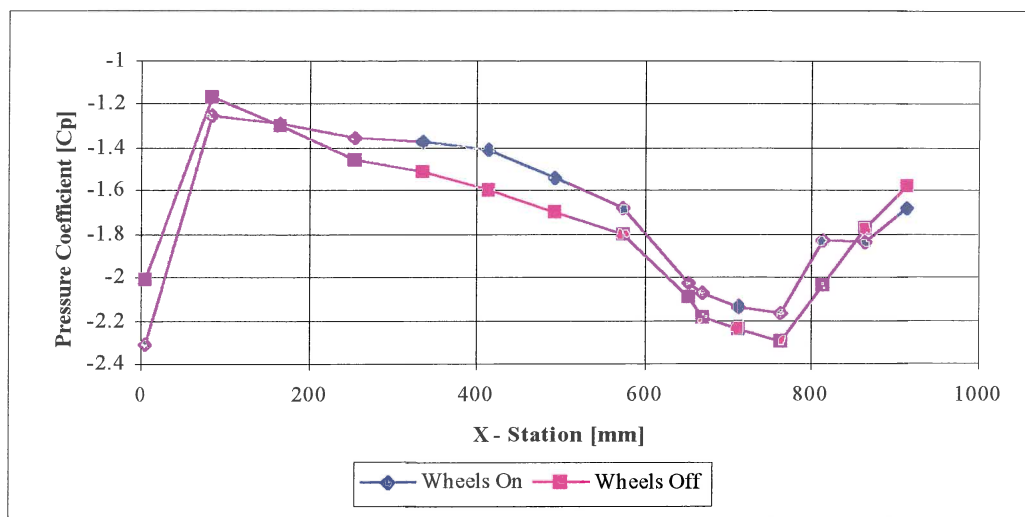
Figure 3-18 Centre-line pressure coefficient comparison: wheels-on vs. wheels-off.

From Figure 3-18 it can be seen that despite the significant influence of the wheels at positions away from the centre line, the effect of the wheels seems less influential in this area. This suggests that the fundamental shape of the centre-line pressure profile is not a function of the wheels.

3.2 Computational Investigation

Due to the close proximity of open-wheel racing cars to the ground, the interaction between the ground and the car becomes very important. This is often a major factor in the characterisation and understanding of the flow phenomena of these types of vehicles. Experimental studies therefore require rolling-road facilities to capture these phenomena. As an aid to this expensive and often very time-consuming method, CFD is being used by some

Formula One racing teams[9,10]. This is because the computer provides the designer with a virtual wind-tunnel environment where major changes can be performed with minimal cost implications. Due to the complexity and scale sizes of the flow, assumptions have to be made during the solution process. Numerical flow simulation therefore still needs to be correlated with experimental studies to verify the accuracy of the approximations and of the solution.

In this study CFD was used to investigate the air flow beneath the floor of the 30% scale model of the Forti Ford racing car. Two flow solvers were used to solve the full Reynolds-Averaged Navier-Stokes equations on a two-dimensional curvilinear grid. The first used Roe's flux-difference splitting algorithm, and the second was the SIMPLE algorithm of STAR-CD with a two-equation turbulence model. Even though a two-dimensional centre-plane geometry was simulated, the effect of the rotating wheels was incorporated using experimentally-correlated boundary conditions. This was considered feasible due to the reduced influence of the wheels on the centre-line flow pattern as shown in Figure 3-18. The experimental results discussed previously were used to verify the computational results. By independently varying front and rear-air gaps, the effect of ride-height configuration on the flow is discussed. Finally, the sensitivity of flow field on velocity variation was investigated.

3.2.1 Computational Set-up

3.2.1.1 Grid Generation

The 2D geometry was treated as an internal flow problem. The upper boundary was the 2D centre section of the car undertray as obtained from CAD data. The lower boundary was used to simulate the rolling road. The remaining two boundaries were treated as inflow and outflow boundaries.

The 2D centre-line grid was not complicated, so an efficient and inexpensive algebraic grid-generation procedure could be used. The algorithm was developed so that grid rendering was semi-automated for ride-height changes. The correct pitch, air gap and resulting grid was produced by simply defining the desired front and rear ride heights. The user also had control over the first and last spacing at the inlet and outlet boundaries as well as at the entrance to the diffuser. Vinokur[39] stretching as described in section 2.3.4.1, was used to control the spacing of the internal points. The blending function[40] as described in section 2.3.4.1 was used to ensure that grid lines were normal to the upper and lower boundaries. The user had to define the power of the blending function and the transition index for blending.

A typical grid used for the flow simulation is shown in Figure 3-19 and Figure 3-20. Note the clustering in the boundary layer and in the transition to the rear diffuser. This was to ensure proper resolution of expected high gradients in the flow.

Figure 3-19 Typical 2D-grid: full-scale front ride-height = 40 mm; full-scale rear ride-height = 40 mm
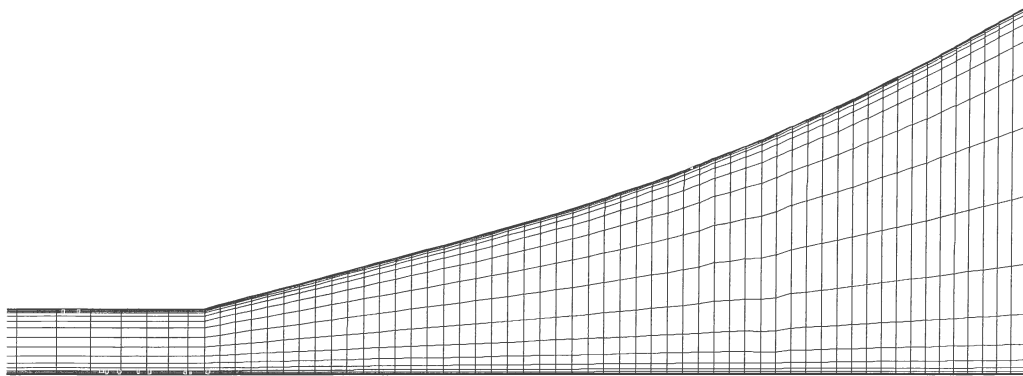
Figure 3-20 Close-up of diffuser section of grid

3.2.1.2 Flow Solvers

Two flow solvers were used during this study. These included an in-house laminar Reynolds-Averaged Navier-Stokes code, and the SIMPLE algorithm with k-ε turbulence model and wall function as implemented by STAR-CD.

The in-house code was based on Roe's flux difference splitting method as discussed in section 2.3.5.1 and in Appendix B.

3.2.1.3 Boundary Conditions

The Boundary conditions discussed in this section only apply to Roe's flux-difference splitting methods.

The inflow boundaries were specified using flow characteristics. As the flow to be solved was subsonic, only three relations were needed from the external flow at the inlet. The three relations were chosen as total pressure, total temperature and flow angle.

As the outflow conditions were subsonic and unknown away from the upper boundary, characteristic relations could only be used to solve three of the four characteristics. The final pressure characteristic, which needed to be specified from the exterior domain, was calculated using a line-iterative method as no information was available on the exterior flow field. Four different line-iterative methods as described by Wei[44], were used. The pressure on the floor at the diffuser exit was fixed using experimental data.

3.2.2 Computational Results

The flow conditions and dimensional parameters which were used are listed in Table 3-5.

All measurements were non-dimensionalised to pressure coefficients.

A typical runtime of the flow solver on an SGI Indy 133MHz workstation was 0.8msec/grid point/iteration. The maximum number of iterations used for a steady-state flow solution was 500 while a typical grid contained about 2500 points.

Parameter	Value/Description
Free stream velocity	24 - 100 m/s
Speed of rolling road	24 - 100 m/s
Temperature	295 K
Atmospheric pressure	101.325 kPa
Ratio of specific heats	1.4
Specific heat at constant volume	0.707 kJ/kgK
Viscosity	Sutherland's Law
Inflow angle	0°
Profile Length (MS)	0.92
FRH (FS)	10-40 mm
RRH (FS)	20-40 mm

Table 3-5 Flow conditions and Dimensional Parameters

3.2.3 Simulated Flow Field

Figure 3-21 and Figure 3-22 show the streamlines and relative pressure contours of two different ride-height configurations in the rear-diffuser area. Note the separation bubbles that formed against the undertray in the rear-diffuser area. These re-circulation bubbles were not observed experimentally. This can be ascribed to the interaction with the rear-wing assembly, which as described in 3.1.2.2, precludes the formation of these bubbles. The CFD rear boundary condition could not take the effect of the rear wings into account.
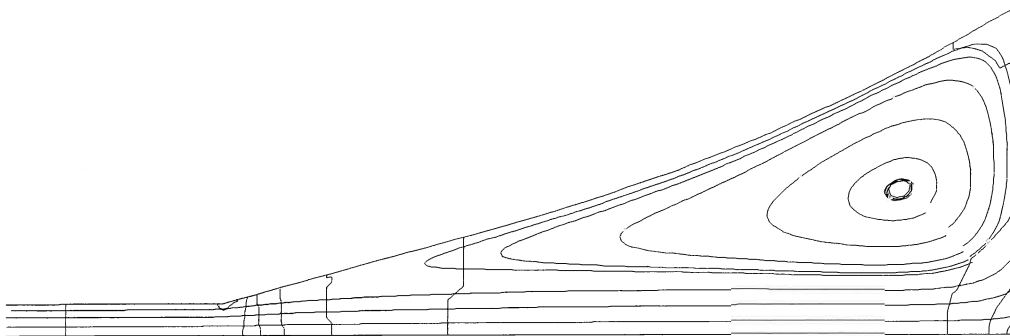
Figure 3-21 Streamlines and relative pressure contours in rear-diffuser area (FRH=10mm, RRH=20mm)

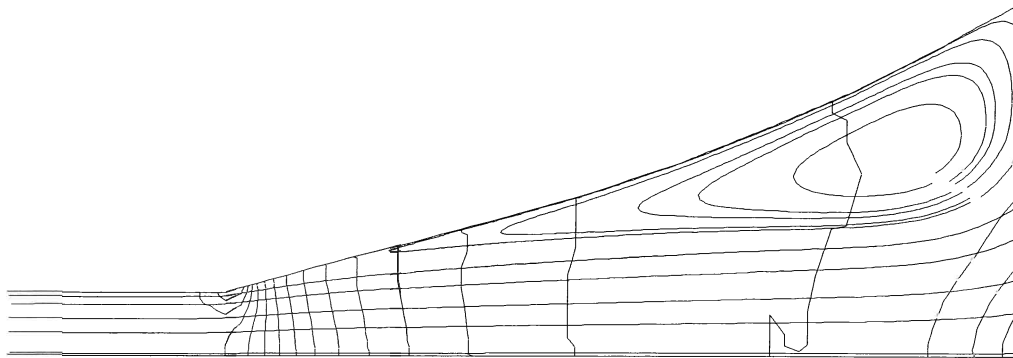**Figure 3-22 Streamlines and relative pressure contours in rear-diffuser area (FRH=40mm, RRH=40mm)**

3.2.4 Variation of Road Speed

To illustrate the sensitivity of the solution to Reynolds-Number changes, the road and free-stream speeds were varied. Figure 3-23 shows the result in the form of the normalised lift coefficient of a series of CFD simulations for the 40-40 ride-height configuration. The downforce coefficient is shown to increase with road speed as expected, but a saturation point is reached.
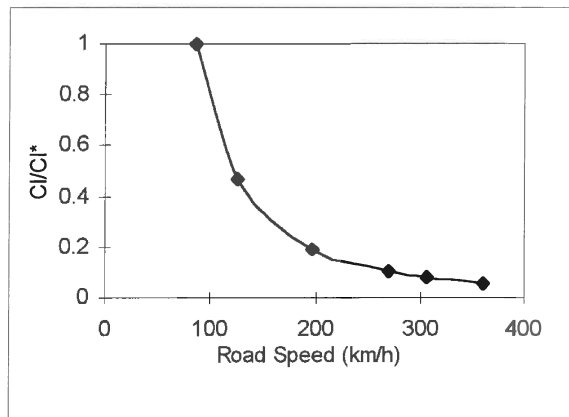
Figure 3-23 Normalised lift coefficient as a function of road speed (ride-height configuration 40-40)

3.3 Pressure Coefficient Correlation on the Centre Line

The centre-line pressure coefficients for five different computations are compared to wind-tunnel data in Figure 3-24. The data shown are for FRH = 40mm and RRH = 40mm. It can be seen that runs a and b are shifted upwards when compared to the wind-tunnel results (f). This is because the solutions generated using STAR-CD are relative to a user-specified reference pressure. After the reference pressure is adjusted to coincide with the experimental data, a better correlation is obtained (d and e). This adjustment is not necessary for the RANS in-house code (c), as pressures are calculated as absolute. The large spike obtained from this run is due to the sharp discontinuity present in the modelling of the transition from the flat undertray to the diffuser. The spike can be reduced by introducing a more even transition in the grid. The differences between runs a and b (and d and e) clearly illustrate the effect of turbulence on the solution.
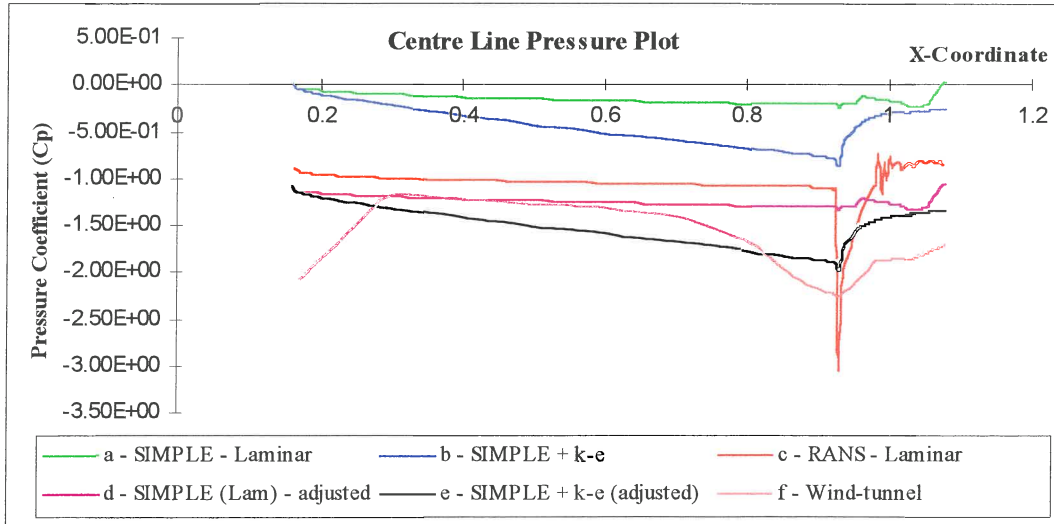
Figure 3-24 Centre-line pressure plot correlation

It is evident from the data that there are two distinct areas where the correlation between the wind tunnel and the CFD data is not accurate. These are, firstly, the area at the entrance to the under-body and, secondly, the exit- diffuser area. At the entrance area the correlation is poor because the 3D acceleration of the air due to the interaction between the front splitter plate and chassis, could not be simulated with the under-tray in isolation. At the exit, the deviation is probably caused by the omission of the rear-wing assembly.

3.4 Conclusion

In this investigation, the Parmalat Forti Ford FG01-95 racing car was used to study the flow beneath the floor of a Formula One car. The study was conducted using experimental and numerical techniques. The numerical part was, in an attempt to find more efficient development techniques, directed towards the use of centre-line geometry in predicting the flow-field trends. The experimental leg was aimed at establishing the aerodynamic influence of components external to the floor. As the numerical component used experimental data for verification, the wind-tunnel study was presented first.

The experimental study consisted of building a 30% scale model and testing it in a rolling-road wind tunnel. To capture the flow field beneath the floor, the model was fitted with 92 static-surface pressure ports.

The investigation revealed, that despite the obvious dependency of the pressure distribution on the geometry of the floor, front-flap angle and ride-height adjustments had comparatively little effect on the shape of the pressure contours. The wheels however, had a dominating influence on the shape of the pressure map. Despite the fact that the rear wheels had the biggest effect on the aerodynamic coefficients, the front wheels played an equal and independent role in setting up the underlying flow pattern beneath the car. It was however, also shown that the classic floor-pressure profile, characteristic to smooth-bottomed racing cars with front splitters and rear diffusers was still clearly visible even after the wheels had been removed.

It was suggested that the potential exists to minimise and overturn the detrimental effect of the wheels by using add-on devices such as barge boards and diffuser turning vanes.

The numerical investigation used two flow solvers to solve the full Reynolds-Averaged Navier-Stokes equations on a two-dimensional curvilinear grid. Roe's flux-difference splitting algorithm, and the commercial package, STAR-CD with a two-equation turbulence model was used. The 3D nature of the flow field was imposed on the centre-line simulation by partially using experimentally-correlated boundary conditions. It was found that although the flow phenomena beneath the isolated floor could be predicted and variations in ride height produced the correct trends, the absence of the rest of the vehicle lead to premature separation in the diffuser. The effect of the front splitter could also not be predicted. Reynolds-Number independence with respect to the lift coefficient was also demonstrated.

To investigate the attainable correlation between the numerical and experimental flow around a racing car, a new study was launched where a less complicated experimental model was used. This is the topic of the next chapter.

4. THE FLOW AROUND A GENERIC BMW TOURING CAR

The aerodynamic investigation of the Parmalat Forti Ford F1 racing car, as presented in Chapter 3, highlighted the difficulties in correlating the numerical centre-line simulation of the isolated floor to the experimental 3D case. The effects of components such as the rear wing and front splitter could not be imposed on the numerical model by simply using experimentally-measured boundary conditions. The conclusion was reached that correlation could potentially be improved by including more detail in the simulation. To address this problem effectively on a 2D basis, the complete centre-line of the car had to be simulated.

The computational costs involved in simulating the complicated F1 profile made this approach very expensive. A less complicated model was therefore chosen. A generic model of a $1/12^{th}$ scale closed-wheel BMW Touring Car was used to investigate the accuracy of centre-line simulations. The smaller scale, as compared to the F1 study, offered the following advantages:
- Lower model-manufacturing costs.
- A smaller and less complicated numerical grid.
- Increased numerical efficiency.
- Reduced tunnel size and related operating costs.

Although the smaller scale resulted in a loss of detail, the scale was still big enough to ensure a representative racing car. Furthermore, full-scale correlation was not the intention of this study and so the loss in detail would not affect the correlation exercise.

A closed-wheel vehicle was chosen to limit the effect and influence of the wheels. The generic nature of the model ensured that a smoothed-bottomed floor could be used and guaranteed the presence of components such as the front splitter and rear diffuser. The choice of motor manufacturer was based on the availability of moulds in the form of commercial scale-model electric-toy racing cars. The body shells of these "toys" offered sufficient detail and eliminated the need for the manufacturing of expensive and complicated moulds.

This investigation, similar to the one presented in Chapter 3, also consisted of an experimental and a numerical study. In this case however, the emphasis was placed on the numerical simulations. The experimental side was mainly used to determine a baseline set of results for use in the computational investigation.

The experimental data was obtained by constructing a scale model of the BMW, fitting it with static-surface pressure taps and testing the model in a wind tunnel. After repeatability and Reynolds-Number independence are demonstrated, the discussion of the experimental results is introduced by examining the similarities between the under-body flow of the BMW and the Parmalat Forti Ford. The baseline experimental results for use in the numerical part is then presented. Included in this section, is a discussion on the interaction between a rear-mounted aerodynamic device and the under-body flow of the BMW. These results are used to explain the underlying phenomena responsible for rear-wing downforce on a sedan-based racing car.

The computational flow solver and grid-rendering software of STAR-CD was used in the numerical investigation. After a description of the grid, the effect of three different turbulence models is investigated. From this study it is seen that although similarities between the experimental and numerical cases exist in certain areas, the correlation under the floor is still

poor. It is concluded that the most likely cause of these discrepancies lies within the computational methodology. At this point it was decided to terminate this study with a proposed outline of work which should be included in a future investigation to improve the numerical accuracy. This discussion includes further simulations and related conclusions. The effects of mesh density and the dependency on the choice of turbulence model and related parameters are covered.

4.1 Experimental Investigation

4.1.1 Experimental Set-up

The closed-return LSWT at the University of Pretoria, South Africa was used for the experimental tests. The wind tunnel had a 0.9x1.1x2m closed test section with a stationary floor. The six-component tail-sting strain-gauge force balance of the tunnel was not used.

To avoid tunnel boundary-layer problems a raised platform was installed. The platform had a knife-edge profile at the leading edge and was approximately 150 mm above the tunnel floor. The platform was inclined at a slight negative angle to limit the development of the platform boundary layer[14] as described in section 2.2.1.2.

The effective tunnel blockage was calculated to be approximately 3% for the 1/12th scale model of the Generic BMW German Touring car. Blockage calculations were referenced to the raised platform.

The tunnel tests were performed at velocities ranging from 40 to 60 m/s. Using the length of the model as the characteristic length, the Reynolds Numbers were in the range of $1x10^6$ to $1.7x10^6$. This was above the critical Reynolds Number as discussed in section 2.2.3.1.

The nose of the model was mounted 360 mm from the leading edge of the platform and the rear end of the vehicle was 675 mm in front of the trailing edge of the platform. The trailing-edge distance was chosen to exceed Garry's[15] criteria for drag errors as described in section 2.2.1.2.

The mould used to construct the model was the body shell of a 1/12th scale electric racing car model. The upper shell was constructed using glass fibre. The model had a smooth wooden floor with closed wheel arches. The engine cavity was closed off by extending the floor from the leading edge to the trailing edge of the model. The scale wheels, which were taken from the electric racing car, were mounted onto the test platform ensuring, as required by Cogotti[46], zero air gap between the platform and the wheels. The wheels were fixed and were therefore not free to rotate.

The upper and lower centre-line surface of the model was fitted with 38 centre-line pressure ports as shown in Figure 4-1. All pressures were corrected using the continuity-based blockage-correction factor as proposed by Sykes[47] and discussed in section 2.2.3.2.
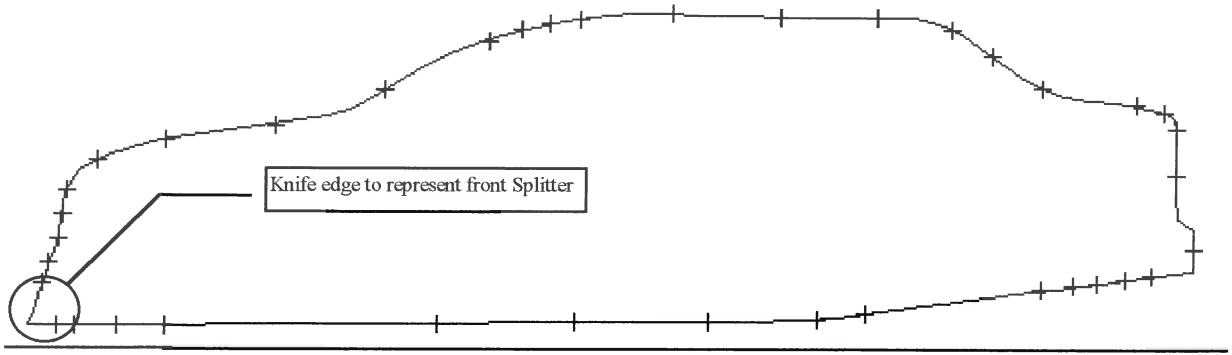
Figure 4-1 Centre line profile showing the positions of the pressure tapping

From Figure 4-1 it can be seen that the front splitter is represented by a knife edge. The inclusion of a rear diffuser is also clearly visible.

The pressure taps were connected to a Scanivalve and data-acquisition system. The valve was mounted inside the model to limit the cabling to and from the model. Cables leaving the model were taken out behind one of the rear wheels. The schematic representation of the model as mounted in the wind tunnel is shown in Figure 4-2.
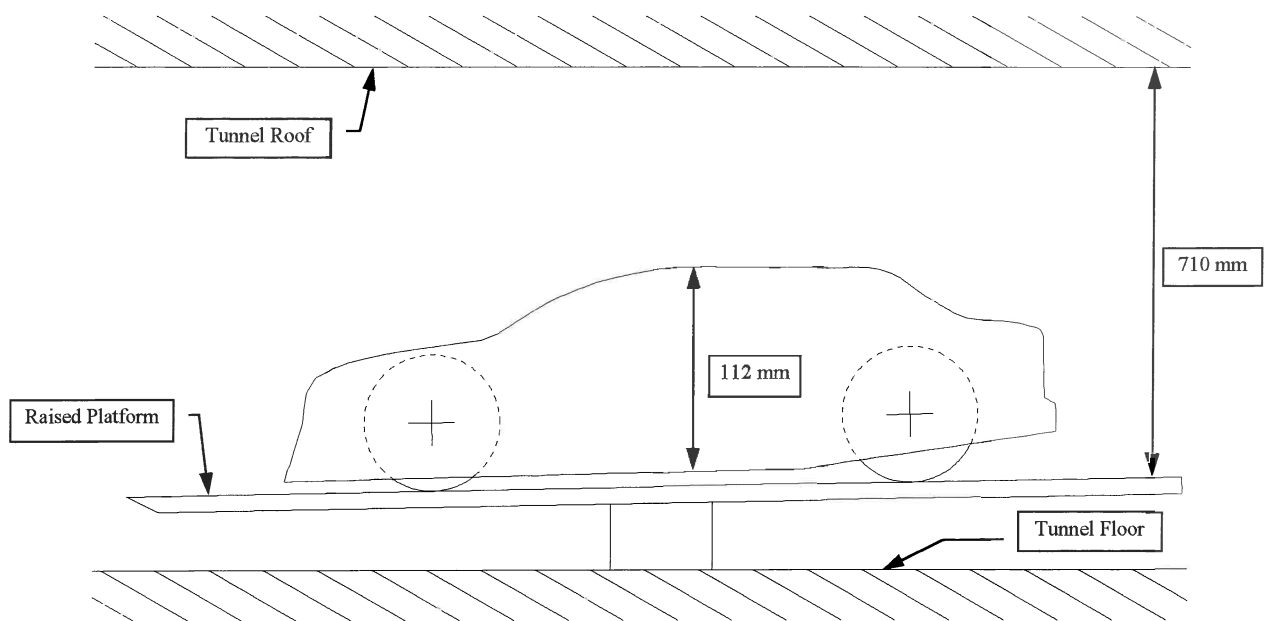
Figure 4-2 Schematic layout of the BMW model as mounted in the wind tunnel

4.1.2 Experimental Results

4.1.2.1 Repeatability

The repeatability of two identical runs, made on different days is summarised in Table 4-1. All the pressure taps were used for the calculations.

Variable calculated	Result
Mean Pressure coefficient of Run 1 (C_P)	-0.1241
Mean Pressure coefficient of Run 2 (C_P)	-0.1252
Mean difference between Runs	0.0020
Mean difference expressed as a percentage (%)	1.3

Table 4-1 Results of repeatability calculations

Differences of less than 1.3% will be interpreted as repeatability errors and not as aerodynamic changes.
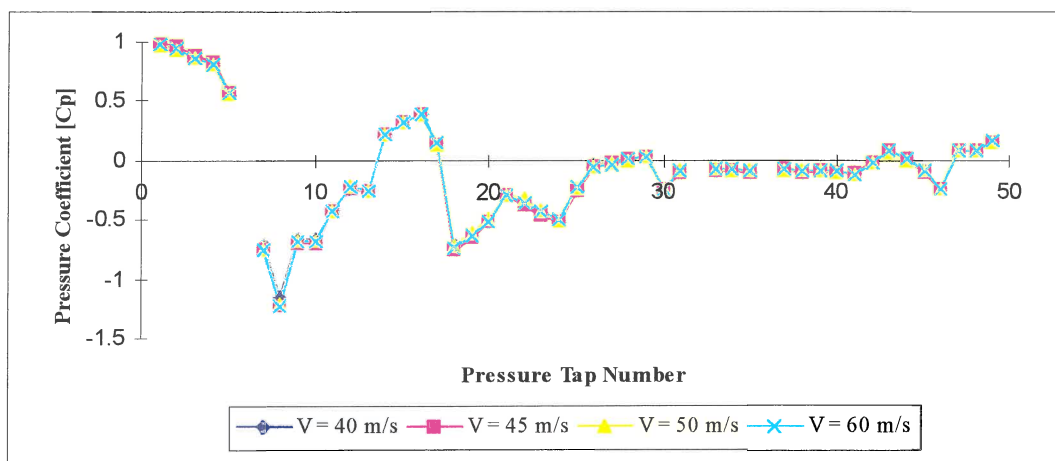
4.1.2.2 Reynolds-Number Sensitivity

The success of CFD models in simulating the flow field around a car is very sensitive to the ability to predict the point or line of flow separation accurately. In a similar way, the aerodynamic coefficients and related pressures of experimental tests are also subject to separation and to the levels of turbulence in the boundary layer and in regions of separated flow. As explained in section 2.2.3.1, turbulence and separation can be represented at scale by ensuring Reynolds-Number independence. To ensure this, pressure readings were measured on the scale model at Reynolds Numbers ranging from 1.15×10^6 to 1.73×10^6. The results, as presented in Figure 4-3, were reduced to velocity comparisons as all the other parameters defining the Reynolds Numbers remained fixed.

Figure 4-3 - Reynolds-Number Sensitivity

From Figure 4-3 it can be seen that there is almost no variation in the magnitude of the pressure coefficients. A test velocity of 40 m/s was therefore adequate to ensure Reynolds-Number independence. As these results are in good agreement with the findings of Barnard[16] who suggested a Reynolds Number in excess of 9.6×10^5, all experimental tests and numerical simulations were performed at this speed.

4.1.2.3 The Characteristic Floor Pressures

To establish continuity with the F1 case study, the BMW floor-pressure coefficients were compared to the Forti coefficients. The results are displayed in Figure 4-4. The F1 data is identical to the values used in Figure 3-6.

As seen from Figure 4-4, the characteristic pressure drop at the front splitter and rear diffuser is also visible for the BMW. The pressure drop induced by the rear diffuser of the BMW is however, less pronounced than that of the Forti. This is to be expected as F1 cars are designed

to be aerodynamically superior, they run at lower FS ride heights, they have more complicated diffusers which run at higher angles and they carry a multitude of efficient wings. The higher aerodynamic forces generated by F1 cars are clearly indicated by the significantly lower pressure coefficients.
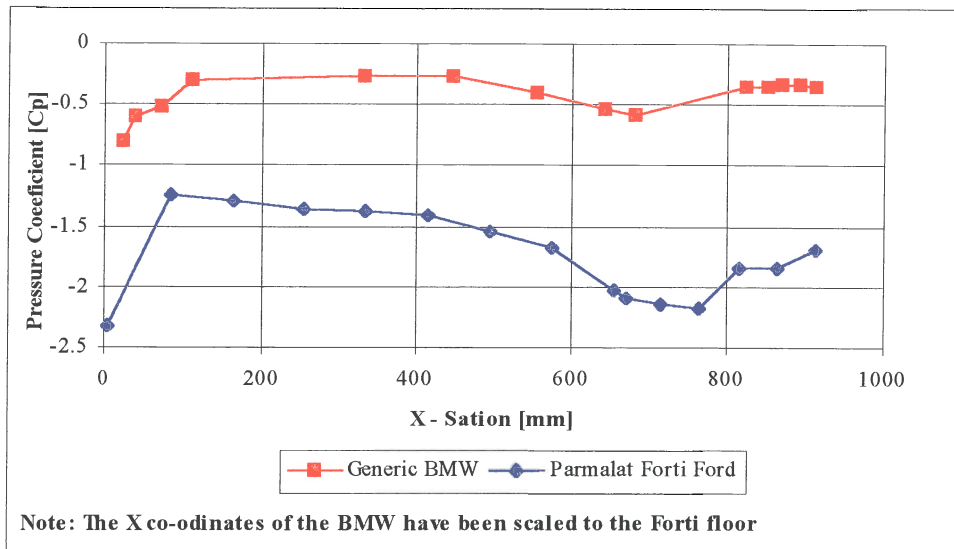
Figure 4-4 Under-body pressures of the Generic BMW and the Parmalat Forti Ford

Continuity with the F1 study has therefore been established.

4.1.2.4 The Centre-Line Pressure Distribution

The main aim of the experimental investigation was to provide a set of base-line results to which the CFD simulations could be compared. The results of these measurements are presented in Figure 4-5 to Figure 4-8 in the form of non-dimensional pressure coefficients. Each figure was chosen to represent a distinct physical region of the vehicle. These were defined to facilitate viewing and discussion. The regions were defined as:

- The nose area - Figure 4-5
- The upper surface area - Figure 4-6
- The rear area - Figure 4-7
- The floor area - Figure 4-8

X=0 and Z=0 are taken to be at the bottom leading edge of the car. All co-ordinates are given in model scale. These conventions are followed throughout the remainder of this chapter.

The lack of numerical correlation in the F1 case study, was amongst other reasons, attributed to the influential effect of the rear-wing assembly. The importance of this interaction was illustrated by placing a 20 mm vertical spoiler or Gurney flap (GF) on the small-scale BMW model. The GF spanned the entire trailing edge of the boot-lid. The results of this set-up were also plotted in Figure 4-5 to Figure 4-8.

It should be noted that the measurements presented in the four figures were made at discrete locations and the data points have simply been connected to establish trends and facilitate interpretation.
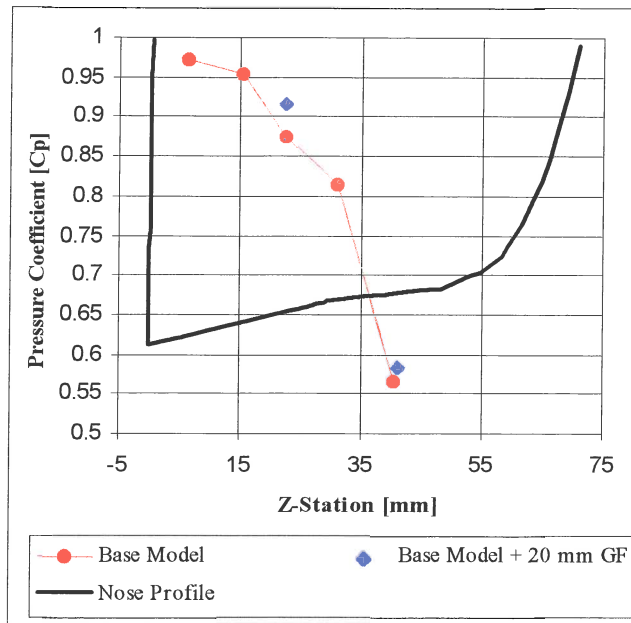
Figure 4-5 Pressure distribution on the centre line of the nose of the car[xiii]
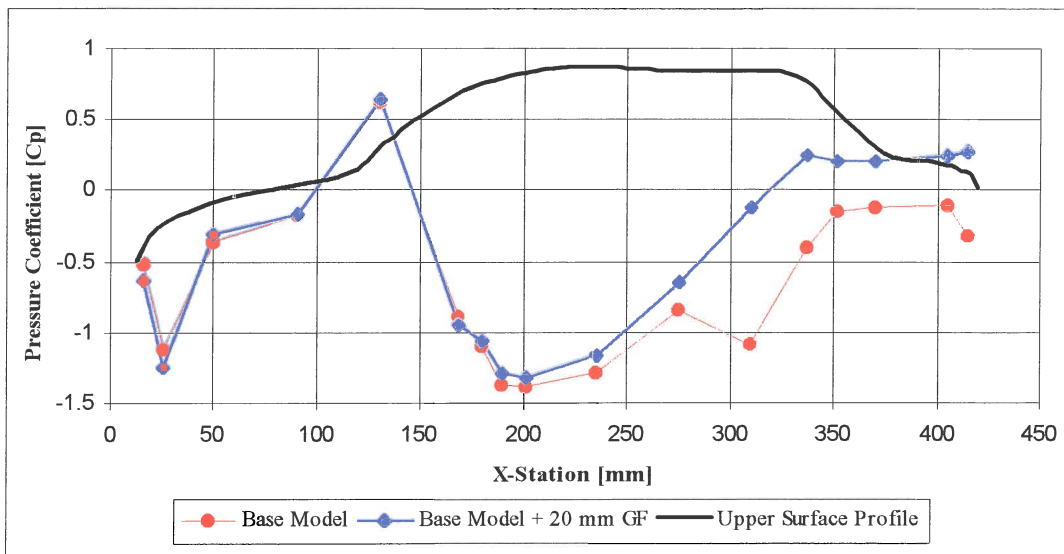
Figure 4-6 Pressure distribution for two tunnel runs on the centre line of the top of the car

---

[xiii] The "Base model + 20 mm GF" case only show the results of two pressure measurements. Three of the five ports became blocked during this run and were therefore not included.
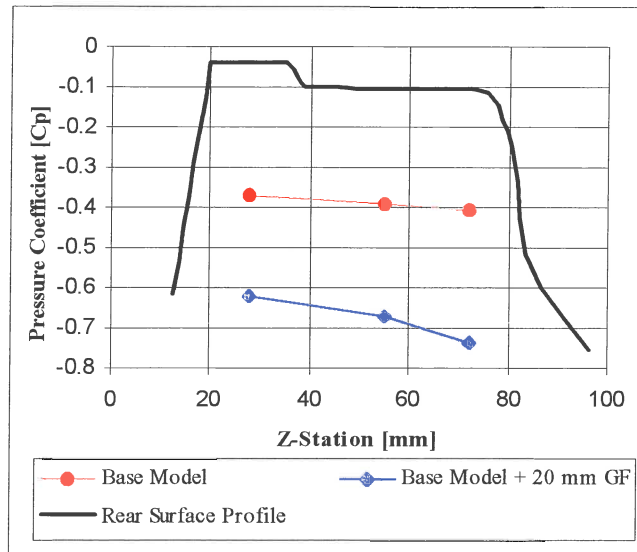
Figure 4-7 Pressure distribution for two tunnel runs on the centre line at the rear of the car
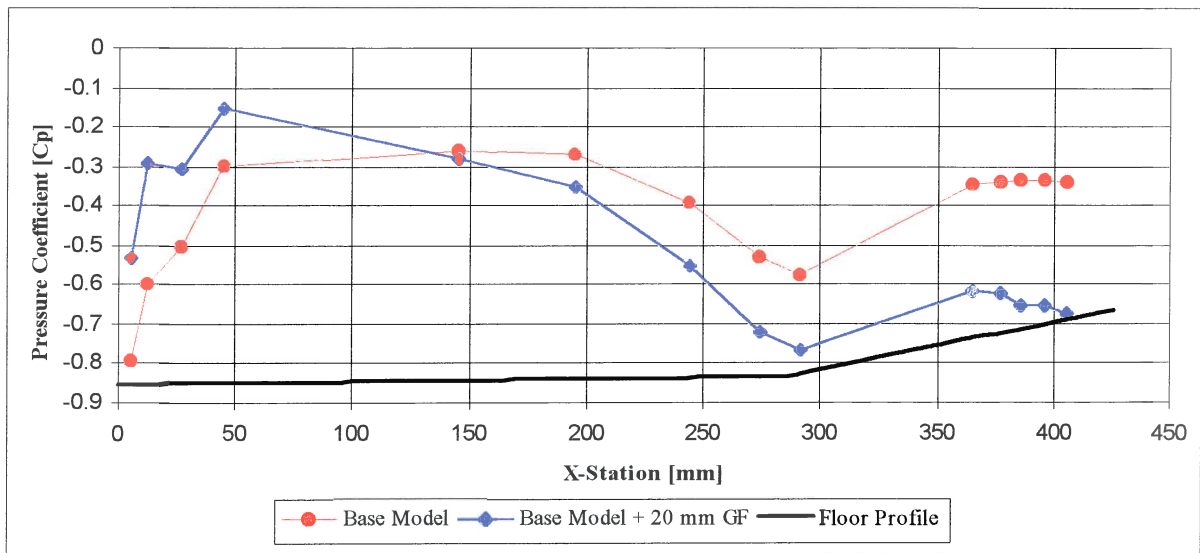
Figure 4-8 Pressure distribution for two tunnel runs on the centre line under the floor of the car

It is evident from the figures that the GF has a marked effect on the pressure distribution over most of the car. The pumping effect of this "wing" as described in section 3.1.2.2, can clearly be seen in Figure 4-8. It can be seen that for the GF case, the pressure under most of the floor was significantly lower than for the baseline case.

Examination of Figure 4-6 and Figure 4-8 also reveals the mechanism responsible for producing rear downforce on sedan-based racing cars fitted with boot spoilers or wings. In addition to the reduction in the under-floor pressure, the rear "wing" also increases the pressure over most of the aft section of the upper surface of the vehicle. The net effect is an increase in the pressure differential between the two surfaces. Rear downforce is therefore generated. Unfortunately, in this case, the increase in rear downforce is offset by a decrease in the front downforce. This is because the rear spoiler increases the pressure under the nose but the pressure on the upper surface remains almost unchanged.

The spoiler also increases the drag of the car. This effect, although not calculated, is evident from the lower base drag in Figure 4-7 and the comparatively insignificant change to the pressures at the front of the car as shown in Figure 4-4.

it can further be seen that although the GF changes the distribution of the pressures under the floor, the characteristic centre-line pressure profile, as discussed in section 3.1.2.2, remains unaltered.

4.2 Computational Investigation

The aim of this investigation was to extend the numerical study presented in section 3.2 by investigating the accuracy with which the centre line of a closed-wheel racing car could be approximated by a two-dimensional computational simulation. These results are presented in this section.

4.2.1 Computational Set-up

The computational domain used to solve the flow around the centre-line profile of the experimental $1/12^{th}$ scale BMW was generated using a CAD system and PRO-STAR, the structured grid rendering pre-processor of STAR-CD. The grid was generated using a number of grid blocks which were matched to ensure connectivity. This approach was required to ensure an accurate centre-line profile and also to facilitate grid clustering in regions where high flow gradients were expected. To ensure a self-contained solution the grid was extended by three car lengths to the front, five car lengths to the rear and four car heights above the vehicle. The resulting grid as shown in Figure 4-9 contained 24240 cells.

Figure 4-9 Centre-line grid for the $1/12^{th}$ scale Generic BMW

The spacing between grid-cell centroids on the surface of the vehicle is described in Table 4-2.

	Average Spacing [mm]	Minimum Spacing [mm]	Maximum Spacing [mm]
The Nose	4.83	2.99	5.46
The Upper Surface	7.82	1.16	10.37
The Rear	2.93	0.811	3.84
The Floor	8.52	8.23	8.67

Table 4-2 Grid spacing on the surface of the BMW

The SIMPLE algorithm as implemented by STAR-CD was used in this investigation. This method was considered more suitable than the PISO and SIMPISO STAR algorithms as the flow was assumed to be steady and excessive grid skewness could be avoided during meshing.

The boundary and flow conditions which were used to close off the system of numerical equations are summarised in Table 4-3 and Table 4-4.

Boundary Description	Boundary Position	STAR Boundary Condition
Inlet	Far field - 3 car lengths in front	Free stream horizontal velocity
Outlet	Far field - 5 car lengths behind	Percentage mass Flow
Solid 1	Vehicle Body	Solid
Solid 2	Road	Solid
Reflection	Far field - 4 car heights above	Reflection
Centre Line	Either side of "1 cell thick" grid	2D Symmetry

Table 4-3 Boundary conditions

Flow Condition or Dimensional Parameter	Specification
Free-stream velocity	120-150 km/h
Density of air (constant)	1.205 kg/m^3
Temperature of the air	295 K
Atmospheric pressure	101.325 kPa
Ratio of specific heats	1.4
Specific heat at constant volume	0.707 kJ/kgK
Viscosity	Sutherlands Law
Turbulence mixing length	0.01
Turbulence intensity	0.1

Table 4-4 Flow conditions and dimensional parameters

4.2.2 Computational Results

The regions of separated flow and related turbulence around a racing car suggests that turbulence models would have a significant role to play in achieving correlation. The effect of turbulence models was therefore investigated first to obtain an indication of potential correlation.

4.2.2.1 The Effect of Turbulence Models

The three standard STAR-CD turbulence models for high Reynolds-Number flows were used to investigate the effect of turbulence on the solution. For comparative reasons a laminar solution (no turbulence model) was also generated. The numerical solutions that are discussed in this section were categorised according to the turbulence model that was employed. The four solutions are described as:

- The laminar flow case (No Turb)
- The standard k-ε turbulence model flow case (KE)
- The k-ε RNG turbulence model flow case (KE-RNG)
- The k-ε turbulence model of Chen flow case (KE-Chen)

The bracketed abbreviations are used to describe the results in the figures which follow.

The numerical solutions were all compared to the experimentally measured data as discussed in section 4.1.2.3.

The results of the four turbulence solutions are presented in Figure 4-10 to Figure 4-13 in similar fashion to the figures of section 4.1.2.4.

From Figure 4-10 it can be seen that there is agreement between the experimental data and the laminar flow case in the upper region of the front nose area of the car. The deviations near the ground are caused by the incorrect prediction of the magnitude and position of the stagnation point. The higher physical position of the numerically-calculated stagnation point implies an incorrect split of the flow around the vehicle. This has implications downstream as the volume of air available to perform work above and below the car will be incorrect. All three turbulence models suffered with this inaccuracy. Of the three turbulence models, the standard k-ε model is seen to perform the worst. This model seems to predict a relatively large stagnation area. The RNG and Chen models, although conservative, approach the experimental pressure contour with higher accuracy.
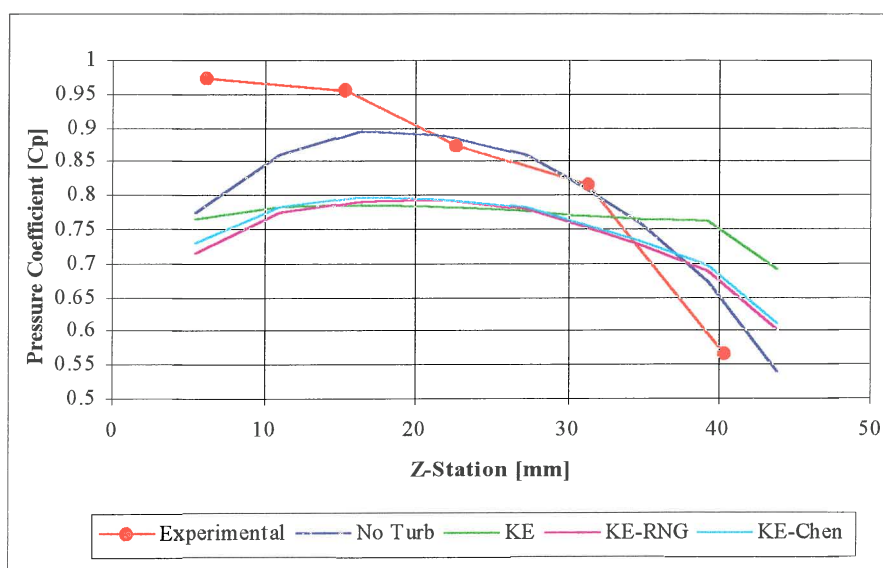
Figure 4-10 - BMW Nose: CFD Turbulence model comparisons

The stagnation point indicated by pressure coefficients close to unity is characterised by areas of low Reynolds-Number flows. This possibly accounts for the poor performance of the High Reynolds-Number turbulence models in this area. The additional terms in the dissipation and related closure terms of the RNG and Chen models as discussed in section 2.3.3.1 seems to improve the performance of these models compared to the standard k-ε model.

On the upper surface of the model, as shown in Figure 4-11, the four numerical models are in good agreement with each other until the leading edge of the roof. The overriding positive pressure gradient is the most likely cause for the agreement. Absolute correlation to the experimental case is however, less positive. The pressure coefficients are under-estimated by more than 0.5 in some cases. Despite this, the correct pressure trends, such as the accelerated flow over the leading edge of the bonnet, the slope change at the bottom of the windscreen and the acceleration over the windscreen, are still predicted by all the models.

From the roof leading-edge rearwards, overall correlation is less favourable. Although the laminar model follows the experimental data the closest, the pressure drop induced by the

negative gradient at the rear window is underestimated by this model. The turbulence models, as expected, capture the change in gradient with higher accuracy.
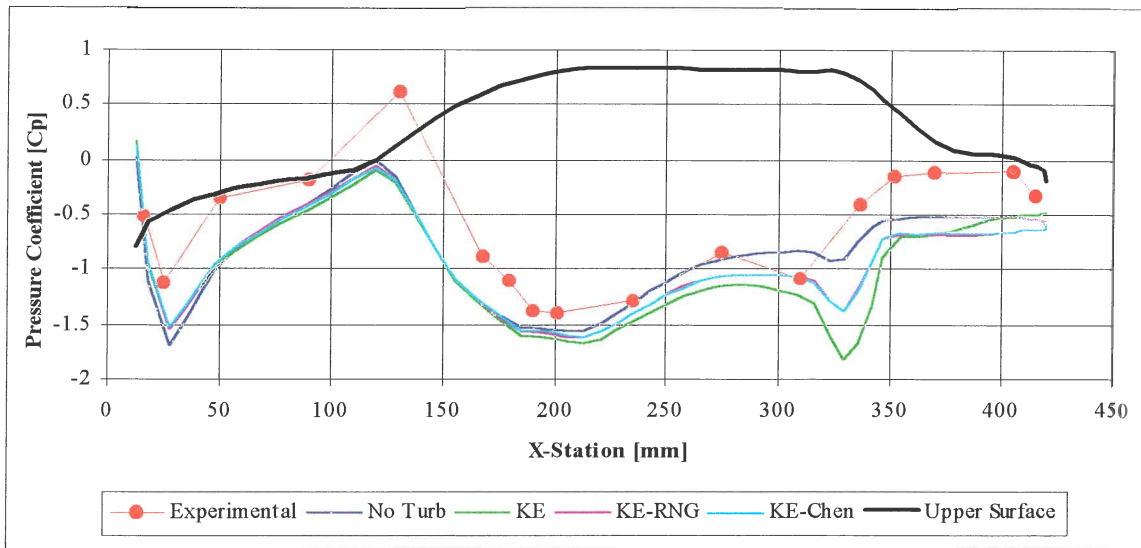
Figure 4-11 BMW Upper surface: CFD Turbulence model comparisons

The standard k-ε model overestimates the pressure recovery on the boot. Here, the RNG and Chen models perform better. These two models seem to be in very close agreement over the entire upper surface of the car.

Generally speaking it can be seen that the turbulence-model pressures are underestimated over the entire upper surface. One explanation for this can be the conservative calculation of the energetic turbulent boundary layer. This can possibly be rectified by increasing the turbulence intensity of the models. The incorrect location of the stagnation point on the nose can also be cited as one of the reasons for these inaccuracies.
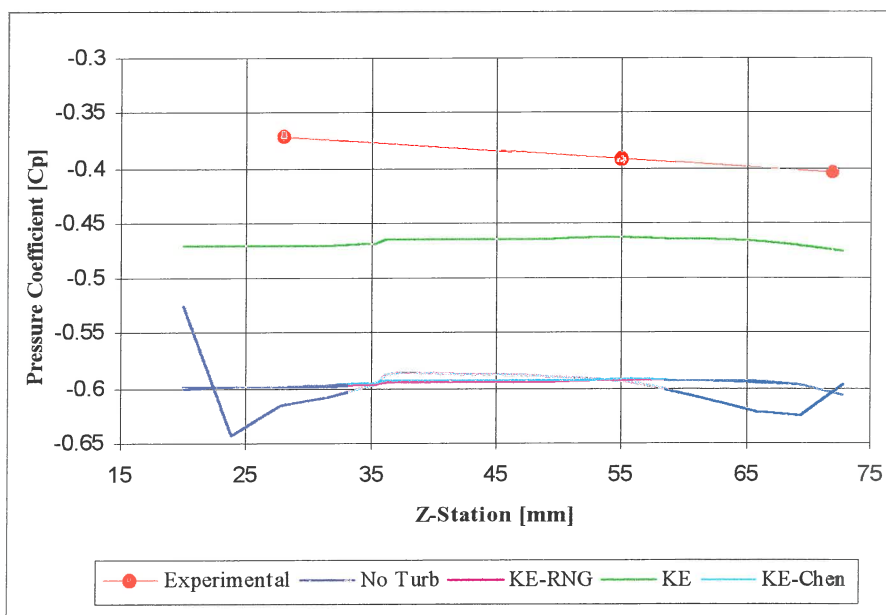
Figure 4-12 BMW Rear: CFD Turbulence model comparisons

At the rear of the vehicle, the flow is highly turbulent, completely separated and is characterised by large regions of re-circulating flow[8,16,18]. It is therefore not surprising that the turbulence models and in particular the standard k-ε model, out-perform the laminar model significantly. Although the RNG and Chen models produce results of similar magnitude to the laminar case, their pressure profiles agree better with the experimental data. As expected, the laminar model is poorly suited for the flow region presented in Figure 4-12.
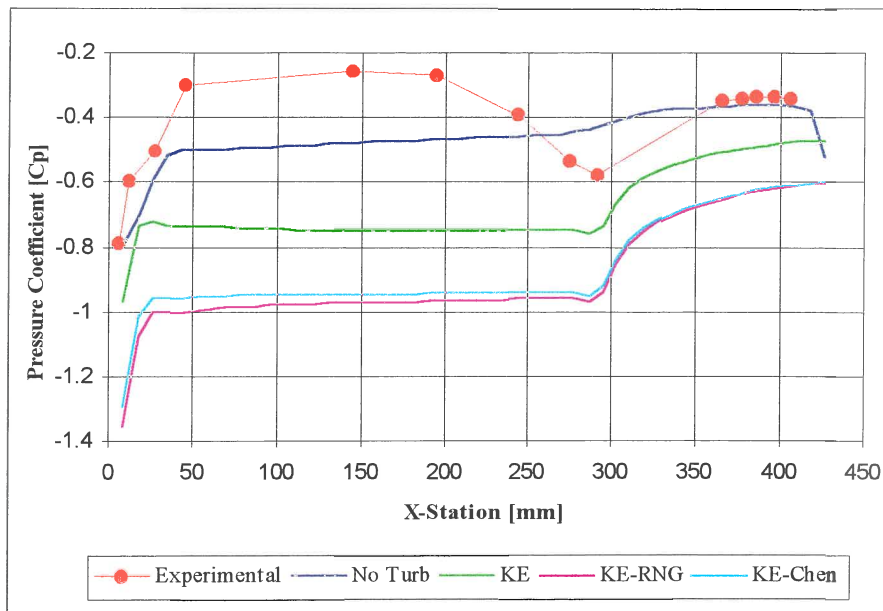
Figure 4-13 BMW Floor: CFD Turbulence model comparisons

As stated at the beginning of this chapter, this investigation was founded on the poor levels of numerical correlation in the F1 study of section 3.3. In Chapter 3 it was concluded that the absence of components such as the front splitter and rear wing had a major role to play in achieving correlation. This investigation was aimed at addressing this problem by simulating the centre-line profile of a complete vehicle.

Comparing Figure 3-24 of section 3.3 to Figure 4-13, one can see that by simulating the complete centre-line contour of the BMW, correlation has been increased in the front-splitter area. The effect of the front splitter, is clearly visible in Figure 4-13. The standard k-ε model renders the best solution in this region.

The greatest concern however, is the apparent inability of the CFD models to take the effect of the rear diffuser and its interaction with the rear end of the car into consideration. The inaccurate linear shape of the mid-section profile and the incorrect prediction of the diffuser-induced pressure drop were first observed in Figure 3-24. It seems that despite inclusion of the complete centre-line profile, the accuracy of the floor simulation has not really increased.

The findings of the experimental F1 study show that external parameters such as variations in ride height, front-flap angle adjustments and even the effect of the wheels, do not induce changes in the surface pressures which are similar in magnitude to the numerical discrepancies. This is also seen in Figure 4-8 where the removal of a relatively large GF from the rear end of

the BMW, does not produce pressure differences similar to those predicted by the CFD
models. It therefore seems unlikely that the absence of the 3D flow field is the cause of the
poor numerical results under the vehicle. The roots of the fundamental correlation
discrepancies therefore seem to point towards problems with the numerical simulation
techniques.

Two main areas can be highlighted where potential gains can be realised. These are:
- The numerical grid or computational domain
- The turbulence models and related parameters

As the extent and time scales involved in realising these potential improvements were
unknown, it was decided to conclude this study by setting out guidelines for a new study. This
discussion includes the results of three further simulations. The first investigated the effect of
grid density while the other two were directed towards the effect of turbulence parameters.

4.2.3 Future Work

The contents of this section is aimed at outlining an approach which could be followed to
improve the correlation between the numerical simulation of the centre-line profile of the 1/12th
scale BMW model and the related experimental results. The topics covered in this section are:
- The computational domain
- Turbulence models and related parameters

In conclusion, the influence of the 3D experimental flow field on the 2D simulation is also
discussed as it is appreciated that these factors will become significant once the accuracy of the
CFD model is increased.

4.2.3.1 The Computational Domain

As a first step to addressing the problem of the inaccurate computational domain, the effect of
increasing the number of grid cells has to be investigated. A grid-independent solution was not
obtained at the outset of the investigation, as it was felt that the grid resolution was high
enough to obtain an estimate of the computational accuracy.

As an indication of the effect that grid density can have on the solution, the number of grid
cells under the car was doubled. The entire grid was not modified to minimise grid generation
and computational costs. The floor area was selected as it was here (Figure 4-13) where the
poorest correlation existed. The results as shown in Figure 4-14 are compared to the solution
of the unmodified grid and to the experimental data.

From Figure 4-14 it can be seen that the higher cell density under the floor has changed the
solution slightly. Improvements were however, achieved with mixed success. Accuracy in the
front-splitter area decreased. A marginal improvement is seen in the centre-floor section and at
the entrance to the diffuser.

Further increases to the grid density or grid spacing in this area might improve the solution but
it is suggested that this is performed in conjunction with refinements around the entire vehicle.
Once a grid-independent solution has been reached, the far-field grid should then be
investigated. The cycle of far-field near-field optimisation should be repeated at least once to
ensure a truly grid-independent solution.

It is further suggested that the grid-optimisation process is performed using one of the standard STAR turbulence models, as the laminar grid, although important in determining the effect of turbulence, has been shown to be unsuitable for the flow around the BMW.
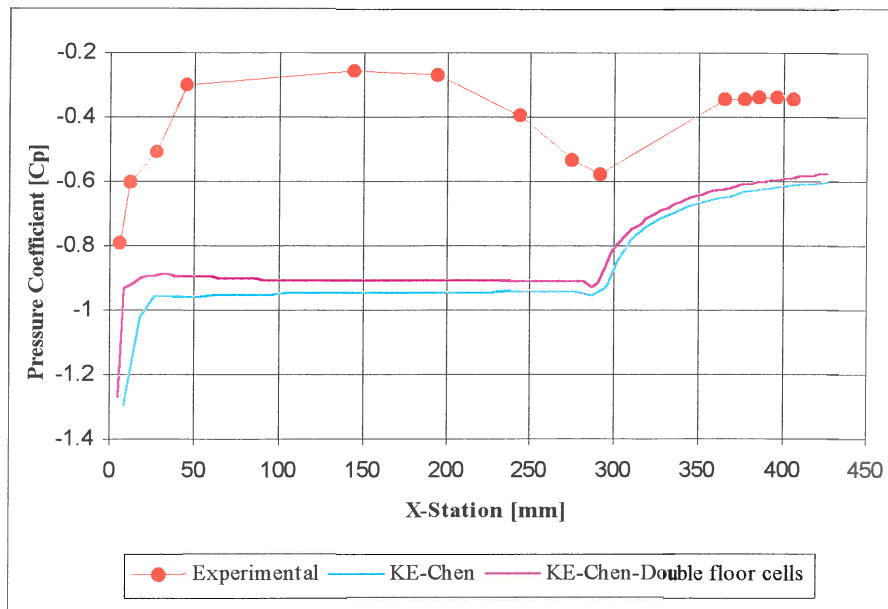
Figure 4-14 Effect of doubling the grid cells beneath the floor

If the optimised grid results in excessively skew cells, then the use of the SIMPISO algorithm, which is more robust than the SIMPLE method for severely distorted meshes, should be considered.

Once grid independence has been demonstrated, the investigation into the effects of turbulence models and related parameters has to be continued.

4.2.3.2 Turbulence Models and Related Parameters

The selection of the correct turbulence model is a difficult decision to make. It can be seen from Figure 4-10 to Figure 4-13 that the three STAR-CD models out-perform each other in different areas. Correlation in the nose area as shown in Figure 4-10 suggests that the standard k-ε model is the least suitable. Other areas such as the upper surface (Figure 4-11) and the rear end (Figure 4-12) indicate that this model is more suitable.

The choice of the correct turbulence model is complicated even further when the user definable mixing length and turbulence intensity are introduced as variables. To demonstrate this, the turbulence parameters of the standard k-ε model were varied and simulated as described in Table 4-5.

Turbulence Intensity	Mixing Length	
	0.01	0.005
0.1	Computed	–
0.01	Computed	Computed

Table 4-5 Variation of Standard k-ε parameters

The results of the simulations as outlined in Table 4-5 are compared to the experimental case in Figure 4-15.
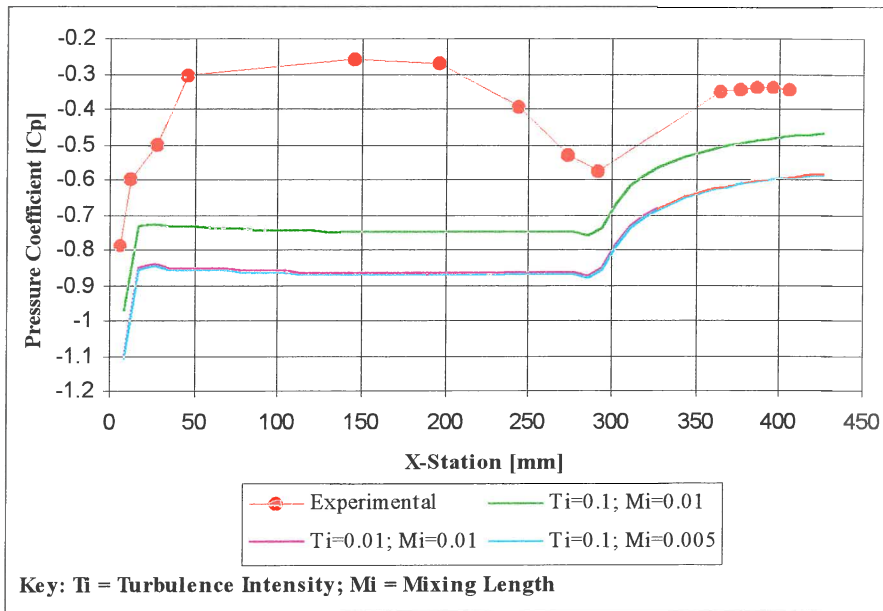
Figure 4-15 BMW Floor: Variation of k-e turbulence parameters

From Figure 4-15 it can be seen that the turbulence intensity has a more significant effect than the mixing-length parameter. It is also evident that the pressure profile of the mid-floor section remains almost unchanged. The results suggest that the intensity should be increased in the floor area. However, examination of the results above the vehicle, as presented in Figure 4-16, seem to indicate the opposite.
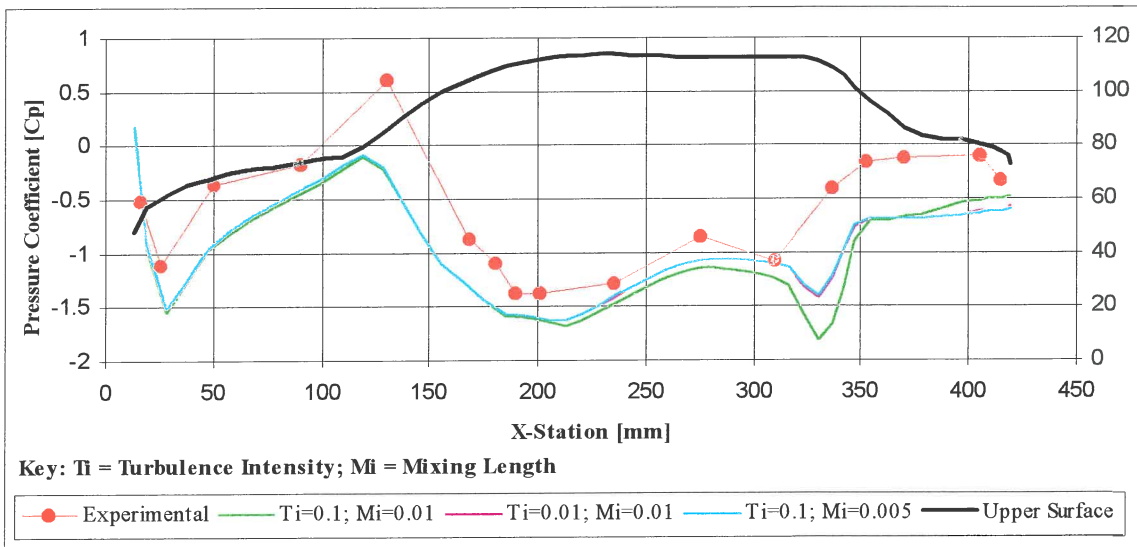
Figure 4-16 BMW Upper Surface: Variation of k-e turbulence parameters

The sensitivity of the simulations to changes in the turbulence parameters are highlighted when the coefficients of lift and drag are calculated by surface integration. As shown in Table 4-6 the lift coefficient can be changed by almost 60% by reducing the turbulence intensity by a factor of 10. The drag coefficient is less sensitive to these changes. This is to be expected as

the length to height ratio of the car suggests a greater sensitivity to pressure changes affecting forces in the direction normal to the free stream flow.

Turbulence Parameters for the k-ε model	Change in Drag Coefficient [% Δ CD]	Change in Lift Coefficient [% Δ CL]
Turbulence Intensity = 0.1 Mixing Length = 0.01	0	0
Turbulence Intensity = 0.01 Mixing Length = 0.01	7.17	-59.14
Turbulence Intensity = 0.1 Mixing Length = 0.005	7.29	-59.14

Table 4-6 Sensitivity of the solution to changes in turbulence parameters

The choice of the most representative turbulence model should only be made after an independent investigation of all three STAR models. The discussion in section 4.2.2.1 indicate that the results obtained from the standard k-ε model are unique when compared to the RNG and Chen models. This conclusion is however, only likely to hold while identical turbulence parameters are used. Comparing the k-ε model with a turbulence intensity of 0.1 to the RNG model with an intensity of 0.01, one can see from Figure 4-17, that the two models, despite their mathematical differences as described in section 2.3.3, are now in close agreement.
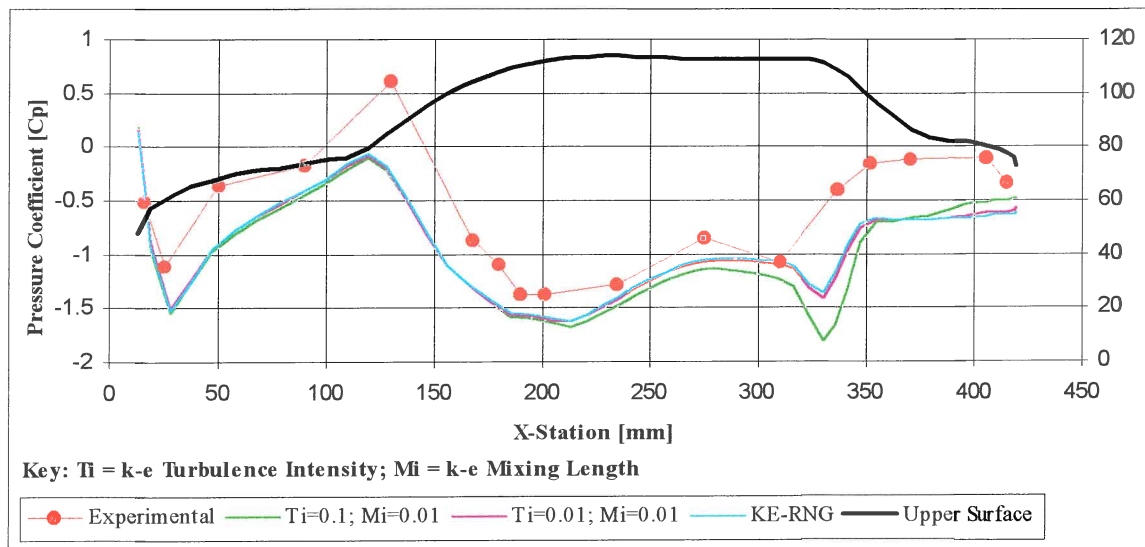
Figure 4-17 The effect of turbulence intensity on different turbulence models

As discussed in section 2.3.3 Cambers and Wilcox[34] found that the k-ε model and its derivatives were not suitable for flows where adverse pressure gradients existed. If these findings are seen to hold for the flow around the BMW, then an alternative approach such as the SST model of Menter[4] as discussed in section 2.3.3 and described in Appendix A might be more suitable. This model was specifically designed to address the deficiencies of the k-ε turbulence models.

4.2.3.3 The Effect of Excluding 3D Influences on the 2D Centre-Line Simulations

The 2D nature of the numerical simulations presented in this study, did not account for the influence of the 3D flow-field, implicitly included in the experimental results. These effects

were not clearly defined in this study and should therefore be addressed in future investigations.

Deviations from the 2D centre-line flow-case, assuming a symmetrical geometry along the centre-line of the vehicle, can be attributed to the influence of the wheels as well as the pressure differential that exists between the sides and the upper and lower surfaces of the vehicle.

In section 3.1.2.5 the effect of the wheels on the underbody flow-field was demonstrated for an open-wheel racing car. Although wheel-well flow patterns are very complicated and highly three dimensional for closed wheel cars, the effects of the wheels can be eliminated by removing the wheels and sealing the wheel-wells.

The interaction between the vehicle sides and the upper and lower surfaces are less easily neutralised. From Figure 3.7 and Figure 3.8 it can be seen that the higher side wall pressure causes an influx of air beneath the car. The net effect of this pressure increase under the floor on the centre-line is not clear. The vortices induced by the rear diffuser for both experimental models reduces the pressure in the diffuser area and therefore also influences the base pressure. These effects can be reduced by increasing the width of the vehicle until the centre-line pressure becomes insensitive to the side-wall pressures. An alternative approach would be to induce a pseudo 2D flow field along the centre-line by installing vertical walls at an appropriate distance from the centre-line. These walls would have to extend in front and behind the vehicle so that pressure differentials between the inboard and outboard side would not induce the formation of vortices in the test area. The y-position of these boards should also take the effect of boundary layer formation along their sides into account.

4.3 Conclusion

The aim of this investigation was to determine the accuracy with which a centre-line numerical simulation could be used to predict the pressure distribution on the centre line of a racing car. This was an extension of the computational work performed on the floor of the Parmalat Forti Ford F1 racing car in Chapter 3.

A 1/12th scale model of a Generic BMW Touring car was selected for this investigation as it provided an ideal balance between the experimental and numerical detail, the costs and the efficiency with which results could be obtained.

The accuracy of the simulated results was verified using experimentally measured data. The data was obtained by building a model of the BMW, fitting it with surface-static pressure ports and testing it in a stationary-road closed-return wind tunnel. The measurements required for the computational investigation were made after repeatability and Reynolds-Number independence had been established. The experimental investigation was also used to establish a link with the F1 investigation by comparing the floor-pressure distributions of each case. It was found that the pressure plot under the BMW was in good agreement with the Forti distribution. As expected, the characteristic shape of the distribution under the open-wheel racing car was more pronounced and at a significantly lower average pressure.

The experimental investigation was also used to demonstrate and explain the phenomena responsible for rear downforce on sedan-based racing cars.

The numerical investigation was based on the centre-line profile of the wind-tunnel model. The grid was constructed using PRO-STAR. The effect of the three high Reynolds-Number turbulence models included in the STAR-CD software was investigated. These were compared to a laminar flow case and to the wind-tunnel results. It was found that although correlation exists in certain areas, the poorest correlation is found beneath the floor. This is ascribed to inaccuracies in the numerical procedures.

The combination of the inaccurate computational techniques and the varying success of the different turbulence models meant that satisfactory correlation could not be obtained. To address these deficiencies, an outline was laid down for a new study, aimed at improving the numerical model. It was suggested that by improving the mesh density and by altering the turbulence parameters, correlation could be improved. These suggestions were substantiated by further simulations. The use of turbulence models more suited to adverse pressure gradients was also included in the recommendations.

It was also shown that by varying the turbulence parameters, two different variations of the k-ε model could be tuned to predict similar results.

A short discussion on the influence of the 3D flow-field on the centre-line simulations conclude this chapter.

5. CONCLUSION

Race car aerodynamics has been transformed over the last four decades from a "cottage" industry, by designers like Colin Chapman who had the ingenious idea of reclining the drivers seat to reduce the frontal area, to a highly technical and sophisticated industry. Radical improvements of the past such as the introduction of wings or ground effects are rarely seen in the modern racing industry. Vast amounts of resources are now spent on obtaining the smallest advantage over the closest competitor. This is partly due to the law of diminishing returns but also due to the continuously shrinking size of the aerodynamic rule box. This was the case in 1995 when large chunks were taken out of the F1 rule box by the F.I.A. One of the areas that was significantly affected was the floor of the racing car. The flat-bottomed cars of the 1994 season were transformed to stepped-bottomed vehicles by removing two rectangular blocks, one on either side of the centre line, from the rule box. Such changes challenge the aerodynamicist to limit and neutralise the negative effect of the rule changes on lap times. As a first step to curbing the aerodynamic damage in a particular area, in this case the floor, the impact of the rules on the flow had to be established. An investigation into the flow beneath the floor of an F1 car was therefore launched.

The aim of this study was to investigate the flow patterns beneath a 30% scale model of the Parmalat Forti Ford FG01-95 Formula One racing car by using experimental and numerical methods. The experimental aim of the investigation was to determine the elements of the car, external to the floor, which were dominant in producing the flow-field patterns beneath the car. The experimental data was also used to investigate the numerical accuracy of simulating the centre-line profile of the floor.

The experimental results were obtained by building the 30% scale model, fitting the floor with static-surface pressure ports and testing it in the rolling-road LWST of the CSIR, South Africa. The results showed that the centre-line pressure profile characteristic to flat-bottomed racing cars was still clearly visible. It was found that the wheels were dominant in modifying the pressure distribution under the floor. It was further shown that only the front or rear wheel sets were required to induce these changes.

The numerical investigation was aimed at reproducing the wind-tunnel results by imposing experimentally measured boundary conditions on the grid of the centre-line profile of the isolated racing-car floor. The grid was constructed by using an algebraic grid generator and the simulations were performed using two CFD codes. One was an in-house code using Roe's flux difference splitting method and the other employed the SIMPLE algorithm of STAR-CD. It was found that although the correct trends could be observed when the ride heights were modified, absolute correlation could not be achieved. The absence of components such as the front splitter and rear-wing assembly were sited as the most likely cause for the discrepancies.

To increase the amount of model detail in the computational simulations, a new investigation was launched. In this investigation the complete centre-line profile of a $1/12^{th}$ scale generic model of a BMW Touring Car was used. The data for the numerical correlation was obtained from experimentally measured static-surface pressures. The stationary-floor wind tunnel at the University of Pretoria in South Africa, was used to measure the pressures on the centre-line around the circumference of the scale model. The experimental results were also used to establish a link with the F1 investigation by comparing the centre-line floor pressure

distribution of the two cases. By adding a Gurney Flap to the rear of the BMW the principles at play when generating rear downforce for sedan-based racing cars were also demonstrated.

The numerical BMW grid was constructed using PRO-STAR and solutions were obtained using the SIMPLE algorithm of STAR-CD. The results of three different k-ε turbulence-model simulations showed that despite limited success in certain areas around the vehicle, the inclusion of entire vehicle profile did not significantly increase correlation. The poor correlation was attributed to inaccuracies in the numerical methodology. It was proposed that another investigation, aimed at improving the numerical simulations, was required but that this study went beyond the scope of this script. Guidelines for the new investigation, based on the results of three additional simulations, were laid down. The related discussions suggested that a refined grid and a study into the effect of the user-definable turbulence parameters might improve the solution. It was also proposed that if the three turbulence models were found to be unsuitable, a more appropriate model such as the SST model of Menter should be used.

It is the author's belief that, although accurate numerical correlation could not be established in this study, CFD would, like wind tunnels, soon become an essential tool in the race-car aerodynamicist's quest for glory.

6. REFERENCES

1. Morrison, I., "The Guiness Guide to Formula One", Ian Morrison and Guiness Publishing Ltd., 1989.
2. Roe, P. L., " Characteristic-Based Schemes for the Euler Equations", Ann. Rev. Fluid Mech. 1986, 18:337-65
3. STAR-CD, Version 2.30 manuals, Computational Dynamics Ltd., London, U.K., 1995.
4. Menter, F. R., "Two-Equation Eddy-Viscosity Turbulence Models For Engineering Applications", AIAA J., Vol. 32, No. 8, August 1994.
5. The New Encyclopaedia Brittanica, 15th edition, Vol. 1, pp 728, The Encyclopaedia Brittanica Inc., 1993.
6. Setright, L. J. K., "The Pirelli History of Motor Sport", Frederick Muller Limited, 1981.
7. Dominy, R. G., "Aerodynamics of Grand Prix Cars", Proc. Instn. Mech. Engrs., Vol. 206, IMechE, 1992.
8. Katz, J., "Race Car Aerodynamics: Designing for Speed", Robert Bentley Publishers, 1995.
9. Akanni, S., "Running Rampant", Racecar Engineering, Vol. 5, No. 2, pp. 44-49, 1995.
10. Hanna, R.K., "Use of Unstructured Grids in the Analysis of the Formula One Benneton Car", 1st South African Conference on Applied Mechanics '96, South Africa, July 1-5, 1996.
11. Rae, W. H. and Pope, A., "Low Speed Wind tunnel Testing", Second Edition, John Wiley & Sons, 1984.
12. Houghton, E. L. and Carruthers, N. B., "Aerodynamics for Engineering Students", Third Edition, Edward Arnold, 1988.
13. Katz, J. and Largman, R., "Experimental Study of the Aerodynamic Interaction Between an Enclosed-Wheel Racing Car and its Rear Wing", Journal of Fluids Engineering, Vol. 111, June 1989.
14. Mercker, E. and Knape, K. W., "Ground Simulation with Moving Belt and Tangential Blowing for Full Scale Automotive Testing in a Wind tunnel", SAE Technical Paper Series, 890367, Detroit, Michigan, 1989.
15. Garry, K.P., Wallis, S.B., Cooper, K. R., Fediw, A., Wilsden, D. J., "The Effect on Aerodynamic Drag of the Longitudinal Position of a Road Vehicle Model in a Wind tunnel Test Section", SAE Paper 940414, 1994.
16. Barnard, R. H., "Road Vehicle Aerodynamic Design An Introduction" Addison Wesley Longman Limited, First Edition, 1996.
17. Milliken, W. F., Milliken, D. L., "Race Car Vehicle Dynamics", SAE International, 1995.
18. Hucho, W., "Aerodynamics of Road Vehicles", Butterworths, 1987.
19. Bertin, J. J., and Smith, M. L., "Aerodynamics for Engineers", Second Edition, Prentice-Hall International Editions, 1989.
20. "Bosch Automotive handbook", Robert Bosch GmbH, 2nd edition, 1986.
21. Blevins, D. R., "Applied Fluid Dynamics Handbook" ,Van Nostrand Reinold Company, 1984.
22. Smith, C. "Swift is Sure", Racecar Engineering, Vol.5 No. 3, 1995.
23. Masaru Ishizuka, " Flow Resistance Correlation of Wire Nets in a Wide Range of Reynolds Numbers for Thermal Design of Electronic Equipment", Journal of Fluids Engineering, Vol. 118, September 1996.
24. Sykes, D. M., "Advances in Road Vehicle Aerodynamics", BHRA Fluid Engineering, Cranfield, Bedford, pp311-321, 1973.

25. Mercker, E., Breuer, N., Berneburg, H. and Emmelmann, H. J., "On the Aerodynamic Interference Due to the Rolling Wheels of Passanger Cars", SAE Paper 910311, 1991.
26. Cogotti, A., "Aerodynamic Characteristics of Car Wheels - Impact of aerodynamics on vehicle design." International Journal of Vehicle Design, SP3, London, 1983.
27. Private conversation with Hans Fouché, former Chief Aerodynamicist at Brabham Grand Prix and Forti Corse Formula One Racing, 1995.
28. Craig, K. J., "Computational Fluid Dynamics - MVB780", Lecture Notes, University of Pretoria, South Africa, 1994.
29. Fletcher C.A.J., "Computational Techniques for Fluid Dynamics", Volume II, Second Edition, Springer Verlag, 1991.
30. Anderson, D. A., Tannehill, J. C. and Pletcher, R. H., "Computational Fluid Mechanics and Heat Transfer", Hemisphere Publishing Co-orporation, 1984.
31. Holst T.L., CFD Notes Stanford.
32. Hoffman, K. A., "Computational Fluid Dynamics for Engineers", Engineering Education Systems™, 1989.
33. Marvin, J. G., "Turbulence modelling for Computational Aerodynamics", AIAA J. Vol. 21, No. 7, July 1983.
34. Chambers, T. L. and Wilcox, D. C., " Critical Examination of Two-Equation Turbulence Closure Models for Boundary Layers", AIAA J., Vol. 15, No. 6, June 1977.
35. Yang, Z. and Shih, T. H., "New Time Scale Based k-ε Model for Near Wall Turbulence", AIAA J. Vol. 31, No.7, July 1993.
36. Wilcox, D. C., "Reassessment of the Scale-Determining Equation for Advanced Turbulence Models", AIAA J. Vol. 26, No. 11, November 1988.
37. Menter, F. R., "Influence of Free Stream Values on k-ω Turbulence Model Predictions", AIAA J., Vol. 30, No. 6, 1992.
38. Wilcox, D. C., "Comparison of Two-Equation Turbulence Models for Boundary Layers with Pressure Gradient", AIAA J. Vol. 31, No. 8, August 1993.
39. Craig, K. J., "Numerical Thermo Fluids - MSM780", Grid Generation Lecture Notes, University of Pretoria, South Africa, 1994.
40. Craig, K. J., "Computational Study of Blowing on Delta Wings at High Alpha", AIAA J. Aircraft, Vol.30, No.6, Nov.-Dec. 1993.
41. Thompson, J. F., Warsi, Z. U. A. and Mastin, C. W., "Numerical Grid Generation: Foundations and Applications", North-Holland, New York, 1985.
42. MacCormack, R. W., Lecture notes AA214B,C, Department of Aeronautics and Astronautics, Stanford University, CA, USA, 1990.
43. Mazaheri, K., Roe, P. L., "New Light On Numerical Boundary Conditions", AIAA-91-1600-CP, 1991.
44. Wei Shyy, "Numerical Outflow Boundary Conditions for Navier-Stokes Flow Calculations by a Line Iterative Method", AIAA J., Vol. 23, No. 12, December 1985.
45. F.I.A., "1995 Formula One Technical Regulations", Fédération Internationale de l'Automobile, 1994.
46. Cogotti, A., "Aerodynamic Characteristics of Car Wheels - Impact of aerodynamics on vehicle design." International Journal of Vehicle Design, SP3, London, 1983.
47. Sykes, D. M., "Advances in Road Vehicle Aerodynamics", BHRA Fluid Engineering, Cranfield, Bedford, pp311-321, 1973.
48. Hirsch, C., Numerical Computation of Internal and External Flows, Vol. 2, John Wiley and Sons, 1990.

Appendix A The Shear Stress Transport Model of Menter

The details of the Shear Stress Transport Model of Menter[4] is outlined in this Appendix.

Dropping the primes and tilda's that donate mean quantities, the governing equations for general compressible turbulent flows as given by Wilcox[36] and Menter[37] can be summarised as:

Mass Conservation:

$$\frac{\partial \rho}{\partial t} + \frac{\partial}{\partial x_j}\left(\rho u_j\right) = 0$$

Equation A-1

Momentum conservation:

$$\frac{\partial}{\partial t}\left(\rho u_i\right) + \frac{\partial}{\partial x_j}\left(\rho u_j u_i\right) = -\frac{\partial p}{\partial x_i} + \frac{\partial \tau_{ji}}{\partial x_j}$$

Equation A-2

Mean energy conservation:

$$\frac{\partial}{\partial t}\left(\rho E\right) + \frac{\partial}{\partial x_j}\left(\rho u_j H\right) = \frac{\partial}{\partial x_j}\left[u_i \tau_{ij} + \left(\mu + \sigma_k \mu_T\right)\frac{\partial k_T}{\partial x_j} - q_j\right]$$

Equation A-3

Turbulent mixing energy:

$$\frac{\partial}{\partial t}\left(\rho k_T\right) + \frac{\partial}{\partial x_j}\left(\rho u_j k_T\right) = \tau_{ij}^T \frac{\partial u_i}{\partial x_j} - \beta^* \rho \omega k_T + \frac{\partial}{\partial x_j}\left[\left(\mu + \sigma_k \mu_T\right)\frac{\partial k_T}{\partial x_j}\right]$$

Equation A-4

Specific dissipation rate:

$$\frac{\partial}{\partial t}\left(\rho \omega\right) + \frac{\partial}{\partial x_j}\left(\rho u_j \omega\right) = \left(\frac{\gamma}{\upsilon_T}\right)\tau_{ij}^T \frac{\partial u_i}{\partial x_j} - \beta \rho \omega^2{}_T + \frac{\partial}{\partial x_j}\left[\left(\mu + \sigma_\omega \mu_T\right)\frac{\partial \omega}{\partial x_j}\right]$$
$$+ 2\left(1 - F_1\right)\rho \sigma_{\omega 2}\frac{1}{\omega}\frac{\partial k}{\partial x_j}\frac{\partial \omega}{\partial x_j}$$

Equation A-5

Closure

The closure constants ϕ of this model are calculated from the constants of the k-ω (ϕ_1) and the k-ε (ϕ_2) models as follows:

$$\phi = F_1\phi_1 + (1-F_1)\phi_2$$

Equation A-6

where the constants ϕ_1 of the k-ω model are:

$\beta_1 = 0.0750$;　　　$\beta^* = 0.09$;　　　$\kappa = 0.41$;　　　$\sigma_{k1} = 0.85$;

$\sigma_{\omega 1} = 0.5$;　　　$\gamma_1 = \beta_1/\beta^* - \sigma_{\omega 1}\kappa^2/\sqrt{\beta^*}$;　　　$a_1 = 0.31$

and the constants ϕ_2 of the k-ε model are:

$\beta_2 = 0.0828$;　　　$\beta^* = 0.09$;　　　$\kappa = 0.41$;　　　$\sigma_{k2} = 1.0$;

$\sigma_{\omega 2} = 0.856$;　　　$\gamma_2 = \beta_2/\beta^* - \sigma_{\omega 2}\kappa^2/\sqrt{\beta^*}$

The eddy viscosity is defined as:

$$v_t = \frac{a_1 k}{\max(a_1 \omega; \Omega F_2)}$$

where $\Omega = |\delta u / \delta y|$ is the absolute value of vorticity. The blending function F_2 is given by:

$$F_2 = \tanh(\text{arg}_2^2); \qquad \text{arg}_2 = \max\left(2\frac{\sqrt{k}}{0.09\omega y}; \frac{500v}{y^2 \omega}\right)$$

The blending function F_1 is defined as:

$$F_1 = \tanh(\text{arg}_1^4); \qquad \text{arg}_1 = \min\left[\max\left(\frac{\sqrt{k}}{0.09\omega y}; \frac{500v}{y^2 \omega}\right); \frac{4\rho\sigma_{\omega 2} k}{CD_{k\omega} y^2}\right]$$

where y is the distance to the next surface point and $CD_{k\omega}$ is:

$$CD_{kw} = \max\left(2\rho\sigma_{\omega 2}\frac{1}{\omega}\frac{\partial k}{\partial x_j}\frac{\partial \omega}{\partial x_j}; 10^{-20}\right)$$

The turbulent shear stress τ^T_{ij} is defined as: $\tau^T_{ij} = \tau_{ij} - \sigma_{ij}$
The total energy E is defined as: $E = e_i + k_T + u_i u_i / 2$

The heat-flux vector q_j is approximated as: $q_i = -\left(\frac{\mu}{\text{Pr}_L} + \frac{\mu_T}{\text{Pr}_T}\right)\frac{\partial h}{\partial x_j}$

where h is the internal enthalpy defined as: $h = e + p/\rho$

Writing the governing equations in the special vector format all fluxes remain unchanged except for the viscous energy fluxes which become:

$$\widetilde{\beta_i} = \widetilde{u_i}\widetilde{\tau_{ij}} + \left(\mu + \sigma_k \mu_T\right)\frac{\partial k_t}{\partial x_i} - q_i$$

Although the SST method is more difficult to code, Menter claims that there is almost no loss in computational efficiency compared to the k-ω model.

Boundary Conditions For Numerical Implementation of The TTS Model
At the surface (y = 0) the following conditions must be specified:

No slip   : $u_w = k_T = 0$
Wall temperature or heat flux   : T_w / Q_w
Dissipation rate   : ω_w

Smooth surface & no mass injection   : $\omega_w = 10\frac{6v_w}{\beta_1 (\Delta y_1)^2}$, where Δy_1 is the distance to the

next point away from the wall
: $v_w^+ = 0$
: $\Delta y_1^+ < 3$

Rough surface & no mass injection $\quad:\quad \omega_w = \dfrac{u_\tau^2}{\nu} S_R$ where $SR = \begin{cases} \left(\dfrac{50}{k_R^+}\right)^2, k_R^+ \langle 25 \\[3mm] \dfrac{100}{k_R^+}, k_R^+ \geq 25 \end{cases}$

$$k_R^+ = \frac{u_\tau k_R}{\nu}$$

$$u_\tau^2 = \left(\nu + \nu_T\right)\frac{\partial u}{\partial y} \quad ;$$

k_R = average height of sand grain roughness elements

Mass injection $\quad:\quad \omega = \dfrac{u_\tau^2}{\nu_w} S_B$ and $v = v_w$ where,

$$S_B = \frac{20}{v_w^+\left(1 + 5v_w^+\right)} \text{ and } v_w^+ = \frac{v_w}{u_\tau}$$

The following choice of free-stream values is recommended:

$\omega_\infty = (1 \rightarrow 10)U_\infty / L;$ $\qquad\qquad v_{t\infty} = 10^{-(2\rightarrow 5)} v_\infty;$ $\qquad\qquad k_\infty = v_{t\infty}\, \omega_\infty$

Appendix B The Flux Difference Splitting Method of ROE

The development of the numerical solver as used in the computational investigation of Chapter 3 is presented in this Appendix.

Implicit Algorithm

The algorithm for Roe's Flux Difference Splitting Method for the full 3D RANS equations is outlined in this section. A 2D thin layer version of Roe's method as described by Craig[28] was used as the basis for expansion. The thin layer algorithm was originally outlined by MacCormack[41]. A similar description is also given by Hirsch[48].

The Navier-Stokes equations as found in section 2.3.1 of the literature study can be written in 3D as:

$$\tilde{U}_t = \tilde{F}_\varepsilon + \tilde{G}_\tau + \tilde{H}_\zeta = 0$$

where

$$\tilde{U} = UV = UJ^{-1}$$

and

$$\tilde{F} = \tilde{F}_e + \tilde{F}_v; \quad \tilde{G} = \tilde{G}_e + \tilde{G}_v; \quad \tilde{H} = \tilde{H}_e + \tilde{H}_v$$

Equation B-1

The subscripts e denotes Euler fluxes and v viscous fluxes.

The implicit 3D algorithm which uses Roe's flux splitting is given as:

$$\left\{ \begin{aligned} & I + \frac{\Delta t}{V_{i,j,k}} \left(\frac{D_+}{\Delta\xi}\tilde{A}_- + \frac{D_-}{\Delta\xi}\tilde{A}_+ + \frac{D_+}{\Delta\eta}\tilde{B}_- + \frac{D_-}{\Delta\eta}\tilde{B}_+ + \frac{D_+}{\Delta\zeta}\tilde{C}_- + \frac{D_-}{\Delta\zeta}\tilde{C}_+ \right) \\ & + \frac{\Delta t}{V_{i,j,k}} \left(\frac{D}{\Delta\xi}\tilde{F}_v + \frac{D}{\Delta\xi}\tilde{G}_v + \frac{D}{\Delta\xi}\tilde{H}_v \right) \end{aligned} \right\} \partial U_{i,j,k} = \Delta U_{i,j,k}$$

where the explicit driving term is:

$$\Delta U_{i,j,k}^n = -\frac{\Delta t}{V_{i,j,k}} \left(\frac{D_+}{\Delta\xi}\tilde{F}_{e-} + \frac{D_-}{\Delta\xi}\tilde{F}_{e+} + \frac{D_+}{\Delta\eta}\tilde{G}_{e-} + \frac{D_-}{\Delta\eta}\tilde{G}_{e+} + \frac{D_+}{\Delta\zeta}\tilde{H}_{e-} + \frac{D_-}{\Delta\zeta}\tilde{H}_{e+} \right)_{i,j,k}^n$$

$$+ \frac{\Delta t}{V_{i,j,k}} \left(\frac{D_+}{\Delta\xi}\tilde{F}_{v-} + \frac{D_-}{\Delta\xi}\tilde{F}_{v+} + \frac{D_+}{\Delta\eta}\tilde{G}_{v-} + \frac{D_-}{\Delta\eta}\tilde{G}_{v+} + \frac{D_+}{\Delta\zeta}\tilde{H}_{v-} + \frac{D_-}{\Delta\zeta}\tilde{H}_{v+} \right)_{i,j,k}^n$$

Equation B-2

As the algorithm is a pentadiagonal matrix which is expensive to invert, Gauss-Seidel Line relaxation is employed to convert the algorithm to a block-tri-diagonal matrix which can be solved efficiently. After line relaxation, descritizisation and the re-writing of the implicit viscous fluxes in terms of M-matrices (M-matrices are explained later in this appendix) the algorithm becomes:

$$\tilde{B}\delta U_{i,j+1,k} + \tilde{A}\delta U_{i,j,k} + \tilde{C}\delta U_{i,j-1,k} = \Delta U_{i,j,k}^n - \tilde{D}\delta U_{i+1,j,k} - \tilde{E}\delta U_{i-1,j,k} - \tilde{O}\delta U_{i,j,k+1} - \tilde{P}\delta U_{i,j,k-1}$$

Equation B-3

where matrices $\hat{A}, \hat{B}, \hat{C}, \hat{D}, \hat{E}, \hat{O}$ and $\hat{P}$ are defined as:

$$\hat{A} = I + \frac{\Delta t}{V_{i,j,k}}\left(\widetilde{A}_{+_{i+\frac{1}{2},j,k}} - \widetilde{A}_{-_{i-\frac{1}{2},j,k}} + \widetilde{B}_{+_{i,j+\frac{1}{2},k}} - \widetilde{B}_{-_{i,j-\frac{1}{2},k}} + \widetilde{C}_{+_{i,j,k+\frac{1}{2}}} - \widetilde{C}_{-_{i,j,k-\frac{1}{2}}}\right)$$

$$+ \frac{\Delta t}{V_{i,j,k}}\left(M^{11}_{i+\frac{1}{2}}N_{i,j,k} + M^{11}_{i-\frac{1}{2}}N_{i,j,k} + M^{22}_{j+\frac{1}{2}}N_{i,j,k} + M^{22}_{j-\frac{1}{2}}N_{i,j,k} + M^{33}_{k+\frac{1}{2}}N_{i,j,k} + M^{33}_{k-\frac{1}{2}}N_{i,j,k}\right)$$

$$\hat{B} = \frac{\Delta t}{V_{i,j,k}}\widetilde{B}_{-_{i,j+\frac{1}{2},k}} - \frac{\Delta t}{V_{i,j,k}}\left(\begin{array}{l} M^{22}_{j+\frac{1}{2}}N_{i,j+1,k} + \frac{1}{4}M^{12}_{i+\frac{1}{2}}N_{i,j+1,k} - \frac{1}{4}M^{12}_{i-\frac{1}{2}}N_{i,j+1,k} + \frac{1}{4}M^{32}_{k+\frac{1}{2}}N_{i,j+1,k} \\ -\frac{1}{4}M^{32}_{k-\frac{1}{2}}N_{i,j+1,k} \end{array}\right)$$

$$\hat{C} = -\frac{\Delta t}{V_{i,j,k}}\widetilde{B}_{+_{i,j-\frac{1}{2},k}} - \frac{\Delta t}{V_{i,j,k}}\left(\begin{array}{l} M^{22}_{j-\frac{1}{2}}N_{i,j-1,k} - \frac{1}{4}M^{12}_{i+\frac{1}{2}}N_{i,j-1,k} + \frac{1}{4}M^{12}_{i-\frac{1}{2}}N_{i,j-1,k} + \frac{1}{4}M^{32}_{k+\frac{1}{2}}N_{i,j-1,k} \\ -\frac{1}{4}M^{32}_{k-\frac{1}{2}}N_{i,j-1,k} \end{array}\right)$$

$$\hat{D} = \frac{\Delta t}{V_{i,j,k}}\widetilde{A}_{-_{i+\frac{1}{2},j,k}} - \frac{\Delta t}{V_{i,j,k}}\left(\begin{array}{l} \frac{1}{4}M^{21}_{j+\frac{1}{2}}N_{i+1,j-1,k} + \frac{1}{4}M^{21}_{j+\frac{1}{2}}N_{i+1,j,k} - \frac{1}{4}M^{21}_{j-\frac{1}{2}}N_{i+1,j,k} - \frac{1}{4}M^{21}_{j-\frac{1}{2}}N_{i+1,j-1,k} \\ -\frac{1}{4}M^{12}_{i+\frac{1}{2}}N_{i+1,j+1,k} - \frac{1}{4}M^{12}_{i+\frac{1}{2}}N_{i+1,j-1,k} + \frac{1}{4}M^{11}_{i+\frac{1}{2}}N_{i+1,j,k} + \frac{1}{4}M^{13}_{i+\frac{1}{2}}N_{i+1,j,k+1} \\ -\frac{1}{4}M^{13}_{k+\frac{1}{2}}N_{i+1,j,k-1} + \frac{1}{4}M^{31}_{k+\frac{1}{2}}N_{i+1,j,k} + \frac{1}{4}M^{31}_{k+\frac{1}{2}}N_{i+1,j,k+1} - \frac{1}{4}M^{31}_{k-\frac{1}{2}}N_{i+1,j,k} \\ -\frac{1}{4}M^{31}_{k-\frac{1}{2}}N_{i+1,j,k-1} \end{array}\right)$$

$$\hat{E} = -\frac{\Delta t}{V_{i,j,k}}\widetilde{A}_{+_{i-\frac{1}{2},j,k}} - \frac{\Delta t}{V_{i,j,k}}\left(\begin{array}{l} -\frac{1}{4}M^{21}_{j+\frac{1}{2}}N_{i-1,j+1,k} - \frac{1}{4}M^{21}_{j+\frac{1}{2}}N_{i-1,j,k} + \frac{1}{4}M^{21}_{j-\frac{1}{2}}N_{i-1,j,k} + \frac{1}{4}M^{21}_{j-\frac{1}{2}}N_{i-1,j-1,k} \\ -\frac{1}{4}M^{12}_{i-\frac{1}{2}}N_{i-1,j+1,k} + \frac{1}{4}M^{12}_{i-\frac{1}{2}}N_{i-1,j-1,k} + \frac{1}{4}M^{11}_{i-\frac{1}{2}}N_{i-1,j,k} - \frac{1}{4}M^{13}_{i-\frac{1}{2}}N_{i-1,j,k+1} \\ +\frac{1}{4}M^{13}_{i-\frac{1}{2}}N_{i-1,j,k-1} - \frac{1}{4}M^{31}_{k+\frac{1}{2}}N_{i-1,j,k+1} - \frac{1}{4}M^{31}_{k+\frac{1}{2}}N_{i-1,j,k} + \frac{1}{4}M^{31}_{k-\frac{1}{2}}N_{i-1,j,k} \\ +\frac{1}{4}M^{31}_{k-\frac{1}{2}}N_{i-1,j,k-1} \end{array}\right)$$

$$\hat{O} = \frac{\Delta t}{V_{i,j,k}}\hat{C}_{-_{i,j,k+\frac{1}{2}}} - \frac{\Delta t}{V_{i,j,k}}\left(\begin{array}{l} M^{33}_{k+\frac{1}{2}}N_{i,j,k+1} + \frac{1}{4}M^{13}_{k+\frac{1}{2}}N_{i,j,k+1} - \frac{1}{4}M^{13}_{i-\frac{1}{2}}N_{i,j,k+1} - \frac{1}{4}M^{23}_{j-\frac{1}{2}}N_{i,j,k+1} \\ +\frac{1}{4}M^{23}_{j+\frac{1}{2}}N_{i,j,k+1} + \frac{1}{4}M^{23}_{j+\frac{1}{2}}N_{i,j+1,k+1} - \frac{1}{4}M^{23}_{j-\frac{1}{2}}N_{i,j-1,k+1} + \frac{1}{4}M^{32}_{k+\frac{1}{2}}N_{i,j+1,k+1} \\ -\frac{1}{4}M^{32}_{k+\frac{1}{2}}N_{i,j-1,k+1} \end{array}\right)$$

$$\hat{P} = -\frac{\Delta t}{V_{i,j,k}}\hat{C}_{+_{i,j,k-\frac{1}{2}}} - \frac{\Delta t}{V_{i,j,k}}\left(\begin{array}{l} M^{33}_{k-\frac{1}{2}}N_{i,j,k-1} - \frac{1}{4}M^{13}_{k+\frac{1}{2}}N_{i,j,k-1} + \frac{1}{4}M^{13}_{i-\frac{1}{2}}N_{i,j,k-1} - \frac{1}{4}M^{23}_{j+\frac{1}{2}}N_{i,j,k-1} \\ +\frac{1}{4}M^{23}_{j-\frac{1}{2}}N_{i,j,k-1} - \frac{1}{4}M^{23}_{j+\frac{1}{2}}N_{i,j+1,k-1} + \frac{1}{4}M^{23}_{j-\frac{1}{2}}N_{i,j-1,k-1} - \frac{1}{4}M^{32}_{k-\frac{1}{2}}N_{i,j+1,k-1} \\ +\frac{1}{4}M^{32}_{k-\frac{1}{2}}N_{i,j-1,k-1} \end{array}\right)$$

Equation B-4

and the explicit driving term becomes:

$$\Delta U^n_{i,j,k} = \left[\begin{array}{l} -\frac{\Delta t}{V_{i,j,k}}\left(\widetilde{F}_{e_{i+\frac{1}{2}}} - \widetilde{F}_{e_{i-\frac{1}{2}}} + \widetilde{G}_{e_{j+\frac{1}{2}}} - \widetilde{G}_{e_{j-\frac{1}{2}}} + \widetilde{H}_{e_{k+\frac{1}{2}}} - \widetilde{H}_{e_{k-\frac{1}{2}}}\right) \\ +\frac{\Delta t}{V_{i,j,k}}\left(\widetilde{F}_{v_{i+\frac{1}{2}}} - \widetilde{F}_{v_{i-\frac{1}{2}}} + \widetilde{G}_{v_{j+\frac{1}{2}}} - \widetilde{G}_{v_{j-\frac{1}{2}}} + \widetilde{H}_{v_{k+\frac{1}{2}}} - \widetilde{H}_{v_{k-\frac{1}{2}}}\right) \end{array}\right]^n_{i,j,k}$$

Equation B-5

<u>Euler Fluxes</u>

The geometric-averaged Jacobians $\hat{A}, \hat{B}$ and $\hat{C}$ are split through polarity of rotated eigen-values and are calculated as follows:

$$\hat{A}_\pm = S^{-1}R_A^{-1}C_A^{-1}\Lambda_{A_\pm}C_AR_AS; \quad \hat{B}_\pm = S^{-1}R_B^{-1}C_B^{-1}\Lambda_{B_\pm}C_BR_BS; \quad \hat{C}_\pm = S^{-1}R_C^{-1}C_C^{-1}\Lambda_{C_\pm}C_CR_CS;$$

$$\hat{A} = \hat{A}\!\left(\hat{U}\right);$$

$$\hat{\rho} = \sqrt{\rho_L}\sqrt{\rho_R}$$

$$\hat{u} = \frac{\left(\sqrt{\rho_L}\,u_L + \sqrt{\rho_R}\,u_R\right)}{\left(\sqrt{\rho_L} + \sqrt{\rho_R}\right)}$$

$$\hat{v} = \frac{\left(\sqrt{\rho_L}\,v_L + \sqrt{\rho_R}\,v_R\right)}{\left(\sqrt{\rho_L} + \sqrt{\rho_R}\right)}$$

$$\hat{w} = \frac{\left(\sqrt{\rho_L}\,w_L + \sqrt{\rho_R}\,w_R\right)}{\left(\sqrt{\rho_L} + \sqrt{\rho_R}\right)}$$

$$\hat{h} = \frac{\left(\sqrt{\rho_L}\,\dfrac{e_L + p_L}{\rho_L} + \sqrt{\rho_L}\,\dfrac{e_R + p_R}{\rho_R}\right)}{\left(\sqrt{\rho_L} + \sqrt{\rho_R}\right)}$$

$$\hat{c} = \sqrt{(\gamma - 1)\!\left(\hat{h} - \tfrac{1}{2}\!\left(\hat{u}^2 + \hat{v}^2 + \hat{w}^2\right)\right)}$$

Dropping the "^":

$$\Lambda_A = d_A\begin{bmatrix} u' & 0 & 0 & 0 & 0 \\ 0 & u'+c & 0 & 0 & 0 \\ 0 & 0 & u' & 0 & 0 \\ 0 & 0 & 0 & u' & 0 \\ 0 & 0 & 0 & 0 & u'-c \end{bmatrix}; \qquad \Lambda_B = d_B\begin{bmatrix} v' & 0 & 0 & 0 & 0 \\ 0 & v' & 0 & 0 & 0 \\ 0 & 0 & v'+c & 0 & 0 \\ 0 & 0 & 0 & v' & 0 \\ 0 & 0 & 0 & 0 & v'-c \end{bmatrix}$$

$$\Lambda_C = d_C\begin{bmatrix} w' & 0 & 0 & 0 & 0 \\ 0 & w' & 0 & 0 & 0 \\ 0 & 0 & w' & 0 & 0 \\ 0 & 0 & 0 & w'+c & 0 \\ 0 & 0 & 0 & 0 & w'-c \end{bmatrix}$$

$$\Lambda_+ = \frac{\Lambda + |\Lambda|}{2}; \qquad\qquad \Lambda_- = \frac{\Lambda - |\Lambda|}{2}$$

$$d_A = \left.\sqrt{\xi_x^2 + \xi_y^2 + \xi_z^2}\,\right|_{i+\frac{1}{2}}; \qquad d_B = \left.\sqrt{\eta_x^2 + \eta_y^2 + \eta_z^2}\,\right|_{j+\frac{1}{2}}; \qquad d_C = \left.\sqrt{\zeta_x^2 + \zeta_y^2 + \zeta_z^2}\,\right|_{k+\frac{1}{2}}$$

$$u' = \left(\xi_x u + \xi_y v + \xi_z w\right)\big/d_A; \qquad v' = \left(\eta_x u + \eta_y v + \eta_z w\right)\big/d_B; \qquad w' = \left(\zeta_x u + \zeta_y v + \zeta_z w\right)\big/d_C$$

Equation B-6

The metrics are used, at $i + \frac{1}{2}$ as listed in section 2.3.4 and the primitive metrics are

$$x_\eta = \left(x_{i+1,j+1,k+1} - x_{i+1,j,k+1} + x_{i+1,j+1,k} - x_{i+1,j,k}\right)\big/2$$

$$x_\zeta = \left(x_{i+1,j,k+1} - x_{i+1,j,k} + x_{i+1,j+1,k+1} - x_{i+1,j+1,k}\right)\big/2$$

$$y_\eta = \left(y_{i+1,j+1,k+1} - y_{i+1,j,k+1} + y_{i+1,j+1,k} - y_{i+1,j,k}\right)\big/2$$

$$y_\zeta = \left(y_{i+1,j,k+1} - y_{i+1,j,k} + y_{i+1,j+1,k+1} - y_{i+1,j+1,k}\right)\big/2$$

$$z_\eta = \left(z_{i+1,j+1,k+1} - z_{i+1,j,k+1} + z_{i+1,j+1,k} - z_{i+1,j,k}\right)\big/2$$

$$z_\zeta = \left(z_{i+1,j,k+1} - z_{i+1,j,k} + z_{i+1,j+1,k+1} - z_{i+1,j+1,k}\right)\big/2$$

Equation B-7

The metrics are used, at $j + \frac{1}{2}$ as listed in section 2.3.4 and the primitive metrics are:

$$x_\xi = \left(x_{i+1,j+1,k+1} - x_{i,j+1,k+1} + x_{i+1,j+1,k} - x_{i,j+1,k}\right)\big/2$$

$$x_\zeta = \left(x_{i,j+1,k+1} - x_{i,j+1,k} + x_{i+1,j+1,k+1} - x_{i+1,j+1,k}\right)\big/2$$

$$y_\xi = \left(y_{i+1,j+1,k+1} - y_{i,j+1,k+1} + y_{i+1,j+1,k} - y_{i,j+1,k}\right)\big/2$$

$$y_\zeta = \left(y_{i,j+1,k+1} - y_{i,j+1,k} + y_{i+1,j+1,k+1} - y_{i+1,j+1,k}\right)\big/2$$

$$z_\xi = \left(z_{i+1,j+1,k+1} - z_{i,j+1,k+1} + z_{i+1,j+1,k} - z_{i,j+1,k}\right)\big/2$$

$$z_\zeta = \left(z_{i,j+1,k+1} - z_{i,j+1,k} + z_{i+1,j+1,k+1} - z_{i+1,j+1,k}\right)\big/2$$

Equation B-8

The metrics are used, at $k + \frac{1}{2}$ as listed in section 2.3.4 and the primitive metrics are:

$$x_\xi = \left(x_{i+1,j+1,k+1} - x_{i,j+1,k+1} + x_{i+1,j,k+1} - x_{i,j,k+1}\right)\big/2$$

$$x_\eta = \left(x_{i+1,j+1,k+1} - x_{i+1,j,k+1} + x_{i,j+1,k+1} - x_{i,j,k+1}\right)\big/2$$

$$y_\xi = \left(y_{i+1,j+1,k+1} - y_{i,j+1,k+1} + y_{i+1,j,k+1} - y_{i,j,k+1}\right)\big/2$$

$$y_\eta = \left(y_{i+1,j+1,k+1} - y_{i+1,j,k+1} + y_{i,j+1,k+1} - y_{i,j,k+1}\right)\big/2$$

$$z_\xi = \left(z_{i+1,j+1,k+1} - z_{i,j+1,k+1} + z_{i+1,j,k+1} - z_{i,j,k+1}\right)\big/2$$

$$z_\eta = \left(z_{i+1,j+1,k+1} - z_{i+1,j,k+1} + z_{i,j+1,k+1} - z_{i,j,k+1}\right)\big/2$$

Equation B-9

Each cell volume can be made up of six tetrahedrons which are determined as follows:

Cell Volume $= Vol_1 + Vol_2 + Vol_3 + Vol_4 + Vol_5 + Vol_6$

where:

$$
Vol_1 = \left\{
\begin{array}{l}
x_{i,j,k+1}\left[y_{i,j,k}\left(z_{i+1,j,k}-z_{i,j+1,k}\right)-z_{i,j,k}\left(y_{i+1,j,k}-y_{i,j+1,k}\right)+\left(y_{i+1,j,k}z_{i,j+1,k}-z_{i+1,j,k}y_{i,j+1,k}\right)\right] \\[4pt]
-y_{i,j,k+1}\left[x_{i,j,k}\left(z_{i+1,j,k}-z_{i,j+1,k}\right)-z_{i,j,k}\left(x_{i+1,j,k}-x_{i,j+1,k}\right)+\left(x_{i+1,j,k}z_{i,j+1,k}-x_{i,j+1,k}z_{i+1,j,k}\right)\right] \\[4pt]
+z_{i,j,k+1}\left[x_{i,j,k}\left(y_{i+1,j,k}-y_{i,j+1,k}\right)-y_{i,j,k}\left(x_{i+1,j,k}-x_{i,j+1,k}\right)+\left(x_{i+1,j,k}y_{i,j+1,k}-y_{i+1,j,k}z_{i,j+1,k}\right)\right] \\[4pt]
-\left[
\begin{array}{l}
x_{i,j,k}\left(y_{i+1,j,k}z_{i,j+1,k}-z_{i+1,j,k}y_{i,j+1,k}\right)-y_{i,j,k}\left(x_{i+1,j,k}z_{i,j+1,k}-z_{i+1,j,k}x_{i,j+1,k}\right) \\[2pt]
+z_{i,j,k}\left(x_{i+1,j,k}y_{i,j+1,k}-y_{i+1,j,k}x_{i,j+1,k}\right)
\end{array}
\right]
\end{array}
\right\}
$$

$$
Vol_2 = \left\{
\begin{array}{l}
x_{i,j,k+1}\left[y_{i+1,j,k}\left(z_{i+1,j+1,k}-z_{i,j+1,k}\right)-z_{i+1,j,k}\left(y_{i+1,j+1,k}-y_{i,j+1,k}\right)+\left(y_{i+1,j+1,k}z_{i,j+1,k}-z_{i+1,j+1,k}y_{i,j+1,k}\right)\right] \\[4pt]
-y_{i,j,k+1}\left[x_{i+1,j,k}\left(z_{i+1,j+1,k}-z_{i,j+1,k}\right)-z_{i+1,j,k}\left(x_{i+1,j+1,k}-x_{i,j+1,k}\right)+\left(x_{i+1,j+1,k}z_{i,j+1,k}-x_{i,j+1,k}z_{i+1,j+1,k}\right)\right] \\[4pt]
+z_{i,j,k+1}\left[x_{i+1,j,k}\left(y_{i+1,j+1,k}-y_{i,j+1,k}\right)-y_{i+1,j,k}\left(x_{i+1,j+1,k}-x_{i,j+1,k}\right)+\left(x_{i+1,j+1,k}y_{i,j+1,k}-y_{i+1,j+1,k}z_{i,j+1,k}\right)\right] \\[4pt]
-\left[
\begin{array}{l}
x_{i+1,j,k}\left(y_{i+1,j+1,k}z_{i,j+1,k}-z_{i+1,j+1,k}y_{i,j+1,k}\right)-y_{i+1,j,k}\left(x_{i+1,j+1,k}z_{i,j+1,k}-z_{i+1,j+1,k}x_{i,j+1,k}\right) \\[2pt]
+z_{i+1,j,k}\left(x_{i+1,j+1,k}y_{i,j+1,k}-y_{i+1,j+1,k}x_{i,j+1,k}\right)
\end{array}
\right]
\end{array}
\right\}
$$

$$
Vol_3 = \left\{
\begin{array}{l}
x_{i,j,k+1}\left[
\begin{array}{l}
y_{i+1,j,k}\left(z_{i+1,j,k+1}-z_{i+1,j+1,k+1}\right)-z_{i+1,j,k}\left(y_{i+1,j,k+1}-y_{i+1,j+1,k+1}\right) \\[2pt]
+\left(y_{i+1,j,k+1}z_{i+1,j+1,k+1}-z_{i+1,j,k+1}y_{i+1,j+1,k+1}\right)
\end{array}
\right] \\[6pt]
-y_{i,j,k+1}\left[
\begin{array}{l}
x_{i+1,j,k}\left(z_{i+1,j,k+1}-z_{i+1,j+1,k+1}\right)-z_{i+1,j,k}\left(x_{i+1,j,k+1}-x_{i+1,j+1,k+1}\right) \\[2pt]
+\left(x_{i+1,j,k+1}z_{i+1,j+1,k+1}-x_{i+1,j+1,k+1}z_{i+1,j,k+1}\right)
\end{array}
\right] \\[6pt]
+z_{i,j,k+1}\left[
\begin{array}{l}
x_{i+1,j,k}\left(y_{i+1,j,k+1}-y_{i+1,j+1,k+1}\right)-y_{i+1,j,k}\left(x_{i+1,j,k+1}-x_{i+1,j+1,k+1}\right) \\[2pt]
+\left(x_{i+1,j,k+1}y_{i+1,j+1,k+1}-y_{i+1,j,k+1}z_{i+1,j+1,k+1}\right)
\end{array}
\right] \\[6pt]
-\left[
\begin{array}{l}
x_{i+1,j,k}\left(y_{i+1,j,k+1}z_{i+1,j+1,k+1}-z_{i+1,j,k+1}y_{i+1,j+1,k+1}\right)-y_{i+1,j,k}\left(x_{i+1,j,k+1}z_{i+1,j+1,k+1}-z_{i+1,j,k+1}x_{i+1,j+1,k+1}\right) \\[2pt]
+z_{i+1,j,k}\left(x_{i+1,j,k+1}y_{i+1,j+1,k+1}-y_{i+1,j,k+1}x_{i+1,j+1,k+1}\right)
\end{array}
\right]
\end{array}
\right\}
$$

$$
Vol_4 = \left\{
\begin{array}{l}
x_{i,j,k+1}\left[
\begin{array}{l}
y_{i+1,j,k}\left(z_{i+1,j+1,k+1}-z_{i+1,j+1,k}\right)-z_{i+1,j,k}\left(y_{i+1,j+1,k+1}-y_{i+1,j+1,k}\right) \\[2pt]
+\left(y_{i+1,j+1,k+1}z_{i+1,j+1,k}-z_{i+1,j+1,k+1}y_{i+1,j+1,k}\right)
\end{array}
\right] \\[6pt]
-y_{i,j,k+1}\left[
\begin{array}{l}
x_{i+1,j,k}\left(z_{i+1,j+1,k+1}-z_{i+1,j+1,k}\right)-z_{i+1,j,k}\left(x_{i+1,j+1,k+1}-x_{i+1,j+1,k}\right) \\[2pt]
+\left(x_{i+1,j+1,k+1}z_{i+1,j+1,k}-x_{i+1,j+1,k}z_{i+1,j+1,k+1}\right)
\end{array}
\right] \\[6pt]
+z_{i,j,k+1}\left[
\begin{array}{l}
x_{i+1,j,k}\left(y_{i+1,j+1,k+1}-y_{i+1,j+1,k}\right)-y_{i+1,j,k}\left(x_{i+1,j+1,k+1}-x_{i+1,j+1,k}\right) \\[2pt]
+\left(x_{i+1,j+1,k+1}y_{i+1,j+1,k}-y_{i+1,j+1,k+1}z_{i+1,j+1,k}\right)
\end{array}
\right] \\[6pt]
-\left[
\begin{array}{l}
x_{i+1,j,k}\left(y_{i+1,j+1,k+1}z_{i+1,j+1,k}-z_{i+1,j+1,k+1}y_{i+1,j+1,k}\right)-y_{i+1,j,k}\left(x_{i+1,j+1,k+1}z_{i+1,j+1,k}-z_{i+1,j+1,k+1}x_{i+1,j+1,k}\right) \\[2pt]
+z_{i+1,j,k}\left(x_{i+1,j+1,k+1}y_{i+1,j+1,k}-y_{i+1,j+1,k+1}x_{i+1,j+1,k}\right)
\end{array}
\right]
\end{array}
\right\}
$$

$$Vol_5 = \begin{Bmatrix} x_{i,j,k+1}\left[\begin{array}{l} y_{i,j+1,k}\left(z_{i+1,j+1,k+1} - z_{i,j+1,k+1}\right) - z_{i,j+1,k}\left(y_{i+1,j+1,k+1} - y_{i,j+1,k+1}\right) \\ + \left(y_{i+1,j+1,k+1}z_{i,j+1,k+1} - z_{i+1,j+1,k+1}y_{i,j+1,k+1}\right) \end{array}\right] \\ - y_{i,j,k+1}\left[\begin{array}{l} x_{i,j+1,k}\left(z_{i+1,j+1,k+1} - z_{i,j+1,k+1}\right) - z_{i,j+1,k}\left(x_{i+1,j+1,k+1} - x_{i,j+1,k+1}\right) \\ + \left(x_{i+1,j+1,k+1}z_{i,j+1,k+1} - x_{i,j+1,k+1}z_{i+1,j+1,k+1}\right) \end{array}\right] \\ + z_{i,j,k+1}\left[\begin{array}{l} x_{i,j+1,k}\left(y_{i+1,j+1,k+1} - y_{i,j+1,k+1}\right) - y_{i,j+1,k}\left(x_{i+1,j+1,k+1} - x_{i,j+1,k+1}\right) \\ + \left(x_{i+1,j+1,k+1}y_{i,j+1,k+1} - y_{i+1,j+1,k+1}z_{i,j+1,k+1}\right) \end{array}\right] \\ - \left[\begin{array}{l} x_{i,j+1,k}\left(y_{i+1,j+1,k+1}z_{i,j+1,k+1} - z_{i+1,j+1,k+1}y_{i,j+1,k+1}\right) - y_{i,j+1,k}\left(x_{i+1,j+1,k+1}z_{i,j+1,k+1} - z_{i+1,j+1,k+1}x_{i,j+1,k+1}\right) \\ + z_{i,j+1,k}\left(x_{i+1,j+1,k+1}y_{i,j+1,k+1} - y_{i+1,j+1,k+1}x_{i,j+1,k+1}\right) \end{array}\right] \end{Bmatrix}$$

$$Vol_6 = \begin{Bmatrix} x_{i,j,k+1}\left[\begin{array}{l} y_{i,j+1,k}\left(z_{i,j+1,k+1} - z_{i+1,j+1,k+1}\right) - z_{i,j+1,k}\left(y_{i,j+1,k+1} - y_{i+1,j+1,k+1}\right) \\ + \left(y_{i,j+1,k+1}z_{i+1,j+1,k+1} - z_{i,j+1,k+1}y_{i+1,j+1,k+1}\right) \end{array}\right] \\ - y_{i,j,k+1}\left[\begin{array}{l} x_{i,j+1,k}\left(z_{i,j+1,k+1} - z_{i+1,j+1,k+1}\right) - z_{i,j+1,k}\left(x_{i,j+1,k+1} - x_{i+1,j+1,k+1}\right) \\ + \left(x_{i,j+1,k+1}z_{i+1,j+1,k+1} - x_{i+1,j+1,k+1}z_{i,j+1,k+1}\right) \end{array}\right] \\ + z_{i,j,k+1}\left[\begin{array}{l} x_{i,j+1,k}\left(y_{i,j+1,k+1} - y_{i+1,j+1,k+1}\right) - y_{i,j+1,k}\left(x_{i,j+1,k+1} - x_{i+1,j+1,k+1}\right) \\ + \left(x_{i,j+1,k+1}y_{i+1,j+1,k+1} - y_{i,j+1,k+1}z_{i+1,j+1,k+1}\right) \end{array}\right] \\ - \left[\begin{array}{l} x_{i,j+1,k}\left(y_{i,j+1,k+1}z_{i+1,j+1,k+1} - z_{i,j+1,k+1}y_{i+1,j+1,k+1}\right) - y_{i,j+1,k}\left(x_{i,j+1,k+1}z_{i+1,j+1,k+1} - z_{i,j+1,k+1}x_{i+1,j+1,k+1}\right) \\ + z_{i,j+1,k}\left(x_{i,j+1,k+1}y_{i+1,j+1,k+1} - y_{i,j+1,k+1}x_{i+1,j+1,k+1}\right) \end{array}\right] \end{Bmatrix}$$

Equation B-10

The rotated Eigen-values are defined as:

$$S = \begin{pmatrix} 1 & 0 & 0 & 0 & 0 \\ -u\rho^{-1} & \rho^{-1} & 0 & 0 & 0 \\ -v\rho^{-1} & 0 & \rho^{-1} & 0 & 0 \\ -w\rho^{-1} & 0 & 0 & \rho^{-1} & 0 \\ \alpha\beta & -u\beta & -v\beta & -w\beta & \beta \end{pmatrix} ; \quad S^{-1} = \begin{pmatrix} 1 & 0 & 0 & 0 & 0 \\ u & \rho & 0 & 0 & 0 \\ v & 0 & \rho & 0 & 0 \\ w & 0 & 0 & \rho & 0 \\ \alpha & \rho u & \rho v & \rho w & \beta^{-1} \end{pmatrix} ; \quad \begin{array}{l} \alpha = \tfrac{1}{2}\left(u^2 + v^2 + w^2\right); \\ \beta = \gamma - 1 \end{array}$$

$$C_A = \begin{pmatrix} 1 & 0 & 0 & 0 & -c^{-2} \\ 0 & \rho c & 0 & 0 & 1 \\ 0 & 0 & 1 & 0 & 0 \\ 0 & 0 & 0 & 1 & 0 \\ 0 & -\rho c & 0 & 0 & 1 \end{pmatrix} ; \quad C_A^{-1} = \begin{pmatrix} 1 & c^{-2}/2 & 0 & 0 & c^{-2}/2 \\ 0 & \rho^{-1}c^{-1}/2 & 0 & 0 & -\rho^{-1}c^{-1}/2 \\ 0 & 0 & 1 & 0 & 0 \\ 0 & 0 & 0 & 1 & 0 \\ 0 & 1/2 & 0 & 0 & 1/2 \end{pmatrix}$$

$$C_B = \begin{pmatrix} 1 & 0 & 0 & 0 & -c^{-2} \\ 0 & 1 & 0 & 0 & 0 \\ 0 & 0 & \rho c & 0 & 1 \\ 0 & 0 & 0 & 1 & 0 \\ 0 & 0 & -\rho c & 0 & 1 \end{pmatrix} ; \quad C_B^{-1} = \begin{pmatrix} 1 & 0 & c^{-2}/2 & 0 & c^{-2}/2 \\ 0 & 1 & 0 & 0 & 0 \\ 0 & 0 & \rho^{-1}c^{-1}/2 & 0 & -\rho^{-1}c^{-1}/2 \\ 0 & 0 & 0 & 1 & 0 \\ 0 & 0 & 1/2 & 0 & 1/2 \end{pmatrix}$$

$$C_C = \begin{pmatrix} 1 & 0 & 0 & 0 & -c^{-2} \\ 0 & 1 & 0 & 0 & 0 \\ 0 & 0 & 1 & 0 & 0 \\ 0 & 0 & 0 & \rho c & 1 \\ 0 & 0 & 0 & -\rho c & 1 \end{pmatrix} ; \quad C_C^{-1} = \begin{pmatrix} 1 & 0 & 0 & c^{-2}/2 & c^{-2}/2 \\ 0 & 1 & 0 & 0 & 0 \\ 0 & 0 & 1 & 0 & 0 \\ 0 & 0 & 0 & \rho^{-1}c^{-1}/2 & -\rho^{-1}c^{-1}/2 \\ 0 & 0 & 0 & 1/2 & 1/2 \end{pmatrix}$$

and rotation matrices:

$$R_A = \frac{1}{d_A}\begin{pmatrix} d_A & 0 & 0 & 0 & 0 \\ 0 & \xi_x & \xi_y & \xi_z & 0 \\ 0 & -\xi_y & \xi_x & 0 & 0 \\ 0 & -\xi_z & 0 & \xi_x & 0 \\ 0 & 0 & 0 & 0 & d_A \end{pmatrix} ; \qquad R_B = \frac{1}{d_B}\begin{pmatrix} d_B & 0 & 0 & 0 & 0 \\ 0 & \eta_y & -\eta_x & 0 & 0 \\ 0 & \eta_x & \eta_y & \eta_z & 0 \\ 0 & 0 & -\eta_z & \eta_y & 0 \\ 0 & 0 & 0 & 0 & d_B \end{pmatrix} ;$$

$$R_C = \frac{1}{d_C}\begin{pmatrix} d_C & 0 & 0 & 0 & 0 \\ 0 & \zeta_z & 0 & -\zeta_x & 0 \\ 0 & 0 & \zeta_z & -\zeta_y & 0 \\ 0 & \zeta_x & \zeta_y & \zeta_z & 0 \\ 0 & 0 & 0 & 0 & d_C \end{pmatrix}$$

where

$$R_A^{-1} = R_A^T ; \qquad R_B^{-1} = R_B^T ; \qquad R_C^{-1} = R_C^T ;$$

Equation B-11

Explicit Euler Fluxes in the Driving Term

The explicit Euler Fluxes are calculated as follows:

$$\widetilde{F}_{e_{i+\frac{1}{2}}} = \frac{\widetilde{F}_{e_R} + \widetilde{F}_{e_L}}{2} - \tfrac{1}{2}\left(\hat{A}_+ - \hat{A}_-\right)\left(U_R - U_L\right)$$

$$\widetilde{G}_{e_{j+\frac{1}{2}}} = \frac{\widetilde{G}_{e_T} + \widetilde{G}_{e_B}}{2} - \tfrac{1}{2}\left(\hat{B}_+ - \hat{B}_-\right)\left(U_T - U_B\right)$$

$$\widetilde{H}_{e_{k+\frac{1}{2}}} = \frac{\widetilde{H}_{e_I} + \widetilde{H}_{e_O}}{2} - \tfrac{1}{2}\left(\hat{C}_+ - \hat{C}_-\right)\left(U_I - U_O\right)$$

R = Right, L = Left, T = Top, B = Bottom, I = In and O = Out

Equation B-12

The geometric Averaged Jacobians $\hat{A}$, $\hat{B}$ and $\hat{C}$ are calculated as defined earlier.

Dropping the subscript e, the transformed fluxes at the cell corners, $\widetilde{F}, \widetilde{G}\ and\ \widetilde{H}$ (fluxes on RHS of the equations) are determined as follows:

$$\widetilde{F} = \xi_x F + \xi_y G + \xi_z H$$

$$\widetilde{G} = \eta_x F + \eta_y G + \eta_z H$$

$$\widetilde{H} = \zeta_x F + \zeta_y G + \zeta_z H$$

and

$$U = \begin{pmatrix} \rho \\ \rho u \\ \rho v \\ \rho w \\ E \end{pmatrix} ; \quad F = \begin{pmatrix} \rho u \\ \rho u^2 + p \\ \rho uv \\ \rho uw \\ (E+p)u \end{pmatrix} ; \quad G = \begin{pmatrix} \rho v \\ \rho uv \\ \rho v^2 + p \\ \rho vw \\ (E+p)v \end{pmatrix} ; \quad H = \begin{pmatrix} \rho w \\ \rho uw \\ \rho vw \\ \rho w^2 + p \\ (E+p)w \end{pmatrix} ;$$

Equation B-13

Viscous Fluxes

The viscous fluxes can be written in terms of M-matrices as follows:

$$\tilde{F}_v\Big|_{i+\frac{1}{2}} = \left(M^{11}V_\xi + M^{12}V_\eta + M^{13}V_\zeta\right)\Big|_{i+\frac{1}{2}}$$

$$\tilde{G}_v\Big|_{j+\frac{1}{2}} = \left(M^{21}V_\xi + M^{22}V_\eta + M^{23}V_\zeta\right)\Big|_{j+\frac{1}{2}}$$

$$\tilde{H}_v\Big|_{k+\frac{1}{2}} = \left(M^{31}V_\xi + M^{32}V_\eta + M^{33}V_\zeta\right)\Big|_{k+\frac{1}{2}}$$

where

$$V = \begin{pmatrix} \rho & u & v & w & e \end{pmatrix}^T$$

Equation B-14

All the M-matrices have the same format i.e. zero and non-zero elements remain in the same positions:

$$M^{i,j} = \begin{pmatrix} 0 & 0 & 0 & 0 & 0 \\ 0 & m_{22} & m_{23} & m_{24} & 0 \\ 0 & m_{32} & m_{33} & m_{34} & 0 \\ 0 & m_{42} & m_{43} & m_{44} & 0 \\ 0 & m_{52} & m_{53} & m_{54} & m_{55} \end{pmatrix} ; \quad i,j = 1 \rightarrow 3$$

Equation B-15

The viscous fluxes are only determined for use in the explicit driving term. The conserved variable vector V is discretisized as follows:

at the $i+1/2$ face

$$V_\xi = \begin{pmatrix} \rho_{i+1,j,k} - \rho_{i,j,k} \\ u_{i+1,j,k} - u_{i,j,k} \\ v_{i+1,j,k} - v_{i,j,k} \\ w_{i+1,j,k} - w_{i,j,k} \\ e_{i+1,j,k} - e_{i,j,k} \end{pmatrix}$$

$$V_\eta = \begin{pmatrix} \left[\rho_{i,j+1,k} - \rho_{i,j-1,k} + \rho_{i+1,j+1,k} - \rho_{i+1,j-1,k}\right]\Big/4 \\ \left[u_{i,j+1,k} - u_{i,j-1,k} + u_{i+1,j+1,k} - u_{i+1,j-1,k}\right]\Big/4 \\ \left[v_{i,j+1,k} - v_{i,j-1,k} + v_{i+1,j+1,k} - v_{i+1,j-1,k}\right]\Big/4 \\ \left[w_{i,j+1,k} - w_{i,j-1,k} + w_{i+1,j+1,k} - w_{i+1,j-1,k}\right]\Big/4 \\ \left[e_{i,j+1,k} - e_{i,j-1,k} + e_{i+1,j+1,k} - e_{i+1,j-1,k}\right]\Big/4 \end{pmatrix}$$

at the $j+1/2$ face

$$V_\xi = \begin{pmatrix} \left[\rho_{i+1,j,k} - \rho_{i-1,j,k} + \rho_{i+1,j+1,k} - \rho_{i-1,j+1,k}\right]\Big/4 \\ \left[u_{i+1,j,k} - u_{i-1,j,k} + u_{i+1,j+1,k} - u_{i-1,j+1,k}\right]\Big/4 \\ \left[v_{i+1,j,k} - v_{i-1,j,k} + v_{i+1,j+1,k} - v_{i-1,j+1,k}\right]\Big/4 \\ \left[w_{i+1,j,k} - w_{i-1,j,k} + w_{i+1,j+1,k} - w_{i-1,j+1,k}\right]\Big/4 \\ \left[e_{i+1,j,k} - e_{i-1,j,k} + e_{i+1,j+1,k} - e_{i-1,j+1,k}\right]\Big/4 \end{pmatrix}$$

$$V_\eta = \begin{pmatrix} \rho_{i,j+1,k} - \rho_{i,j,k} \\ u_{i,j+1,k} - u_{i,j,k} \\ v_{i,j+1,k} - v_{i,j,k} \\ w_{i,j+1,k} - w_{i,j,k} \\ e_{i,j+1,k} - e_{i,j,k} \end{pmatrix}$$

at the $k+1/2$ face

$$V_\xi = \begin{pmatrix} \left[\rho_{i+1,j,k} - \rho_{i-1,j,k} + \rho_{i+1,j,k+1} - \rho_{i-1,j,k+1}\right]\Big/4 \\ \left[u_{i+1,j,k} - u_{i-1,j,k} + u_{i+1,j,k+1} - u_{i-1,j,k+1}\right]\Big/4 \\ \left[v_{i+1,j,k} - v_{i-1,j,k} + v_{i+1,j,k+1} - v_{i-1,j,k+1}\right]\Big/4 \\ \left[w_{i+1,j,k} - w_{i-1,j,k} + w_{i+1,j,k+1} - w_{i-1,j,k+1}\right]\Big/4 \\ \left[e_{i+1,j,k} - e_{i-1,j,k} + e_{i+1,j,k+1} - e_{i-1,j,k+1}\right]\Big/4 \end{pmatrix}$$

$$V_\eta = \begin{pmatrix} \left[\rho_{i,j+1,k} - \rho_{i,j-1,k} + \rho_{i,j+1,k+1} - \rho_{i,j-1,k+1}\right]\Big/4 \\ \left[u_{i,j+1,k} - u_{i,j-1,k} + u_{i,j+1,k+1} - u_{i,j-1,k+1}\right]\Big/4 \\ \left[v_{i,j+1,k} - v_{i,j-1,k} + v_{i,j+1,k+1} - v_{i,j-1,k+1}\right]\Big/4 \\ \left[w_{i,j+1,k} - w_{i,j-1,k} + w_{i,j+1,k+1} - w_{i,j-1,k+1}\right]\Big/4 \\ \left[e_{i,j+1,k} - e_{i,j-1,k} + e_{i,j+1,k+1} - e_{i,j-1,k+1}\right]\Big/4 \end{pmatrix}$$

$$V_\zeta = \begin{pmatrix} \left[\begin{array}{l}\rho_{i,j,k+1}-\rho_{i,j,k-1} \\ +\rho_{i+1,j,k+1}-\rho_{i+1,j,k-1}\end{array}\right] \Big/ 4 \\[12pt] \left[\begin{array}{l}u_{i,j,k+1}-u_{i,j,k-1} \\ +u_{i+1,j,k+1}-u_{i+1,j,k-1}\end{array}\right] \Big/ 4 \\[12pt] \left[\begin{array}{l}v_{i,j,k+1}-v_{i,j,k-1} \\ +v_{i+1,j,k+1}-v_{i+1,j,k-1}\end{array}\right] \Big/ 4 \\[12pt] \left[\begin{array}{l}w_{i,j,k+1}-w_{i,j,k-1} \\ +w_{i+1,j,k+1}-w_{i+1,j,k-1}\end{array}\right] \Big/ 4 \\[12pt] \left[\begin{array}{l}e_{i,j,k+1}-e_{i,j,k-1} \\ +e_{i+1,j,k+1}-e_{i+1,j,k-1}\end{array}\right] \Big/ 4 \end{pmatrix}$$

$$V_\zeta = \begin{pmatrix} \left[\begin{array}{l}\rho_{i,j,k+1}-\rho_{i,j,k-1} \\ +\rho_{i,j+1,k+1}-\rho_{i,j+1,k-1}\end{array}\right] \Big/ 4 \\[12pt] \left[\begin{array}{l}u_{i,j,k+1}-u_{i,j,k-1} \\ +u_{i,j+1,k+1}-u_{i,j+1,k-1}\end{array}\right] \Big/ 4 \\[12pt] \left[\begin{array}{l}v_{i,j,k+1}-v_{i,j,k-1} \\ +v_{i,j+1,k+1}-v_{i,j+1,k-1}\end{array}\right] \Big/ 4 \\[12pt] \left[\begin{array}{l}w_{i,j,k+1}-w_{i,j,k-1} \\ +w_{i,j+1,k+1}-w_{i,j+1,k-1}\end{array}\right] \Big/ 4 \\[12pt] \left[\begin{array}{l}e_{i,j,k+1}-e_{i,j,k-1} \\ +e_{i,j+1,k+1}-e_{i,j+1,k-1}\end{array}\right] \Big/ 4 \end{pmatrix}$$

$$V_\zeta = \begin{pmatrix} \rho_{i,j,k+1}-\rho_{i,j,k} \\ u_{i,j,k+1}-u_{i,j,k} \\ v_{i,j,k+1}-v_{i,j,k} \\ w_{i,j,k+1}-w_{i,j,k} \\ e_{i,j,k+1}-e_{i,j,k} \end{pmatrix}$$

Equation B-16

$$M^{1L}\Big|_{i+\frac{1}{2}}; \quad L = 1 \to 3$$

$m_{22}^{11} = (2\mu+\lambda)\xi_x^2 + \mu\xi_y^2 + \mu\xi_z^2$

$m_{23}^{11} = (\mu+\lambda)\xi_x\xi_y$

$m_{24}^{11} = (\mu+\lambda)\xi_x\xi_z$

$m_{32}^{11} = m_{23}^{11}$

$m_{33}^{11} = \mu\xi_x^2 + (2\mu+\lambda)\xi_y^2 + \mu\xi_z^2$

$m_{34}^{11} = (\mu+\lambda)\xi_y\xi_z$

$m_{42}^{11} = m_{24}^{11}$

$m_{43}^{11} = m_{34}^{11}$

$m_{44}^{11} = \mu\xi_x^2 + \mu\xi_y^2 + (2\mu+\lambda)\xi_z^2$

$m_{52}^{11} = \bar{u}m_{22}^{11} + \bar{v}m_{32}^{11} + \bar{w}m_{42}^{11}$

$m_{53}^{11} = \bar{u}m_{23}^{11} + \bar{v}m_{33}^{11} + \bar{w}m_{43}^{11}$

$m_{54}^{11} = \bar{u}m_{24}^{11} + \bar{v}m_{34}^{11} + \bar{w}m_{44}^{11}$

$m_{55}^{11} = \kappa\left(\xi_x^2 + \xi_y^2 + \xi_z^2\right)$

$m_{22}^{13} = (2\mu+\lambda)\xi_x\eta_x + \mu\xi_y\eta_y + \mu\xi_z\eta_z$

$m_{23}^{12} = \lambda\xi_x\eta_y + \mu\xi_y\eta_x$

$m_{24}^{12} = \lambda\xi_x\eta_z + \mu\xi_z\eta_x$

$m_{32}^{12} = \lambda\xi_x\eta_z + \mu\xi_z\eta_x$

$m_{33}^{12} = \mu\xi_x\eta_x + (2\mu+\lambda)\xi_y\eta_y + \mu\xi_z\eta_z$

$m_{34}^{13} = \lambda\xi_y\zeta_z + \mu\xi_z\zeta_y$

$m_{42}^{13} = \lambda\xi_z\zeta_y + \mu\xi_y\zeta_z$

$m_{43}^{13} = \lambda\xi_z\zeta_y + \mu\xi_y\zeta_z$

$m_{44}^{13} = \mu\xi_x\zeta_x + \mu\xi_y\zeta_y + (2\mu+\lambda)\xi_z\zeta_z$

$m_{52}^{11} = \bar{u}m_{22}^{11} + \bar{v}m_{32}^{11} + \bar{w}m_{42}^{11}$

$m_{53}^{11} = \bar{u}m_{23}^{11} + \bar{v}m_{33}^{11} + \bar{w}m_{43}^{11}$

$m_{54}^{11} = \bar{u}m_{24}^{11} + \bar{v}m_{34}^{11} + \bar{w}m_{44}^{11}$

$m_{55}^{11} = \kappa\left(\xi_x^2 + \xi_y^2 + \xi_z^2\right)$

$m_{22}^{12} = (2\mu+\lambda)\xi_x\eta_x + \mu\xi_y\eta_y + \mu\xi_z\eta_z$

$m_{23}^{12} = \lambda\xi_x\eta_y + \mu\xi_y\eta_x$

$m_{24}^{12} = \lambda\xi_x\eta_z + \mu\xi_z\eta_x$

$m_{32}^{12} = \lambda\xi_x\eta_z + \mu\xi_z\eta_x$

$m_{33}^{12} = \mu\xi_x\eta_x + (2\mu+\lambda)\xi_y\eta_y + \mu\xi_z\eta_z$

$m_{34}^{12} = \lambda\xi_y\eta_z + \mu\xi_z\eta_y$

$m_{42}^{12} = \lambda\xi_z\eta_x + \mu\xi_x\eta_z$

$m_{43}^{12} = \lambda\xi_z\eta_y + \mu\xi_y\eta_z$

$m_{44}^{12} = \mu\xi_x\eta_x + \mu\xi_y\eta_y + (2\mu+\lambda)\xi_z\eta_z$

$m_{52}^{12} = \bar{u}m_{22}^{12} + \bar{v}m_{32}^{12} + \bar{w}m_{42}^{12}$

$m_{53}^{12} = \bar{u}m_{23}^{12} + \bar{v}m_{33}^{12} + \bar{w}m_{43}^{12}$

$m_{54}^{12} = \bar{u}m_{24}^{12} + \bar{v}m_{34}^{12} + \bar{w}m_{44}^{12}$

$m_{55}^{12} = \kappa\left(\xi_x\eta_x + \xi_y\eta_y + \xi_z\eta_z\right)$

$\bar{u} = \dfrac{u_{i+1,j,k} + u_{i,j,k}}{2}$

$\bar{v} = \dfrac{v_{i+1,j,k} + v_{i,j,k}}{2}$

$\bar{w} = \dfrac{w_{i+1,j,k} + w_{i,j,k}}{2}$

$\mu = \mu\left(\dfrac{T_{i+1,j,k} + T_{i,j,k}}{2}\right)$

with primitive metrics:

$$x_\xi = \left(\begin{array}{l} x_{i+2,j+1,k} - x_{i,j+1,k} + x_{i+2,j,k} - x_{i,j,k} \\ x_{i+2,j+1,k+1} - x_{i,j+1,k+1} + x_{i+2,j,k+1} - x_{i,j,k+1} \end{array}\right)\Big/8$$

$$x_\eta = \left(x_{i+1,j+1,k+1} - x_{i+1,j,k+1} + x_{i+1,j+1,k} - x_{i+1,j,k}\right)\Big/2$$

$$x_\zeta = \left(x_{i+1,j,k+1} - x_{i+1,j,k} + x_{i+1,j+1,k+1} - x_{i+1,j+1,k}\right)\Big/2$$

$$y_\xi = \left(\begin{array}{l} y_{i+2,j+1,k} - y_{i,j+1,k} + y_{i+2,j,k} - y_{i,j,k} \\ y_{i+2,j+1,k+1} - y_{i,j+1,k+1} + y_{i+2,j,k+1} - y_{i,j,k+1} \end{array}\right)\Big/8$$

$$y_\eta = \left(y_{i+1,j+1,k+1} - y_{i+1,j,k+1} + y_{i+1,j+1,k} - y_{i+1,j,k}\right)\Big/2$$

$$y_\zeta = \left(y_{i+1,j,k+1} - y_{i+1,j,k} + y_{i+1,j+1,k+1} - y_{i+1,j+1,k}\right)\Big/2$$

$$z_\xi = \left(\begin{array}{l} z_{i+2,j+1,k} - z_{i,j+1,k} + z_{i+2,j,k} - z_{i,j,k} \\ z_{i+2,j+1,k+1} - z_{i,j+1,k+1} + z_{i+2,j,k+1} - z_{i,j,k+1} \end{array}\right)\Big/8$$

$$z_\eta = \left(z_{i+1,j+1,k+1} - z_{i+1,j,k+1} + z_{i+1,j+1,k} - z_{i+1,j,k}\right)\Big/2$$

$$z_\zeta = \left(z_{i+1,j,k+1} - z_{i+1,j,k} + z_{i+1,j+1,k+1} - z_{i+1,j+1,k}\right)\Big/2$$

$$M^{2L}\Big|_{j+\frac{1}{2}}; \quad L = 1 \to 3$$

$m^{21}_{22} = (2\mu+\lambda)\xi_x\eta_x + \mu\xi_y\eta_y + \mu\xi_z\eta_z$ 　　　 $m^{22}_{22} = (2\mu+\lambda)\eta_x^2 + \mu\eta_y^2 + \mu\eta_z^2$

$m^{21}_{23} = \lambda\eta_x\xi_y + \mu\eta_y\xi_x$ 　　　 $m^{22}_{23} = (\mu+\lambda)\eta_x\eta_y$

$m^{21}_{24} = \lambda\eta_x\xi_z + \mu\eta_z\xi_x$ 　　　 $m^{22}_{24} = (\mu+\lambda)\eta_x\eta_z$

$m^{21}_{32} = \lambda\eta_y\xi_x + \mu\eta_x\xi_y$ 　　　 $m^{22}_{32} = m^{22}_{23}$

$m^{21}_{33} = \mu\xi_x\eta_x + (2\mu+\lambda)\xi_y\eta_y + \mu\xi_z\eta_z$ 　　　 $m^{22}_{33} = \mu\eta_x^2 + (2\mu+\lambda)\eta_y^2 + \mu\eta_z^2$

$m^{21}_{34} = \lambda\eta_z\xi_y + \mu\eta_y\xi_z$ 　　　 $m^{22}_{34} = (\mu+\lambda)\eta_y\eta_z$

$m^{21}_{42} = \lambda\eta_x\xi_z + \mu\eta_z\xi_x$ 　　　 $m^{22}_{42} = m^{22}_{24}$

$m^{21}_{43} = \lambda\eta_y\xi_z + \mu\eta_z\xi_y$ 　　　 $m^{22}_{43} = m^{22}_{34}$

$m^{21}_{44} = \mu\xi_x\eta_x + \mu\xi_y\eta_y + (2\mu+\lambda)\xi_z\eta_z$ 　　　 $m^{22}_{44} = \mu\eta_x^2 + \mu\eta_y^2 + (2\mu+\lambda)\eta_z^2$

$m^{21}_{52} = \bar{u}m^{21}_{22} + \bar{v}m^{21}_{32} + \bar{w}m^{21}_{42}$ 　　　 $m^{22}_{52} = \bar{u}m^{22}_{22} + \bar{v}m^{22}_{32} + \bar{w}m^{22}_{42}$

$m^{21}_{53} = \bar{u}m^{21}_{23} + \bar{v}m^{21}_{33} + \bar{w}m^{21}_{43}$ 　　　 $m^{22}_{53} = \bar{u}m^{22}_{23} + \bar{v}m^{22}_{33} + \bar{w}m^{22}_{43}$

$m^{21}_{54} = \bar{u}m^{21}_{24} + \bar{v}m^{21}_{34} + \bar{w}m^{21}_{44}$ 　　　 $m^{22}_{54} = \bar{u}m^{22}_{24} + \bar{v}m^{22}_{34} + \bar{w}m^{22}_{44}$

$m^{21}_{55} = \kappa\left(\xi_x\eta_x + \xi_y\eta_y + \xi_z\eta_z\right)$ 　　　 $m^{22}_{55} = \kappa\left(\eta_x^2 + \eta_y^2 + \eta_z^2\right)$

$$m_{22}^{23} = (2\mu + \lambda)\xi_x\zeta_x + \mu\xi_y\zeta_y + \mu\xi_z\zeta_z$$

$$m_{23}^{23} = \lambda\eta_x\zeta_y + \mu\eta_y\zeta_x$$

$$m_{24}^{23} = \lambda\eta_x\zeta_z + \mu\eta_z\zeta_x$$

$$m_{32}^{23} = \lambda\eta_y\zeta_x + \mu\eta_x\zeta_y$$

$$m_{33}^{23} = \mu\xi_x\zeta_x + (2\mu + \lambda)\xi_y\zeta_y + \mu\xi_z\zeta_z$$

$$m_{34}^{23} = \lambda\eta_y\zeta_z + \mu\eta_z\zeta_y$$

$$m_{42}^{23} = \lambda\eta_z\zeta_x + \mu\eta_x\zeta_z$$

$$m_{43}^{23} = \lambda\eta_z\zeta_y + \mu\eta_y\zeta_z$$

$$m_{44}^{23} = \mu\zeta_x\eta_x + \mu\zeta_y\eta_y + (2\mu + \lambda)\zeta_z\eta_z$$

$$m_{52}^{23} = \bar{u}m_{22}^{23} + \bar{v}m_{32}^{23} + \bar{w}m_{42}^{23}$$

$$m_{53}^{23} = \bar{u}m_{23}^{23} + \bar{v}m_{33}^{23} + \bar{w}m_{43}^{23}$$

$$m_{54}^{23} = \bar{u}m_{24}^{23} + \bar{v}m_{34}^{23} + \bar{w}m_{44}^{23}$$

$$m_{55}^{23} = \kappa(\zeta_x\eta_x + \zeta_y\eta_y + \zeta_z\eta_z)$$

$$\bar{u} = \frac{u_{i,j+1,k} + u_{i,j,k}}{2}$$

$$\bar{v} = \frac{v_{i,j+1,k} + v_{i,j,k}}{2}$$

$$\bar{w} = \frac{w_{i,j+1,k} + w_{i,j,k}}{2}$$

$$\mu = \mu\left(\frac{T_{i,j+1,k} + T_{i,j,k}}{2}\right)$$

with primitive metrics:

$$x_\xi = \left(x_{i+1,j+1,k+1} - x_{i,j+1,k+1} + x_{i+1,j+1,k} - x_{i,j+1,k}\right)/2$$

$$x_\eta = \left(\begin{array}{c} x_{i,j+2,k+1} - x_{i,j,k+1} + x_{i,j+2,k} - x_{i,j,k} \\ x_{i+1,j+2,k+1} - x_{i+1,j,k+1} + x_{i+1,j+2,k} - x_{i+1,j,k} \end{array}\right)\Big/8$$

$$x_\zeta = \left(x_{i,j+1,k+1} - x_{i,j+1,k} + x_{i+1,j+1,k+1} - x_{i+1,j+1,k}\right)/2$$

$$y_\xi = \left(y_{i+1,j+1,k+1} - y_{i,j+1,k+1} + y_{i+1,j+1,k} - y_{i,j+1,k}\right)/2$$

$$y_\eta = \left(\begin{array}{c} y_{i,j+2,k+1} - y_{i,j,k+1} + y_{i,j+2,k} - y_{i,j,k} \\ y_{i+1,j+2,k+1} - y_{i+1,j,k+1} + y_{i+1,j+2,k} - y_{i+1,j,k} \end{array}\right)\Big/8$$

$$y_\zeta = \left(y_{i,j+1,k+1} - y_{i,j+1,k} + y_{i+1,j+1,k+1} - y_{i+1,j+1,k}\right)/2$$

$$z_\xi = \left(z_{i+1,j+1,k+1} - z_{i,j+1,k+1} + z_{i+1,j+1,k} - z_{i,j+1,k}\right)/2$$

$$z_\eta = \left(\begin{array}{c} z_{i,j+2,k+1} - z_{i,j,k+1} + z_{i,j+2,k} - z_{i,j,k} \\ z_{i+1,j+2,k+1} - z_{i+1,j,k+1} + z_{i+1,j+2,k} - z_{i+1,j,k} \end{array}\right)\Big/8$$

$$z_\zeta = \left(z_{i,j+1,k+1} - z_{i,j+1,k} + z_{i+1,j+1,k+1} - z_{i+1,j+1,k}\right)/2$$

$$M^{3L}\Big|_{k+\frac{1}{2}}; \quad L = 1 \rightarrow 3$$

$m_{22}^{31} = (2\mu + \lambda)\xi_x\zeta_x + \mu\xi_y\zeta_y + \mu\xi_z\zeta_z$

$m_{23}^{31} = \lambda\zeta_x\xi_y + \mu\zeta_y\xi_x$

$m_{24}^{31} = \lambda\zeta_x\xi_z + \mu\zeta_z\xi_x$

$m_{32}^{31} = \lambda\zeta_y\xi_x + \mu\zeta_x\xi_y$

$m_{33}^{31} = \mu\xi_x\zeta_x + (2\mu + \lambda)\xi_y\zeta_y + \mu\xi_z\zeta_z$

$m_{34}^{31} = \lambda\xi_z\zeta_y + \mu\xi_y\zeta_z$

$m_{42}^{31} = \lambda\zeta_z\xi_x + \mu\zeta_x\xi_z$

$m_{43}^{31} = \lambda\zeta_z\xi_y + \mu\zeta_y\xi_z$

$m_{44}^{31} = \mu\xi_x\zeta_x + \mu\xi_y\zeta_y + (2\mu + \lambda)\xi_z\zeta_z$

$m_{52}^{31} = \bar{u}m_{22}^{31} + \bar{v}m_{32}^{31} + \bar{w}m_{42}^{31}$

$m_{53}^{31} = \bar{u}m_{23}^{31} + \bar{v}m_{33}^{31} + \bar{w}m_{43}^{31}$

$m_{54}^{31} = \bar{u}m_{24}^{31} + \bar{v}m_{34}^{31} + \bar{w}m_{44}^{31}$

$m_{55}^{31} = \kappa\left(\xi_x\zeta_x + \xi_y\zeta_y + \xi_z\zeta_z\right)$

$m_{22}^{33} = (2\mu + \lambda)\zeta_x^2 + \zeta\eta_y^2 + \zeta\eta_z^2$

$m_{23}^{33} = (\mu + \lambda)\zeta_x\zeta_y$

$m_{24}^{33} = (\mu + \lambda)\zeta_x\zeta_z$

$m_{32}^{33} = m_{23}^{33}$

$m_{33}^{33} = \mu\zeta_x^2 + (2\mu + \lambda)\zeta_y^2 + \mu\zeta_z^2$

$m_{34}^{33} = (\mu + \lambda)\zeta_y\zeta_z$

$m_{42}^{33} = m_{24}^{33}$

$m_{43}^{33} = m_{34}^{33}$

$m_{44}^{33} = \mu\zeta_x^2 + \mu\zeta_y^2 + (2\mu + \lambda)\zeta_z^2$

$m_{52}^{33} = \bar{u}m_{22}^{33} + \bar{v}m_{32}^{33} + \bar{w}m_{42}^{33}$

$m_{53}^{33} = \bar{u}m_{23}^{33} + \bar{v}m_{33}^{33} + \bar{w}m_{43}^{33}$

$m_{54}^{33} = \bar{u}m_{24}^{33} + \bar{v}m_{34}^{33} + \bar{w}m_{44}^{33}$

$m_{55}^{33} = \kappa\left(\zeta_x^2 + \zeta_y^2 + \zeta_z^2\right)$

$m_{22}^{32} = (2\mu + \lambda)\eta_x\zeta_x + \mu\eta_y\zeta_y + \mu\eta_z\zeta_z$

$m_{23}^{32} = \lambda\zeta_x\eta_y + \mu\zeta_y\eta_x$

$m_{24}^{32} = \lambda\zeta_x\eta_z + \mu\zeta_z\eta_x$

$m_{32}^{32} = \lambda\zeta_z\eta_y + \mu\zeta_y\eta_z$

$m_{33}^{32} = \mu\eta_x\zeta_x + (2\mu + \lambda)\eta_y\zeta_y + \mu\eta_z\zeta_z$

$m_{34}^{32} = \lambda\eta_y\zeta_z + \mu\eta_z\zeta_y$

$m_{42}^{32} = \lambda\zeta_z\eta_x + \mu\zeta_x\eta_z$

$m_{43}^{32} = \lambda\zeta_z\eta_y + \mu\zeta_y\eta_z$

$m_{44}^{23} = \mu\zeta_x\eta_x + \mu\zeta_y\eta_y + (2\mu + \lambda)\zeta_z\eta_z$

$m_{52}^{32} = \bar{u}m_{22}^{32} + \bar{v}m_{32}^{32} + \bar{w}m_{42}^{32}$

$m_{53}^{32} = \bar{u}m_{23}^{32} + \bar{v}m_{33}^{32} + \bar{w}m_{43}^{32}$

$m_{54}^{32} = \bar{u}m_{24}^{32} + \bar{v}m_{34}^{32} + \bar{w}m_{44}^{32}$

$m_{55}^{32} = \kappa\left(\zeta_x\eta_x + \zeta_y\eta_y + \zeta_z\eta_z\right)$

$\bar{u} = \dfrac{u_{i,j,k+1} + u_{i,j,k}}{2}$

$\bar{v} = \dfrac{v_{i,j,k+1} + v_{i,j,k}}{2}$

$\bar{w} = \dfrac{w_{i,j,k+1} + w_{i,j,k}}{2}$

$\mu = \mu\left(\dfrac{T_{i,j,k+1} + T_{i,j,k}}{2}\right)$

with primitive metrics:

$$x_\xi = \left(x_{i+1,j+1,k+1} - x_{i,j+1,k+1} + x_{i+1,j,k+1} - x_{i,j,k+1} \right) \big/ 2$$

$$x_\eta = \left(x_{i+1,j+1,k+1} - x_{i+1,j,k+1} + x_{i,j+1,k+1} - x_{i,j,k+1} \right) \big/ 2$$

$$x_\zeta = \left(\begin{array}{c} x_{i,j+1,k+2} - x_{i,j+1,k} + x_{i,j,k+2} - x_{i,j,k} \\ x_{i+1,j+1,k+2} - x_{i+1,j+1,k} + x_{i+1,j,k+2} - x_{i+1,j,k} \end{array} \right) \big/ 8$$

$$y_\xi = \left(y_{i+1,j+1,k+1} - y_{i,j+1,k+1} + y_{i+1,j,k+1} - y_{i,j,k+1} \right) \big/ 2$$

$$y_\eta = \left(y_{i+1,j+1,k+1} - y_{i+1,j,k+1} + y_{i,j+1,k+1} - y_{i,j,k+1} \right) \big/ 2$$

$$y_\zeta = \left(\begin{array}{c} y_{i,j+1,k+2} - y_{i,j+1,k} + y_{i,j,k+2} - y_{i,j,k} \\ y_{i+1,j+1,k+2} - y_{i+1,j+1,k} + y_{i+1,j,k+2} - y_{i+1,j,k} \end{array} \right) \big/ 8$$

$$z_\xi = \left(z_{i+1,j+1,k+1} - z_{i,j+1,k+1} + z_{i+1,j,k+1} - z_{i,j,k+1} \right) \big/ 2$$

$$z_\eta = \left(z_{i+1,j+1,k+1} - z_{i+1,j,k+1} + z_{i,j+1,k+1} - z_{i,j,k+1} \right) \big/ 2$$

$$z_\zeta = \left(\begin{array}{c} z_{i,j+1,k+2} - z_{i,j+1,k} + z_{i,j,k+2} - z_{i,j,k} \\ z_{i+1,j+1,k+2} - z_{i+1,j+1,k} + z_{i+1,j,k+2} - z_{i+1,j,k} \end{array} \right) \big/ 8$$

and

$$\kappa = \frac{\gamma\mu}{\mathrm{Pr}}; \quad \lambda = -\frac{2}{3}\mu; \quad e = c_v T$$

$$N = \begin{pmatrix} 1 & 0 & 0 & 0 & 0 \\ -u\rho^{-1} & \rho^{-1} & 0 & 0 & 0 \\ -v\rho^{-1} & 0 & \rho^{-1} & 0 & 0 \\ -w\rho^{-1} & 0 & 0 & \rho^{-1} & 0 \\ (\alpha-e)\rho^{-1} & -u\rho^{-1} & -v\rho^{-1} & -w\rho^{-1} & \rho^{-1} \end{pmatrix}; \qquad \alpha = \frac{u^2 + v^2 + w^2}{2}$$

Equation B-17

Implementation
The algorithm is implemented in two sweeps:

sweep1: backward direction keeping k constant (decreasing i direction)
sweep2: forward direction keeping k constant (increasing i direction)

The process is now repeated incrementing k from 2 to NZ-1

Finally, the solution is updated and the time step is incremented.

Boundary Conditions

This method is an 3D extension of the Thin layer 2D Reynolds-averaged Navier-Stokes boundary conditions as described by Craig[28].

Impermeable Boundaries

The explicit and implicit boundary conditions are treated separately.

Explicit Euler boundary conditions:

$$U_m = R_o^{-1}TR_oU_n;$$

$$T = \begin{pmatrix} 1 & 0 & 0 & 0 & 0 \\ 0 & 1 & 0 & 0 & 0 \\ 0 & 0 & p & 0 & 0 \\ 0 & 0 & 0 & q & 0 \\ 0 & 0 & 0 & 0 & 1 \end{pmatrix} \quad for \quad \begin{cases} J - \text{surface: } p = -1; q = 1; o = B \\ K - \text{surface: } p = 1; q = -1; o = A \\ \text{lower boudary: } m = 1; n = 2 \\ \text{upper boundary: } m = NJ; n = NJ - 1 \text{ on } J - \text{surface} \\ \qquad\qquad m = NK; n = NK - 1 \text{ on } K - \text{surface} \end{cases}$$

Equation B-18

$$\rho_m = U_m(1)$$
$$u_m = U_m(2)/U_m(1)$$
$$v_m = U_m(3)/U_m(1)$$
$$w_m = U_m(4)/U_m(1)$$
$$E_m = U_m(5)$$
$$e_m = U_m(5)/U_m(1) - (u_m^2 + v_m^2 + w_m^2)/2$$
$$p_m = (\gamma - 1)e_m\rho_m$$
$$c_m = \sqrt{\frac{\gamma p_m}{\rho_m}}$$

Explicit viscous boundary conditions:

$$\rho_m = \rho_n$$
$$u_m = -u_n + 2u_{wall}$$
$$v_m = -v_n$$
$$w_m = -w_n$$
$$e_m = (1 - t_1)T_{wall}c_v + t_1e_n$$
$$t_1 = \begin{cases} 1 & adiabatic\ wall \\ -1 & isothermal\ wall \end{cases}$$

Implicit viscous boundary conditions:

no slip boundary at $j=1\frac{1}{2}$

$$\hat{A}'_2 = \hat{A}_2 - \frac{\Delta t}{V_{i,2,k}} \widetilde{B}_{+,i,1\frac{1}{2},k} R_B^{-1}TR_B$$

$$- \frac{\Delta t}{V_{i,2,k}} \left(\begin{array}{l} M_{i,1\frac{1}{2},k}^{22}E_lN_{i,2,k} - \frac{1}{4}M_{i+\frac{1}{2},j,k}^{12}E_lN_{i,2,k} + \frac{1}{4}M_{i-\frac{1}{2},j,k}^{12}E_lN_{i,2,k} + \frac{1}{4}M_{i,j,k+\frac{1}{2}}^{32}E_lN_{i,2,k} \\ -\frac{1}{4}M_{i,j,k-\frac{1}{2}}^{32}E_lN_{i,2,k} \end{array} \right)$$

Equation B-19

no slip boundary at $j=NJ-\frac{1}{2}$

$$\hat{A}'_{NJ-1} = \hat{A}_{NJ-1} + \frac{\Delta t}{V_{i,NJ-1,k}}\widetilde{B}_{-_{i,NJ-\frac{1}{2},k}}R_B^{-1}TR_B$$

$$-\frac{\Delta t}{V_{i,NJ-1,k}}\left(\begin{array}{l} M^{22}_{i,NJ-\frac{1}{2},k}E_lN_{i,NJ-1,k} + \frac{1}{4}M^{12}_{i+\frac{1}{2},NJ-\frac{1}{2},k}E_lN_{i,NJ-1,k} - \frac{1}{4}M^{12}_{i-\frac{1}{2},NJ-\frac{1}{2},k}E_lN_{i,NJ-1,k} \\ +\frac{1}{4}M^{32}_{i,NJ-\frac{1}{2},k+\frac{1}{2}}E_lN_{i,NJ-1,k} + \frac{1}{4}M^{32}_{i,NJ-\frac{1}{2},k-\frac{1}{2}}E_lN_{i,NJ-1,k} \end{array}\right)$$

Equation B-20

no slip boundary at $k=1\frac{1}{2}$

$$\widetilde{A}'_2 = \widetilde{A}_2 - \frac{\Delta t}{V_{i,j,2}}\hat{C}_{+_{i,j,1\frac{1}{2}}}R_A^{-1}TR_A$$

$$-\frac{\Delta t}{V_{i,j,2}}\left(\begin{array}{l} M^{33}_{i,j,1\frac{1}{2}}E_lN_{i,j,2} - \frac{1}{4}M^{13}_{i,j,1\frac{1}{2}}E_lN_{i,j,2} + \frac{1}{4}M^{13}_{i-\frac{1}{2},j,k}E_lN_{i,j,2} - \frac{1}{4}M^{23}_{i,j+\frac{1}{2},k}E_lN_{i,j,2} \\ +\frac{1}{4}M^{23}_{i,j-\frac{1}{2},k}E_lN_{i,j,2} - \frac{1}{4}M^{23}_{i,j+\frac{1}{2},k}E_lN_{i,j,2} + \frac{1}{4}M^{23}_{i,j-\frac{1}{2},k}E_lN_{i,j,2} - \frac{1}{4}M^{32}_{i,j,1\frac{1}{2}}E_lN_{i,j,2} \\ +\frac{1}{4}M^{32}_{i,j,1\frac{1}{2}}E_lN_{i,j,2} \end{array}\right)$$

Equation B-21

no slip boundary at $k=NK-\frac{1}{2}$

$$\hat{A}'_{NK-1} = \widetilde{A}_{NK-1}\frac{\Delta t}{V_{i,j,NK-1}}\hat{C}_{-_{i,j,NJ-\frac{1}{2}}}R_A^{-1}TR_A$$

$$-\frac{\Delta t}{V_{i,j,NK-1}}\left(\begin{array}{l} M^{33}_{i,j,NK-\frac{1}{2}}E_lN_{i,j,NK-1} + \frac{1}{4}M^{13}_{i,j,NK-\frac{1}{2}}E_lN_{i,j,NK-1} - \frac{1}{4}M^{13}_{i-\frac{1}{2},j,k-\frac{1}{2}}E_lN_{i,j,NK-1} \\ -\frac{1}{4}M^{23}_{i,j-\frac{1}{2},k-\frac{1}{2}}E_lN_{i,j,NK-1} + \frac{1}{4}M^{23}_{i,j+\frac{1}{2},NK-\frac{1}{2}}E_lN_{i,j,NK-1} + \frac{1}{4}M^{23}_{i,j+\frac{1}{2},NK-\frac{1}{2}}E_lN_{i,j,NK-1} \\ -\frac{1}{4}M^{23}_{i,j-\frac{1}{2},k-\frac{1}{2}}E_lN_{i,j,NK-1} + \frac{1}{4}M^{32}_{i,j,NK-\frac{1}{2}}E_lN_{i,j+1,NK-1} - \frac{1}{4}M^{32}_{i,j,NK-\frac{1}{2}}E_lN_{i,j-1,NK-1} \end{array}\right)$$

Equation B-22

Entrance Boundaries
For 3D flow four independent external quantities have to be specified for subsonic entrance conditions. The following quantities were chosen:

$$p_t \quad = \text{Total ambient pressure [kPa]}$$
$$T_t \quad = \text{Ambient temperature [K]}$$
$$\theta_v, \theta_w = \text{Entrance velocity angles}$$

The entrance pressure and temperature can be expressed as a function of the flow velocity:

$$p = p_t\left[1 - \frac{\gamma-1}{\gamma+1}\left(1 + \tan^2\theta_v + \tan^2\theta_w\right)\frac{u^2}{a_*^2}\right]^{\frac{\gamma}{\gamma-1}} = p(u)$$

$$T = T_t\left[1 - \frac{\gamma-1}{\gamma+1}\left(1 + \tan^2\theta_v + \tan^2\theta_w\right)\frac{u^2}{a_*^2}\right] = T(u)$$

$$v = u\tan\theta_v = v(u);\; w = u\tan\theta_w = w(u);\; a_*^2 = 2\gamma\frac{\gamma-1}{\gamma+1}c_vT_t$$

Equation B-23

The flow variables are updated as follows:

$$u_1^{n+1} = u_1^n + \delta u_1$$

$$v_1^{n+1} = u_1^{n+1} \tan \theta_v$$

$$w_1^{n+1} = u_1^{n+1} \tan \theta_w$$

$$p_1^{n+1} = p\left(u_1^{n+1}\right)$$

$$T_1^{n+1} = T\left(u_1^{n+1}\right)$$

$$\rho_1^{n+1} = \frac{p_1^{n+1}}{(\gamma - 1)c_v T_1^{n+1}}$$

$$\alpha = \frac{\left(u_1^{n+1}\right)^2 + \left(v_1^{n+1}\right)^2 + \left(w_1^{n+1}\right)^2}{2}$$

$$E_1^{n+1} = \rho_1^{n+1}\left(c_v T_1^{n+1} + \alpha\right)$$

δu_1 is solved as follows:

$$\delta u_1 = \frac{R}{\left(\dfrac{\delta p}{\delta u}\right)_1 - \rho_1 c_1}$$

where

$$R = -\lambda_4 \left(p_2 - p_1 - \rho_1 c_1 (u_2 - u_1)\right)$$

$$\lambda_4 = \frac{\lambda}{1 - \lambda}$$

$$\lambda = \frac{(u_1 - c_1)\Delta t}{\Delta x}$$

$$\left(\frac{\delta p}{\delta u}\right)_1 = -\frac{p_t \left(1 + \tan^2 \theta_v + \tan^2 \theta_w\right)u}{(\gamma - 1)c_v T_t}\left[1 - \frac{\gamma - 1}{\gamma + 1}\left(1 + \tan^2 \theta_v + \tan^2 \theta_w\right)\frac{u^2}{a_*^2}\right]^{\frac{1}{\gamma - 1}}$$

Equation B-24

<u>Exit Boundaries</u>

For subsonic exit boundary conditions only one external variable needs to be specified. For super-sonic flows no external conditions need to be specified.

The flow variables are updated as follows:

$$\rho_{NI}^{n+1} = \rho_{NI}^{n} + \delta\rho_{NI}$$

$$u_{NI}^{n+1} = u_{NI}^{n} + \delta u_{NI}$$

$$v_{NI}^{n+1} = v_{NI}^{n} + \delta v_{NI}$$

$$w_{NI}^{n+1} = w_{NI}^{n} + \delta w_{NI}$$

$$p_{NI}^{n+1} = p_{NI}^{n} + \delta p_{NI}$$

$$T_{NI}^{n+1} = \frac{p_{NI}^{n+1}}{(\gamma-1)c_v\rho_{NI}^{n+1}}$$

$$\alpha = \frac{\left(u_{NI}^{n+1}\right)^2 + \left(v_{NI}^{n+1}\right)^2 + \left(w_{NI}^{n+1}\right)^2}{2}$$

$$E_{NI}^{n+1} = \rho_{NI}^{n+1}\left(c_v T_{NI}^{n+1} + \alpha\right)$$

Equation B-25

The changes in the flow variables are defined as:

$$\delta p_{NI} = \begin{cases} \dfrac{R_2 + R_5}{2} & \text{if } M_{NI-1} = \dfrac{u_{NI-1}}{c_{NI-1}} \geq 1 \\ \Delta t \dfrac{\delta p_e}{\delta t} = 0 & \text{if } M_{NI-1} = \dfrac{u_{NI-1}}{c_{NI-1}} < 1 \end{cases}$$

$$\delta\rho_{NI} = R_1 + \frac{\delta p_{NI}}{c_{NI-1}^2}$$

$$\delta p_{NI} = \frac{\left(R_2 - \delta p_{NI}\right)}{\rho_{NI-1}c_{NI-1}}$$

$$\delta v_{NI} = R_3$$

$$\delta w_{NI} = R_4$$

Equation B-26

where

$$R_1 = -\lambda_1\left(\rho_{NI} - \rho_{NI-1} - \frac{1}{c_{NI-1}^2}\left(p_{NI} - p_{NI-1}\right)\right)$$

$$R_2 = -\lambda_2\left(p_{NI} - p_{NI-1} + \rho_{NI-1}c_{NI-1}\left(u_{NI} - u_{NI-1}\right)\right)$$

$$R_3 = -\lambda_1\left(v_{NI} - v_{NI-1}\right)$$

$$R_4 = -\lambda_1\left(w_{NI} - w_{NI-1}\right)$$

$$R_5 = -\lambda_4\left(p_{NI} - p_{NI-1} - \rho_{NI-1}c_{NI-1}\left(u_{NI} - u_{NI-1}\right)\right)$$

$$\lambda_i = \frac{\lambda'_i}{1+\lambda'_i}; i = 1,2,4$$

$$\lambda'_1 = \frac{u_{NI-1}\Delta t}{\Delta x}; \quad \lambda'_2 = \frac{\left(u_{NI-1} + c_{NI-1}\right)\Delta t}{\Delta x}; \quad \lambda'_4 = \frac{\left(u_{NI-1} - c_{NI-1}\right)\Delta t}{\Delta x}$$